HETEROGENEOUSLY CATALYSED CHEMOSELECTIVE REDUCTION OF UNSATURATED NITRO AND CARBONYL COMPOUNDS

Eva PLESSERS

Supervisors:
Prof. M. Roeffaers, KU Leuven
Prof. D. De Vos, KU Leuven

Members of the Examination Committee:
Prof. J. Buyse, KU Leuven, Chair
Prof. J. Hofkens, KU Leuven
Prof. J. Martens, KU Leuven
Prof. R. Ameloot, KU Leuven
Prof. K. de Jong, Utrecht University

Dissertation presented
in partial fulfilment of
the requirements for the
degree of Doctor of
Bioscience Engineering

2016

Doctoraatsproefschrift nr. 1374 aan de faculteit Bio-ingenieurswetenschappen van de KU Leuven

Uitgegeven in eigen beheer, Eva Plessers, Bilzen

PREFACE

Bij het schrijven van dit voorwoord denk ik spontaan terug aan 4 jaar geleden, toen ik voor dezelfde opdracht stond bij het afronden van mijn masterthesis. Ik had toen een interessant jaar achter de rug en keek vol verwachting uit naar de start van een volgende fase in mijn leven. Dat enthousiasme was terecht, want ook vandaag kan ik tevreden en met enige trots terugblikken op de afgelopen 4 jaar en popel ik om aan een nieuw hoofdstuk te beginnen. Dat goede gevoel heb ik echter niet enkel aan mezelf te danken, maar vooral aan iedereen die er bij en voor mij waren.

Het is een ongeschreven regel, maar naar mijn mening ook een volledig terechte regel om je promotoren eerst te bedanken. Maarten, bedankt voor alles, en dat is veel. In de eerste plaats voor het vertrouwen, het vertrouwen in mij door geregeld te zeggen 'ge kunt dat', maar ook het vertrouwen langs mijn kant dat ik altijd met alles bij u terecht kon. Bedankt om zo betrokken en enthousiast te zijn over mijn onderzoek en me vooruit te helpen, maar ook om regelmatig terloops de bureau binnen te wandelen, een mopje te maken en te vragen hoe het ging. Want ook voor mijn persoonlijke ontwikkeling had je aandacht en kon ik altijd mezelf zijn. Bedankt om me aan te moedigen mijn creatieve vaardigheden te ontwikkelen, mijn eerste well-figuur was rampzalig lelijk, maar uiteindelijk kreeg ik van onze Nederlandse collega toch een 'mooi plaatje' als commentaar op mijn figuur. Bedankt Dirk, om zo gepassioneerd met wetenschap bezig te zijn dat dat aanstekelijk werkt voor iedereen in de buurt. Bedankt om me de kans te geven een interessant FWO-project aan te vragen en altijd bereid te zijn om experimenten te bediscussiëren en vragen te beantwoorden. Ook bedankt aan mijn assessoren, professoren Johan Hofkens en Johan Martens, voor de interesse en nuttige suggesties. Bedankt prof. Krijn de Jong en prof. Rob Ameloot voor jullie bereid om in mijn jury te zetelen. En bedankt aan mijn voorzitter, prof. Johan Buyse, voor de flexibiliteit om prof. René De Mot te vervangen zodat de verdediging tijdig kon plaatsvinden en omdat ik anders nog niet genoeg Johannen in mijn jury had zitten.

Maar natuurlijk kan je niet alleen vooruit zonder fantastische collega's. Voor mijn eerste stappen in de wereld van de doctoraatsstudenten werd ik gedropt in de beruchte bureau 69. Ondanks dat ik de eerste vrouw was in deze bureau, was er naast flauwe (ja, nog steeds vrouw-onvriendelijke) moppen ook nog plaats voor normale gesprekken en goede raad. Bedankt Frederik, Bart, Laurens, Ivo, Jeroen en Maxime. En ook bedankt aan de overige katalyse-collega's en in het bijzonder de katalyse-jaargenoten, voor de babbels in het labo, tijdens de middag en COK-weekends. Ik had het geluk niet van één, maar van twee geweldige labo's deel uit te maken. Het LPS was in het begin nog één grote, onbekende leefgemeenschap met zijn eigen gebruiken en tradities (plezante weekendjes en activiteiten), uitspattingen (cocktail-feestjes onder leiding van het opperhoofd), sfeerbrengers (Doortje) en moederfiguur om deze bende op het rechte pad te houden (Carine). Bedankt ook Katrien om me in het begin in te leiden in deze groep, ook al zat je de eerste weken nog in Valencia. Tijdens die 4 jaar kwamen er ook vele toffe collega's in Maarten zijn groep bij, bedankt allen en in het bijzonder Alexey, Jordi, Christian, Wouter, Collin, Tom, Bartosz (en Dennis, soms-dan-toch) om samen een bureau te delen. Bedankt LPS-ladies voor de toffe dates, slappe-lach-momenten, luisterende oren en al het lekkere eten & drinken; girlpower! Al dat labowerk zou verder niet gelukt zijn

zonder de ondersteuning van het GC-Team (bedankt vooral Laurens & Bart), de technische hulp van Johan, Stef, Paul en Tony; en Carine, Sabina & Annelies om te zorgen dat niemand iets tekort kwam en alles vlot geregeld werd.

Bedankt liefste vrienden van de Thunderbuddies, één van de mooiste souvenirs uit mijn studententijd is jullie vriendschap. Ook al besloten we verschillende promotoren en zelfs faculteiten op te zoeken, we blijven één groep die ontstond uit het melkhuisje en haar 2 kippen. De lunchen 's middags, de supergezellige etentjes, de vakantie/weekendjes, … Stilletjes aan komt er een einde aan onze studententijd, Leuven wordt steeds minder en minder een fysieke schakel tussen ons allen; maar dat maakt onze etentjes in Mechelen, Hasselt, Aarschot, Bilzen, toekomstige-stek-J&E-in-de-Vlaanders(?) en wie-weet-waar-T&E-zullen-belanden des te interessanter. Natuurlijk niet te vergeten, de Gang. Ook al hebben jullie niet rechtstreeks een invloed gehad op de wetenschappelijke uitkomst van mijn doctoraat, de verwondering over de titel en jullie aanwezigheid op mijn publieke verdediging doen me een groot plezier. 15 jaar geleden waren jullie nog gewoon toffe meiden waar ik toevallig mee in de klas zat, vandaag zijn jullie vriendinnen voor het leven. Bedankt voor alle steun, verjaardagen (les Lacs du Connemara in het bijzonder), girlsweekends, festivals, cafébezoekjes, babbels, plezier maken en jullie liefde.

Ik prijs mij ook gelukkig met de warme familie waarin ik opgroeide en nog steeds kan thuiskomen. Mama en papa, bedankt voor de liefde en vele mogelijkheden die we kregen om fantastische momenten te beleven, maar ook de vrijheid die we kregen om ons ding te doen, soms eens fouten te laten maken en zo onszelf te vormen tot de kinderen die we nu zijn. Nu we allemaal volwassen zijn kan ik zeggen dat jullie daarin goed gelukt zijn, want ik heb een pracht van een broer en een zus. Mamoe, Moeke en Opa die voor ons zorgen zoals alleen grootouders dat kunnen. Papoe, jammer dat je hier nu niet trots kan zitten wezen, maar voor ons ben je er altijd bij. Familie Housen, na 7 jaar voel ik me toch een klein beetje lid van de familie. Mimi en Ben, bedankt voor het de gastvrijheid en de warmte, en vooral voor het voortbrengen van een pracht van een zoon, natuurlijk. Elke, Bart, Nele, Sara en Carlo om me zo op te nemen in de familie. Merci liefje, ook al interesseerde mijn onderzoek je niet zoveel en was je soms minder enthousiast dan ik hoopte over de foto's of figuren die ik je liet zien, ik had dit niet tot eenzelfde einde kunnen brengen zonder jou. Als het even niet wilde lukken of als ik juist erg goed nieuws had, kon ik dat gevoel het beste delen met jou. Voor de veranderingen in mijn persoonlijke leven de afgelopen 4 jaar ben jij verantwoordelijk en daar ben ik alleen maar heel blij en dankbaar voor. Sorry dat gedurende de laatste maanden mijn focus vooral op het doctoraat lag en je vele uren alleen voor de verbouwing doorbracht. Ik kijk er zo hard naar uit om samen verder te werken aan ons droomhuisje in het schone Kleine-Spouwen en samen als berggeiten oud te worden.

Proost, op de afgelopen 4 jaar, waarin de wondere wereld van de wetenschap weer een stukje van zijn geheimen heeft prijs gegeven, maar tegelijkertijd nog meer mysteries heeft gecreëerd; proost op 4 fantastische jaren waarin ik ook veel over mezelf geleerd heb en sterker ben geworden als persoon; proost op 4 zalige jaren met schatten van mensen ... En nu op naar een nieuw avontuur!

Eva

Allylic alcohols and functionalized anilines are industrially valuable flavouring and fragrance compounds and important intermediates for pharmaceuticals, polymers and other fine chemicals. These compounds can be synthesised via chemoselective reduction of unsaturated aldehydes and nitro compounds. Reduction of the olefinic group yields saturated aldehydes and nitro compounds, whereas hydrogenation of the carbonyl and nitro group produce allylic alcohols and unsaturated amines. Typically, this reduction is performed under high hydrogen pressure conditions with supported metal catalysts, alternatively transfer hydrogenation with an alcohol as hydride donor and a Lewis acid catalyst can be employed. The former process is most widely applicable, but is not straightforward since olefins are often preferentially reduced, due to thermodynamic and kinetic reasons. To direct selectivity towards the desired products there is thus a strong motivation to develop chemoselective supported metal reduction catalysts. Platinum group metals (Pt, Pd, Ir, Rh, Os and Ru; PGMs) are typically used, but often require complex doping schemes. Silver on the contrary, has a very high intrinsic chemoselectivity towards unsaturated products in reductions of polyfunctional molecules and will thus be explored in this work as chemoselective reduction catalyst.

Metal nanoparticle catalysts used for the chemoselective reduction are typically supported on porous materials like silica, alumina and carbon. These supports stabilise the metal nanoparticles preventing their aggregation and hence loss in activity and/or selectivity. Though more interestingly the pores of these support can also be used to control the size of nanoparticles via pore confined synthesis strategies. In this work, chemoselective hydrogenation with a commonly used silver on silica catalyst is investigated first, whereafter the development of a new chemoselective silver catalyst on an innovative material is described and the remarkable transfer hydrogenation catalysing power of this support.

In the first experimental chapter (**Chapter 2**), the chemoselective reduction of 4-nitrostyrene using a silver on silica catalyst, prepared via the standard incipient wetness (IWI) procedure, is explored in detail. In IWI a porous support is filled with a metal precursor solution that equals the pore volume of the support. After drying and calcination, the final supported metal nanoparticle catalyst is obtained. In contrast to the typically used bulk averaging or spatially resolving characterisation techniques, in this work optical microscopy is used as the most important characterisation technique. Optical microscopy proved to be a convenient tool to directly interlink structural and compositional information and hydrogenation performance of individual support particles. This novel correlative imaging approach revealed for the first time how incipient wetness impregnation led to 10-fold

variations in silver loading between individual submillimetre-sized silica support granules. Furthermore, this heterogeneity had a profound impact on the catalytic performance: 100-fold interparticle variations in normalized catalytic performance were discovered for the chemoselective 4-nitrostyrene reduction between granules of the same batch. This detailed study revealed the optimal silver loading and based on this information the normalized yield was increased by 38 %.

To unravel the origin of this interparticle heterogeneity the impregnation process was dissected into the individual synthesis steps (impregnation, drying & calcination) and the pre-impregnated support, and investigated in detail using optical microscopy (**Chapter 3**). Examination of the influence of each elementary step on the resulting silver distribution pointed out that every step introduces a minimal degree of interparticle heterogeneity, but the optimised drying procedure has the largest impact on the heterogeneity. More specifically, the position of a support granule in the stagnant drying bed has a large influence on the resulting colour and thus silver distribution. Moving from a static to a fluidized bed drying resulted in an improved homogeneity in silver loading on the different support granules. This optimised drying procedure is easy to implement in the lab and on even larger scales.

The importance of generating well-defined and stable silver nanoparticles was an incentive to look into pore confinement in metal organic frameworks (MOFs). These results are described in **Chapter 4**. Silver nanoparticles were successfully synthesized by pore confinement in UiO-66, a widely used zirconium-based metal-organic framework. A recyclable 10 wt% Ag/UiO-66 catalyst reached complete conversion of cinnamaldehyde after 6 h and 50 bar of H_2 with 66 % selectivity for cinnamyl alcohol in the inert solvent *N,N*-dimethylacetamide (140°C, 25 mg catalyst, 2 mol% Ag). Surprisingly, pure UiO-66 without silver reached complete conversion with > 90 % selectivity after 24 h at 120°C (25 mg catalyst, 8 mol% Zr) in isopropyl alcohol solvent, even in absence of H_2. The Lewis acid sites of the Zr-support catalyse transfer hydrogenation of cinnamaldehyde with isopropyl alcohol, a procedure called Meerwein-Ponndorf-Verley (MPV) reduction. The substrate scope of this MPV reduction was successfully extended to citral and carvone, two α,β-unsaturated carbonyl compounds that are harder to reduce selectively. Further catalyst optimisation was possible via the introduction of a NO_2-functional group into the UiO-66 linker, increasing the Lewis acidity.

Based on the high activity and chemoselectivity in the reduction of unsaturated carbonyl compounds using the Lewis acid Zr-sites in UiO-66, a large pore Zr-based MOF, MOF-808-P, was explored as MPV reduction catalyst with isopropyl alcohol as solvent and hydride donor**.** These large pores of MOF-808-P facilitate the formation of the six-membered ring transition state and more importantly, the Zr-atom in the MOF-cluster is undercoordinated which should lead to an increased number and

strength of the Lewis acid sites compared to UiO-66. MOF-808-P catalysed MPV reduction obtained already 99 % cinnamyl alcohol yield after only 2 h (120 °C, 20 mg catalyst, 8 mol% Zr) **(Chapter 5)**. The highly active MOF-808-P was furthermore a good catalyst for the selective reduction of more challenging substrates such as carvone and β-ionone. The activity for the former was 20-fold increased with respect to UiO-66. Two strategies were successfully used to shift the equilibrium reaction towards the desired allylic alcohol products: 1) evaporation of formed acetone when using isopropyl alcohol and 2) the use of the more strongly reducing 1-indanol. Via these approaches the carveol yield was increased to > 70 %.

SAMENVATTING

Onverzadigde alcoholen en gefunctionaliseerde anilines zijn industrieel waardevolle smaak- en geurstoffen en belangrijke tussenproducten voor farmaceutica, polymeren en andere fijnchemicaliën. Deze onverzadigde componenten worden typisch gesynthetiseerd via chemoselectieve reductie van onverzadigde aldehyden en nitroverbindingen. Reductie van de onverzadigde koolstof-koolstofbinding leidt tot de vorming van verzadigde aldehyden en nitroverbindingen, terwijl hydrogenatie van de carbonyl- en nitrogroep onverzadigde alcoholen en amines voortbrengt. Deze chemoselectieve reductie kan zowel uitgevoerd worden onder hoge waterstofdruk met gedragen metaalnanopartikelkatalysatoren, als via transferhydrogenatie met een Lewiszure katalysator en een alcohol als hydridedonor. Chemoselectieve hydrogenatie onder hoge druk is meer algemeen toepasbaar dan transferhydrogenatie, maar bereikt typisch een lagere selectiviteit, omwille van thermodynamische en kinetische redenen wordt de onverzadigde binding eerder gehydrogeneerd dan de functionele carbonyl- of nitrogroep. Via het gebruik van chemoselectieve hydrogenatiekatalysatoren kan daarentegen de selectiviteit naar de gewenste producten verhoogd worden. Platinumgroepmetalen (Pt, Pd, Ir, Rh, Os en Ru; PGM's) worden meestal gebruikt als katalysator, maar deze metalen vereisen vaak ingewikkelde doperingsschema's om de gewenste chemoselectiviteit te bekomen. Zilver daarentegen heeft een erg hoge intrinsieke chemoselectiviteit voor onverzadigde producten in meervoudig gefunctionaliseerde verbindingen, dus zal dit werk zich focussen op zilver als chemoselectieve reductiekatalysator.

De metaalnanopartikels worden typisch afgezet op een poreuze drager zoals silica, alumina en koolstof. Deze dragers zorgen voor stabilisatie van de metaalnanopartikels en voorkomen zo aggregatie en verlies van activiteit en selectiviteit. Nog interessanter is het gericht gebruik van de poriën van de drager om de grootte van de nanopartikels te controleren via 'pore confinement' of vrij vertaald 'porierestrictie'. In dit werk zal chemoselectieve hydrogenatie met een vaak gebruikte zilver-op-silicakatalysator eerst onderzocht worden, waarna de ontwikkeling van de nieuwe chemoselectieve zilverkatalysator op een innovatieve drager beschreven is, naast de opmerkelijke transferhydrogenatie katalyserende eigenschappen van deze drager.

In het eerste experimentele deel (**Hoofdstuk 2**) wordt de chemoselectieve reductie van 4-nitrostyreen door een zilver-op-silicakatalysator in detail onderzocht. Deze katalysator werd gesynthetiseerd via standaard 'incipient wetness impregnation' (IWI). In IWI wordt een poreuze drager gevuld met een metaalprecursoroplossing die van volume exact overeenkomt met het porievolume van de drager. Na drogen en calcinatie wordt dan de uiteindelijke gedragen metaalnanopartikelkatalysator

verkregen. Op laboratoriumschaal wordt deze katalysator typisch gekarakteriseerd met technieken die ofwel een gemiddelde waarde opleveren voor het volledige katalysatorstaal, ofwel met hoge resolutie kijken naar een erg beperkt deel van het totale staal. In dit werk werd optische microscopie gebruikt als meest belangrijke karakterisatietechniek. Optische microscopie bleek een uiterst geschikte techniek om structurele en compositionele informatie te linken aan de katalytische activiteit en selectiviteit van individuele gedragen katalysatorpartikels. Deze nieuwe correlatieve methode bracht voor het eerst onder de aandacht hoe traditionele 'incipient wetness impregnation' leidt tot tienvoudige verschillen in zilverbelading tussen individuele silicadragerpartikels met een diameter kleiner dan een millimeter. Daarenboven had deze interpartikelheterogeniteit een grote impact op de katalytische activiteit en selectiviteit: tussen individuele dragerpartikels van hetzelfde originele staal werden 100-voudige verschillen in genormaliseerde activiteit in de hydrogenatie van 4-nitrostyreen gemeten. Deze gedetailleerde studie bracht de optimale zilverbelading aan het licht en gebaseerd op deze informatie werd de genormaliseerde opbrengst verhoogd met 38 %.

De oorzaak van deze interpartikelheterogeniteit werd opgespoord door het impregnatieproces onder te verdelen in de verschillende individuele synthesestappen (de impregnatie, de droogstap en de calcinatie) en de drager voor impregnatie en deze verschillende aspecten in detail te bestuderen via optische microscopie (**Hoofdstuk 3**). Analyse van de invloed van elk van deze elementaire stappen op de finale zilververdeling wees uit dat elke stap minstens een minimale graad van heterogeniteit veroorzaakt, maar dat optimalisatie van de droogstap de grootste invloed had op de heterogeniteit. In het bijzonder is de positie van een dragerpartikel in het statische droogbed van groot belang voor de uiteindelijke kleur en dus zilverbelading. Verandering van een statisch droogbed naar drogen in een wervelbed leidde tot een sterk verbeterde zilverbelading op het niveau van de dragerpartikels. Deze optimalisatie is makkelijk toe te passen in het labo en zelfs op grotere schaal.

Het belang van goed gedefinieerde en stabiele zilvernanopartikels was een sterke motivatie om de vorming van deze nanopartikels via porierestrictie met behulp van een metaal-organisch rooster (MOF) te onderzoeken. Deze resultaten staan beschreven in **Hoofdstuk 4**. Zilvernanopartikels werden succesvol gevormd via porierestrictie in UiO-66, een vaak gebruikt zirkonium-gebaseerd metaal-organisch rooster. Een recycleerbare 10 wt% Ag/UiO-66-katalysator bereikte volledige cinnamaldehyde-conversie na 6 uur en bij een druk van 50 bar H_2 met 66 % selectiviteit voor cinnamylalcohol in het inerte solvent *N,N*-dimethylaceetamide (140 °C, 25 mg katalysator, 2 mol% Ag). Merkwaardig genoeg bereikte onbeladen UiO-66 zonder zilver volledige conversie met meer dan 90 % selectiviteit binnen 24

uur bij 120 °C (25 mg katalysator, 8 mol% Zr) in isopropylalcohol-solvent, zelfs in afwezigheid van H_2. De Lewiszure sites van het zirkoniumrooster katalyseren de transferhydrogenatie van cinnamaldehyde met isopropylalcohol, de zogenaamde Meerwein-Ponndorf-Verleyreductie (MPV). Het substraatbereik van de MPV-reductie werd verder met succes uitgebreid tot citral en carvone, twee α,β-onverzadigde carbonylverbindingen die typisch moeilijker selectief te reduceren zijn. Verdere katalysatoroptimalisatie was mogelijk via de incorporatie van NO_2-gefunctionaliseerde linkermoleculen in het UiO-66 rooster die de Lewiszuurheid verhogen.

Verder bouwend op de hoge activiteit en chemoselectiviteit in de reductie van onverzadigde carbonylverbindingen door de Lewiszure Zr-sites in UiO-66, werd een Zr-gebaseerde MOF met grote poriën, MOF-808-P, getest als MPV-reductiekatalysator met isopropylalcohol als solvent en hydridedonor. De grote poriën van MOF-808-P vergemakkelijken de vorming van de transitietoestand die bestaat uit een zesvormige ring. Nog belangrijker echter is het feit dat het Zr-atoom in de MOF-cluster ondergecoördineerd is, dit leidt tot een verhoogd aantal en verhoogde sterkte van de Lewiszure sites in vergelijking met UiO-66. MOF-808-P-gekatalyseerde MPV-reductie bereikte 99 % opbrengst van cinnamylalcohol na amper 2 uur (120 °C, 20 mg katalysator, 8 mol% Zr) (**Hoofdstuk 5**). De erg actieve MOF-808-P was daarenboven ook een goede katalysator voor de selectieve reductie van meer uitdagende substraten zoals carvone en β-ionone. De activiteit voor carvone kon 20 keer verhoogd worden ten opzichte van UiO-66. Twee strategieën werden met succes gebruikt om het evenwicht van de reactie in de richting van de gewenste onverzadigde alcoholen te sturen: 1) verdamping van gevormd aceton wanneer isopropylalcohol gebruikt werd als reductans en 2) het gebruik van een sterker reductans: 1-indanol. Via deze strategieën werd de carveol-opbrengst verhoogd tot meer dan 70 %.

4-NSt	4-nitrostyrene
4-VAn	4-vinylaniline
BDC	1,4-benzenedicarboxylate
BTC	1,3,5-benzenetricarboxylate
CALD	cinnamaldehyde
CALH	cinnamyl alcohol
CUS	coordinatively unsaturated site
DMA	*N,N*-dimethylacetamide
DMF	*N,N*-dimethylformamide
DRS	diffuse reflectance spectroscopy
DSC	differential scanning calorimetry
EDX	energy-dispersive X-ray spectroscopy
EXAFS	extended X-ray absorption fine structure
FIB	focused ion beam
FID	flame ionisation detector
FTIR	Fourier transform infrared
GC	gas chromatography
ICP-AES	inductively coupled plasma-atomic emission spectroscopy
IPA	isopropyl alcohol
IWI	incipient wetness impregnation
MCM	Mobil crystalline material
MOF	metal-organic framework
MS	mass spectrometry
MPV(O)	Meerwein-Ponndorf-Verley-Oppenauer
PGM	Platinum group metal
SBA	Santa Barbara amorphous type material
SBU	secondary building unit
SERS	surface enhanced Raman scattering
SEM	scanning electron microscopy
SPR	surface plasmon resonance
TEM	transmission electron microscopy
TEOS	tetraethyl orthosilicate
TGA	thermogravimetric analysis
UiO	University of Oslo
UV/Vis	ultra violet/visible
XAFS	X-ray absorption fine structure spectroscopy
XRD	X-ray diffraction

TABLE OF CONTENTS

CHAPTER 1

INTRODUCTION

Abstract

This literature overview presents a general introduction to the synthesis of unsaturated functionalized compounds via chemoselective reduction. Starting with the synthesis and characterization of supported metal nanoparticles, the catalysts typically used for this reaction. Continued with a summary of the heterogeneity encountered in heterogeneous catalyst batches and proceeded with an overview on chemoselective catalytic reduction. To conclude the scope of this research is formulated.

CHAPTER 1 - INTRODUCTION

Chemoselective reduction of unsaturated nitro- and carbonyl compounds is a valuable route in the fine chemical industry to obtain unsaturated amines and alcohols. Allylic alcohols are important fragrance and flavour components and give compositions their characteristic notes.[1–3] Geraniol is an unsaturated alcohol with a flowery-roselike odor and is one of the most frequently used terpenoid fragrance materials. Cinnamyl alcohol, the most important unsaturated aromatic alcohol, is used as the base for a variety of perfumes and in flavoring for cinnamon and fruit aromas.[4] Furthermore, cinnamyl alcohol is an important intermediate in the pharmaceutical industry, e. g. the cardiovascular drug cinnarizine is derived from cinnamyl alcohol.[5] Although these allylic alcohols naturally occur in several oils, they are mostly synthesized at large-scale via catalytic hydrogenation.[4] Geraniol can be produced via the chemoselective hydrogenation of the α,β-unsaturated aldehyde citral. This is an economically attractive route since citral is an intermediate in the vitamine A synthesis and produced petrochemically. This chemoselective hydrogenation step, as patented by BASF,[6] can be catalysed by Pt nanoparticles supported on a ZnO support. Cinnamyl alcohol can be prepared by reduction of cinnamaldehyde via three different routes: 1) chemoselective hydrogenation of the carbonyl group by supported noble metal catalysts (originally patented for an Os/C catalyst in 1972);[7] 2) Meerwein-Ponndorf-Verley reduction with isopropyl alcohol and 3) reduction with alkali borohydrides.[4]

Chemoselective catalytic hydrogenation is widespread in chemical industry and is typically performed over supported noble metal catalysts such as the Pt/ZnO catalyst used for the geraniol and cinnamyl alcohol production. This catalytic hydrogenation of unsaturated aldehydes and ketones can yield saturated carbonyl compounds when the olefinic group is reduced, whereas hydrogenation of the carbonyl group produces allylic alcohols. Carbonyl hydrogenation is generally less facile than olefin hydrogenation, making selective hydrogenation of α,β-unsaturated aldehydes and ketones to the allyl alcohol challenging. Several metals have been reported as being selective for the production of cinnamyl alcohol from cinnamaldehyde. The Os/C catalyst mentioned above is highly selective, but not ideal for implementation at the industrial scale because of handling difficulties and bulk availability and cost of osmium salts. Supported platinum group metal (PGM) catalysts on the other hand are important hydrogenation catalysts which normally allow reaction at mild temperature and under low pressures. Comparison of PGMs on graphite and activated carbon led to the following selectivity trend: Ir > Pt > Ru > Rh > Pd.[2] More

recently the selectivity trend for C=O over C=C hydrogenation in α,β-unsaturated aldehydes such as citral and crotonaldehyde has been updated and completed with other non-PGMs: Co > Ag > Au > Pd > Pt > Ru.[5] Nickel catalysts are also used, but their toxicity and the elevated reaction temperature and pressure needed hamper their use in batch synthesis typically performed in the fine chemical and pharmaceutical industries.[2]

As mentioned in the example of cinnamyl alchohol, allylic alcohols can also be obtained via the Meerwein-Ponndorf-Verley (MPV) reduction of unsaturated aldehydes. MPV reduction is a hydrogen transfer reaction which can be performed under mild conditions and without the risk of reducing other functional groups like C=C bonds. Typically easily oxidizable alcohols, e.g. isopropyl alcohol, are used as hydrogen donor, in combination with solids with surface basicity or Lewis acidity as catalyst, e.g. alumina, zirconia or magnesium oxide. Grafted zeolites are interesting MPV catalysts since high yields are reported at low loadings;[8] more interestingly their shape selectivity can also be used to induce stereoselectivity.[2] This is an important aspect in pharmaceutical and fragrance industry since in certain products stereochemically pure compounds are required.

Besides allylic alcohols, unsaturated amine compounds are also used as intermediates in the synthesis of pharmaceuticals, polymers and other fine chemicals. Primary aromatic amines are generally produced by the liquid phase catalytic hydrogenation of aromatic nitro compounds. Heterogeneous hydrogenation of these compounds is an interesting route for the production of the corresponding anilines, since theoretically no by-products except water are formed. The hydrogenation mechanism leading to these amines is complex and a variety of nitroso and hydroxylamine intermediates and products are formed.[2,9] The majority of the research reported on chemoselective hydrogenation of nitro-groups focusses on the reduction of halogenated nitro-compounds without hydrolysing the aromatic C-halogen bound. To decrease side product formation and direct selectivity towards the desired product, a correct metal catalyst choice is required. The most frequently used hydrogenation catalysts for the liquid phase hydrogenation of nitro groups are Raney nickel and noble metals such as Pt and Pd supported on large area supports like silica, alumina and carbon.[10]

Since both unsaturated alcohols and aromatic amines are obtained via chemoselective hydrogenation with supported metal nanoparticle catalysts, these catalysts will be discussed first (chapter 1.1), followed by an introduction on selective catalysis (chapter 1.2) via the chemoselective hydrogenation and the Meerwein-Ponndorf-Verley reduction.

1.1 SUPPORTED METAL CATALYSTS

1.1.1 **Synthesis**

Supported metal research catalysts are synthesized through a variety of different methods, subdivided into physical (sonication, microwaves, UV, pulsed laser ablation, supercritical fluids), chemical (impregnation, co-precipitation, deposition-precipitation, microemulsions, chemical vapour deposition, electrochemical reduction) and physicochemical categories (sonoelectro-chemical, flame spray pyrolysis) in the review by White *et al.* (2009).[11] Recent developments in the synthesis of supported metal catalysts is given in the review by de Jong *et al.*, highlighting also emerging techniques such as atomic layer deposition.[12] Ion-exchange of the precursor with surface groups on the support[13] and sol-gel techniques[14] are two other chemical synthesis techniques that are commonly used. The method of choice depends predominantly on the level of control that is aimed for on the final loading and distribution as well as on the used support and metal precursor.

Supported industrial catalysts are mainly synthesized via impregnation, although vapour deposition is employed routinely as well.[15] Since impregnation is also one of the most used classical synthesis techniques at lab scale,[11,16] the following discussion will be limited to this preparation method. The synthesis of supported metal nanoparticles via impregnation can largely be divided into two types: impregnation with interaction between support and precursor and without interaction.[13] Impregnation with interaction is defined as the process in which a bond is formed between the metal precursor to be deposited and the surface of the support. The most commonly occurring form of impregnation with interaction is based on ion-exchange and depends on the nature of the precursor and support; this exchange can be categorized as acid-base, acid-salt, base-salt or salt-salt exchange.[13] Because of the highly localized exchange sites on the surface, impregnation via ion exchange typically leads to better metal dispersion than impregnation without exchange. Metal-loaded zeolites for example are typically prepared via ion-exchange of a metal cation with a H^+ or Na^+ counter ion. Pure oxide surfaces on the contrary do not bare permanent charges, their surface hydroxyl groups are amphoteric and can be positively, neutral and negatively charged depending on the pH of the impregnation solution. A synthesis technique in which pH typically plays a key role, is deposition-precipitation: via slowly altering the impregnation solution conditions (typically a pH increase), a chemical reaction is induced that decreases the metal complex solubility, followed by a controlled precipitation.[12] Homogeneous precipitation can be induced by addition of urea ($CO(NH_2)_2$) at room temperature, followed by heating to 90 °C and slow hydrolysis of urea into CO_2, NH_4^+ and OH^-. This formation of OH^- ions results

in a pH increase and is used for the precursor deposition, however an excess of urea is necessary since part of the urea is hydrolysed into NH_3 and CO_2.[17] Impregnation of oxides with interaction can also occur upon adsorption of the metal precursor from the impregnation solution onto the support without adding any additional agent, the maximally achievable loading however is typically low in this case and achieving a uniform deposition might take several days. Higher loadings can be achieved via impregnation of a precursor that does not absorb onto the support surface or only displays a weak interaction.

Impregnation offers the advantage that it can be used with a variety of precursors and supports and that it can be performed in 'dry' or 'wet' conditions, depending on the relative amounts of support and precursor solution volume used. In dry impregnation a porous support is filled with a metal precursor solution that equals the pore volume of the support. Upon impregnation the powder reaches a slurry state, therefore also called pore volume or incipient wetness impregnation (IWI).[12,15] IWI is a widespread technique because of the simple steps with minimal waste and all the used metal ends up in the final catalyst.[11,17] However, to prevent bursting of the catalyst as the result of capillary forces or temperature rise resulting from the exothermic heat of water adsorption, the support can be wetted prior to impregnation. Wet impregnation, the process in which a water filled support is immersed in the precursor solution, may also be used when thermally unstable precursors are used, when the solubility of the precursor in the solvent is low or when the intended metal loading is high.[17]

A typical impregnation consist of three elementary steps, namely: 1) impregnation, 2) drying and 3) calcination, if necessary followed by an activation (Figure 1).[15,17]

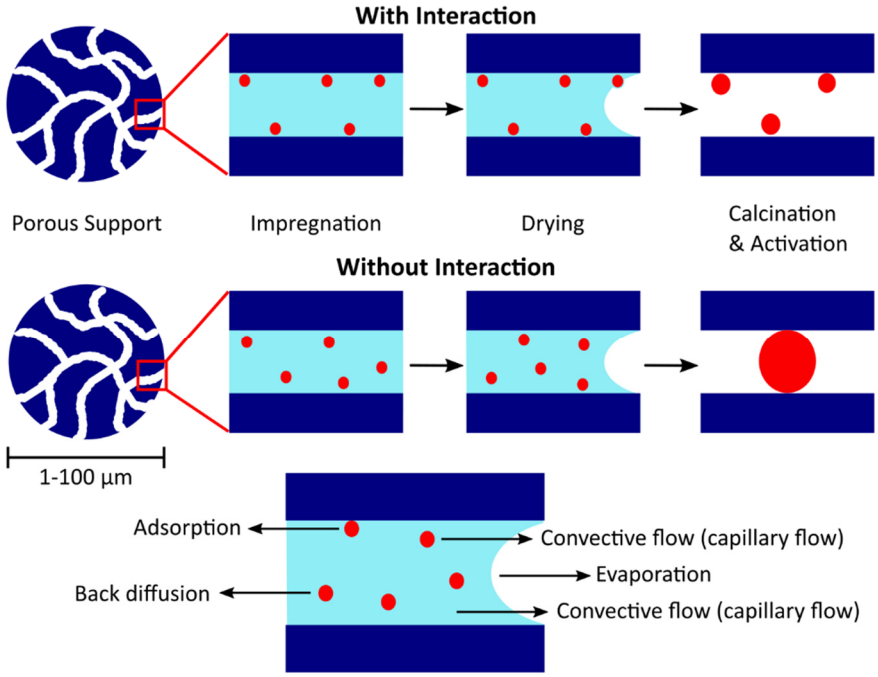

Figure 1 Schematic representation of impregnation as synthesis technique for supported nanoparticles in the two limiting cases of impregnation: with interaction (top) and without interaction (centre), and the different transport phenomena that occur during drying (bottom) (support: dark blue; solvent: light blue; metal (precursor): red).[17]

Before impregnation can start, a suited porous support must be chosen. The majority of supported metals is deposited on metal oxides such as Al_2O_3, SiO_2 and TiO_2, but also carbonaceous materials and polymers are commonly used supports.[5,11,14,18–23] These relatively cheap supports have a high porosity, remarkably increasing the surface area. However, the porosity of the support can also determine the size of the formed nanoparticles, as can be seen in Figure 1. Well-defined crystalline microporous materials are good support candidates for this pore-confinement synthesis strategy. Zeolites e.g. are already used for a long time as support in the chemical industry, but together with other structured microporous materials such as metal-organic-frameworks (MOFs) they are gaining more and more interest.[24–28]

For the first step, the impregnation, the precursor is dissolved in a solvent. For inorganic precursors this solvent is mostly water because it has a high precursor solubility, is readily available, cheap and non-toxic thus simple to use.[12,15] However, also alcohols such as ethanol are used as an impregnation solvent because it is able to reduce the metal precursor already during impregnation as it acts as an electron donor being oxidized to the corresponding ketone/aldehyde.[29] As already

mentioned, the precursor solution volume determines whether the impregnation is classified as 'dry' or 'wet' impregnation. For the silica impregnated silver catalysts used further in this work the precursor solution mostly equals the pore volume, the so-called dry or incipient wetness impregnation (IWI). A key parameter in the impregnation step in IWI is the pore filling. To ensure that the support is completely filled, nitrogen physisorption is typically performed to determine the micro- and mesoporous volume. Differential scanning calorimetry (DSC) and cryo-electron tomography furthermore confirmed that upon impregnation 97 % of the pore volume is homogeneously filled.[30,31] As mentioned, another important characteristic of impregnation is the interaction between precursor and support. When the metal precursor does not significantly adsorb onto the support surface, as is the case for silica and silver nitrate used in this work, incipient wetness impregnation leads to a uniform distribution of the precursor throughout the pore system of the support.[32] In an impregnation with interaction the distribution of the precursor largely depends on the equilibrium constant, the relative concentration of precursor compared to the number of active sites on the support, and whether a competitor is used.[13]

During the second step, the drying, the liquid inside the pores is transported to the external support surface by a flow of water vapour through the pores or by a convective flow of liquid.[17] Due to solvent evaporation the precursor concentration locally reaches supersaturation and the precursor crystallizes inside the pores. Depending on the strength of interaction between precursor and support, drying might alter the distribution after impregnation. In an impregnation with interaction, drying conditions rarely influence the metal distribution, in an impregnation without interaction on the contrary, the drying step is known to induce spatial variation in loading, giving rise to various distribution profiles of the final metal nanoparticles inside the support.[17,33] The importance of the drying step and the resulting metal distribution thus depend on the nature of support and precursor, the pre-treatment of the support particle, pH and concentration of the impregnation solution and the type of drying used.[34] Visual examination and transmission electron microscopy (TEM) can be used to characterize e.g. nanoparticle size distribution and compare different drying methods.[31,34,35]

Although impregnation and drying are generally the most crucial steps in the synthesis procedure,[15] calcination might also influence the final metal nanoparticle size and distribution via nanoparticle growth or sintering as a result from Ostwald ripening. Sintering can be avoided or slowed down when the metal dispersion is very high, as is typically the case in ion exchange and with uniform distributions after impregnation and drying. The influence of calcination conditions on the resulting nanoparticle size and distribution is typically assessed via TEM, an example is given

below in Figure 2.[36] More information on the used characterisation methods and specific examples are given in the following paragraph.

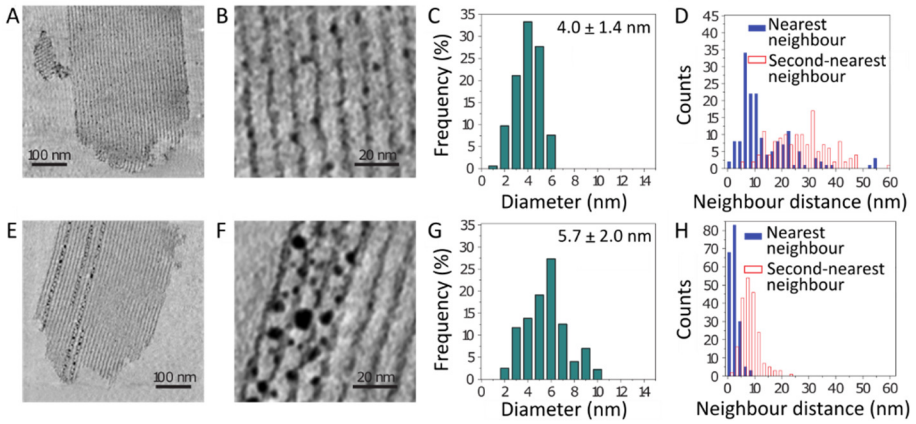

Figure 2 A-D) N_2-calcined CuZn/SBA-15 catalyst comprised Cu-particles with narrow size distribution (4.0±1.4 nm) that, in marked contrast to nitric oxide calcined (2 % NO/N_2) catalyst **(E-H)**, were evenly distributed throughout the entire pore system. **A, B, E, F)** Cross-sections through 3D-reconstructed electron tomograms (nanoparticles as black dots), **C, G)** surface-weighted Cu nanoparticle size histograms**, D, H)** surface-to-surface nearest neighbour distance histograms [reproduced with permission from ref. 36].

1.1.2 Characterisation

Supported metal nanoparticle catalysts are mainly characterised for the resulting nanoparticle size, crystal structure and distribution inside the support.[11] The characterisation techniques used to obtain these values can be divided into bulk averaging techniques and high spatially resolving techniques, providing either averaged properties or local information.

1.1.2.1 Bulk Averaged Characterisation

***X-ray diffraction (XRD)*:** In X-ray diffraction the peak width of the Bragg reflection is determined by the finite size of the nanoparticles, this line-broadening is described by the Scherrer equation and can thus be used to determine the volume averaged nanoparticle size.[37] Metallic silver nanoparticles for example show diffraction peaks at 2θ values of 38.1°, 44.3°, 64.4°, and 77.5° resulting from reflections at the [111], [200], [220], and [311] planes respectively.[38,39] For very small particles, e.g. 1 nm silver containing of about 50 Ag atoms, the thickness is too small to generate significant Bragg diffraction to observe in powder XRD.

UV/Visible-Diffuse Reflectance Spectroscopy (UV/Vis-DRS): The optical properties of metal nanoparticles are largely determined by their size, shape and refractive index (RI) of the surrounding medium. For nanoparticles of 2 nm and larger surface

plasmon resonance (SPR), light absorption causing electrons to oscillate in the conduction band upon white light illumination, can be used to obtain this information.[40,41] Simulations of Ag nanoparticle size on supports with refractive indexes increasing from 1.0 to 1.3 and 1.5 show a red shift of the maximum, but below 10 nm there is no change in maximum absorbance with size anymore.[42] Experimental UV-Vis DRS measurements of silver nanoparticles of about 3 nm supported in a mesoporous silica and on a Ni-MOF exhibit characteristic plasmon absorption peaks at respectively 415 nm and 449 nm.[43,44]

***Chemisorption*:** Chemisorption of a probe molecule at the metal nanoparticle surface atoms can be used to determine the dispersion and average size of the metal nanoparticles, given that the chemisorption stoichiometry is known. CO-adsorption is used for supported platinum or palladium catalysts, O_2/H_2 chemisorption on the other hand is reported for supported silver catalysts.[45] The size obtained with chemisorption techniques yields an approximate value, particularly in the case of silver in which subsurface oxygen chemisorption and bulk oxidation may occur at higher oxygen coverages.[45]

***Inductively Coupled Plasma-Atomic Emission Spectroscopy (ICP-AES)*:** After complete dissolution of the supported metal sample, the solution containing the dissolved catalyst can be analysed via atomic spectroscopy. Currently ICP-AES is a very popular approach in which the atoms are ionized in a plasma, based on the element-specific emission wavelengths elemental analysis of the whole sample can be performed.

Other bulk averaging characterisation techniques that are often used comprise Electron Paramagnetic or Electron Spin Resonance (EPR/ESR),[30] H_2-Temperature Programmed Desorption and Reduction, N_2-physisorption[46] and vibrational IR and Raman spectroscopy.[30]

1.1.2.2 Characterisation with high spatial resolution

In microscopy, the ultimate resolution is limited by the wavelength used to visualize the sample under study. However, an elegant solution to increase resolution beyond this limit is used in super resolution fluorescence microscopy, precise localisation of fluorescent molecules allows reconstruction of an image with nanometre precision.[47] Since wavelength and resolution are inversely related by the Rayleigh criterion,[48] the small wavelength of electrons and X-rays allows atomic resolution and can thus be used for catalyst characterisation with high spatial resolution. ***Transmission Electron Microscopy (TEM)*:** When a very thin sample, typically < 100 nm, is irradiated with an electron beam, the transmitted electrons can be used to create an image with atomic resolution and reveal details about the support and nanoparticle crystal structure, about the size and about the support-metal

nanoparticle interaction.[15] TEM is one of the most widespread microscopy techniques in catalysis research of supported metal nanoparticles because of the atomic resolution that is possible.[11,49] To obtain sufficiently thin samples the catalysts is often dissolved or ground before analysis[14,15,46] and for statistical relevance, multiple individual particles are imaged.[22] Although the high energy electron beam is necessary to obtain atomic resolution, the support might be damaged by this beam and stability of the supported nanoparticles is lost. For oxides this effect is rather limited, but for MOFs damage can be significant and induce reaction and metal nanoparticle restructuring. As a consequence of destruction of the MOF-support silver nanoparticles aggregate and the observed size is an overestimation of the supported nanoparticle size, reaction of silver clusters supported on alumina was also observed.[18,30]

***Scanning Electron Microscopy (SEM)*:** SEM is a basic characterisation technique that also uses an electron beam to visualize the sample; although atomic resolution cannot be achieved in comparison to TEM, nanoparticles can still be easily resolved and since it is easier to operate, SEM is more routinely used. Upon scanning the sample under study with a beam of high energy electron irradiation, secondary electrons or backscattered electrons are emitted by the sample. These electrons are captured with a specific detector and used to reconstruct the image.[15] Since the number of backscattered electrons is related to the atomic weight and density, backscattered scanning electron microscopy is often used to enhance the contrast between the metal nanoparticle and the support, usually the former has a higher atomic weight, creating a brighter signal.[50]

Energy-dispersive X-ray spectroscopy (EDX): The high energy electrons from the electron beam used in electron microscopy can also excite an electron in an orbital shell of the atom under study, when this excited electron returns to its ground state an X-ray is emitted with a characteristic wavelength for every element and elemental analysis of the highly local probed area or spot can be performed. The thickness of the layer analysed by EDS is in the micrometre range.[51]

***X-ray Absorption Fine structure Spectroscopy (XAFS)*:** XAFS is a commonly used term to include 2 characterisation methods that are based on the same principle: Extended X-ray Absorption Fine Structure (EXAFS) and X-ray Absorption Near Edge Spectroscopy (XANES). X-ray absorption by the supported metal atoms is influenced by its local coordination. Interference of electron waves between atoms gives rise to fine structure in the spectrum and provides local structure information on distance, number and type of neighbours of the absorbing atom.[52] Based on the metal-metal coordination number, an estimation of the average nanoparticle size and dispersion can then be made.[18,53] However, silver is highly mobile under the X-ray irradiation

dose that is used in EXAFS, so the observed silver cluster size might not reflect the actual size in the catalytic sample.[54]

1.1.3 Heterogeneity

The average properties that result from bulk measurements assume a uniform distribution of the property for the average to capture the real sample properties. In spatially resolved measurements the information is only useful if a representative subset of the sample is measured. All the characterisation methods discussed above assume thus homogeneous batches, however in literature various types and degrees of heterogeneity in supported metal catalysts have been reported. A summary is given below, with a first paragraph on the extensively studied heterogeneous distribution of metal nanoparticles in millimetre sized catalyst bodies.

1.1.3.1 Heterogeneous metal distribution profiles in catalyst bodies

Supported metal catalysts used in industry are commonly synthesized via impregnation and supported onto millimetre sized catalyst bodies. Although originally homogeneous or uniform distribution of the metal inside the body was aimed for, potential positive effects of heterogeneous concentration distributions on the catalytic performance gained researchers interest from the 1960s and synthesis procedures were developed to deliberately reach a certain non-uniform metal distribution inside the support.[33] Typically these distribution profiles are termed 'uniform', 'egg-shell', 'egg-yolk' or 'egg-white' (Figure 3). The final distribution depends on support and metal precursor used, but is also severely influenced by the impregnation, drying, calcination and reduction during the preparation.[33] Based on the broad overview of experimentally obtained profiles reported in literature and extensive modelling of the different impregnation steps Morbidelli, Gavriilidis and Varma[33] conclude that several experimental factors e.g. precursor solution concentration, pH, and temperature as well as drying conditions affect the final metal distribution.

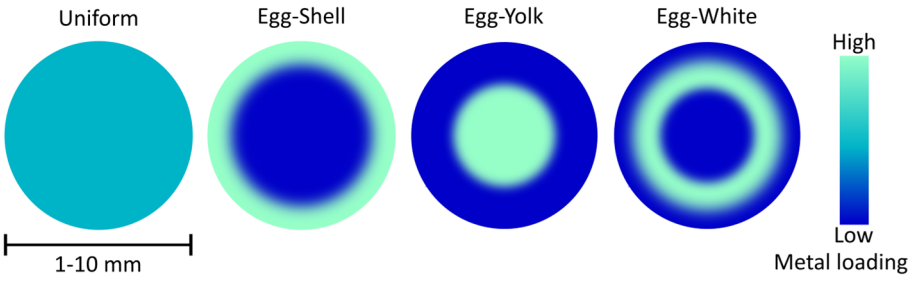

Figure 3 Different macroscopic distributions of catalytically active metal compounds inside catalyst support bodies.[12,15,17]

Typically the impregnated and calcined bodies are bisected to examine the metal distribution profile inside the support. Visual examination of the macroscopic distribution revealed the impact of drying on the Ni-distribution inside an alumina monolith (Figure 4A).[34] Photographs and Raman measurements of bisected 1 wt% Pd on γ-Al_2O_3 bodies clearly reveal an egg-white distribution when impregnation is performed in HCl at pH 1, while an egg-shell distribution is obtained after impregnation at pH 5 (Figure 4B).[55] Magnetic resonance imaging on the contrary can be used to image the distribution without cutting the pellet and also reveals egg-white or egg-shell profiles after Ni-impregnation in alumina bodies depending on the impregnation solution pH (Figure 4C).[56]

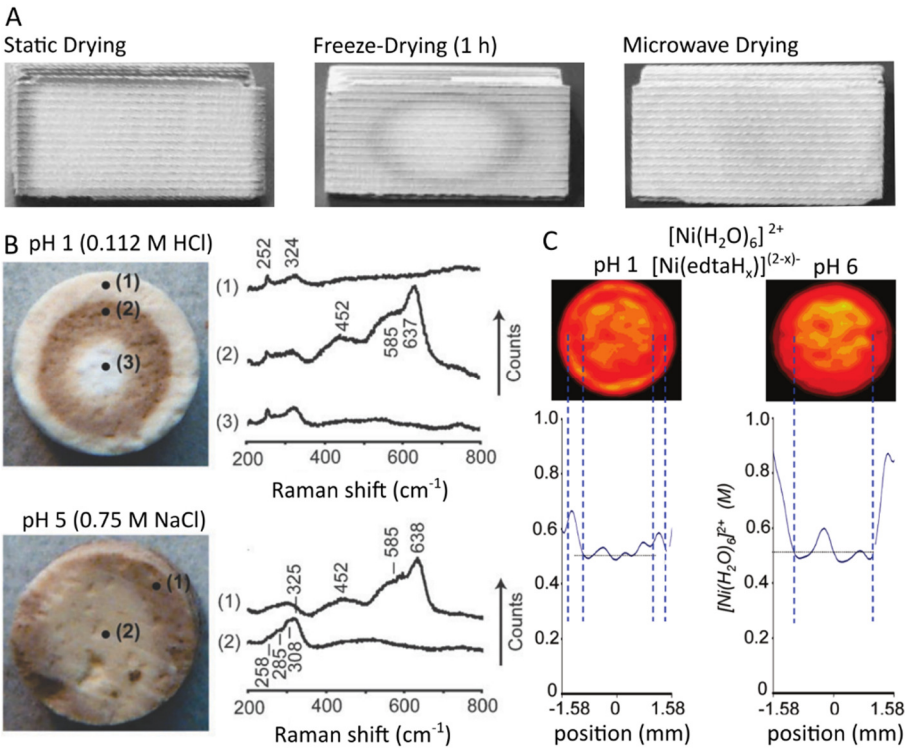

Figure 4 A) Visual examination of the influence of the drying step on the macroscopic distribution of Ni on alumina monoliths (L = 40 mm) after bisecting the catalyst bodies.[34] **B)** Photographs and Raman measurements after impregnation and calcination on bisected catalyst bodies (L, ø = 3 mm) reveal non-uniform macroscopic distributions in 1 wt% Pd/γ-Al_2O_3 as function of the pH of the impregnation solution: brown colour = oxidic Pd (Raman: 452, 585, 637 cm^{-1}); white = chlorinated Pd (Raman: 252, 324 cm^{-1}).[55] **C)** Magnetic Resonance Imaging after impregnation reveals non-uniform profiles in Ni/γ-Al_2O_3 catalyst bodies (L = 12 mm, ø = 3,85 mm); red colour = high Ni^{2+} concentration, yellow = lower concentration).[56]

Although in these last two examples the heterogeneous distribution profile arises from the impregnation step, redistribution of the metal precursor during drying can strongly affect the final distribution profile as indicated by the first example. The drying step is divided into different stages based on the drying rate (increasing, constant and falling-rate period) during which the liquid phase might be converted from a continuous to a pendular state. During the constant rate period vapour removal occurs at the external surface of the support and solvent flow towards the surface is high enough to maintain a constant drying rate; at a certain point the liquid flow can no longer keep up with the evaporation rate resulting in a receding drying front inside the support and a decreasing drying rate.[17] Typically two limiting drying regimes are identified based on the drying rate, namely fast and slow drying.[32.33] Slow drying can be defined as the drying regime in which the constant-rate period predominates, whereas in fast drying the falling-rate period is reached rapidly.[17,32] On a support with a narrow range of pore sizes and if vapour removal is much slower than diffusive transport, during slow drying the drying front recedes towards the centre of the support granule and might lead to an accumulation of the metal in the granule centre if interaction between support and precursor is weak.[13,33] However, as the constant drying rate period predominates during slow drying, liquid transport towards the external support surface where evaporation that takes place, might lead to deposition of the precursor on the external edge of the support granule.[17,32] During fast drying, liquid evaporation is much faster than capillary flow and precursor diffusion (Figure 5A-B).[33] In literature contradicting statements about the effect of fast drying on the active phase distribution can be found, with both an accumulation of catalyst precursor in the centre of the granule as well as at the outer surface.[32] Drying experiments with sol-gel silica spheres with high surface area (230 m^2/g) and narrow pores (7-8 nm) at 80 °C indicate that most of the water is evaporated during the constant rate period, which means that transport of water to the external surface of the spheres is occurring more rapidly than evaporation.[32] Most probably the liquid solution is spread over the hygroscopic silica surface and transported to the external surface of the support granule via a film of liquid between elementary sol-gel support particles (Figure 5C).[32] The accumulation of metal towards the outer surface of the granule can also be explained by the increased precursor concentration at the surface where evaporation occurs, resulting in a large osmotic pressure. This osmotic pressure induces water to flow towards the surface, creating emptied zones inside the support and transport of the weakly interacting precursor towards the outer surface. Since capillary force is responsible for larger pores to be emptied first in favour of smaller pores (Figure 5D), emptied zones can also result from capillary flow towards narrow pore mouths at the granule surface.[32,34] But as mentioned, the influence of drying is also dependent on the solubility of the precursor, the precursor solution concentration, pH and viscosity.

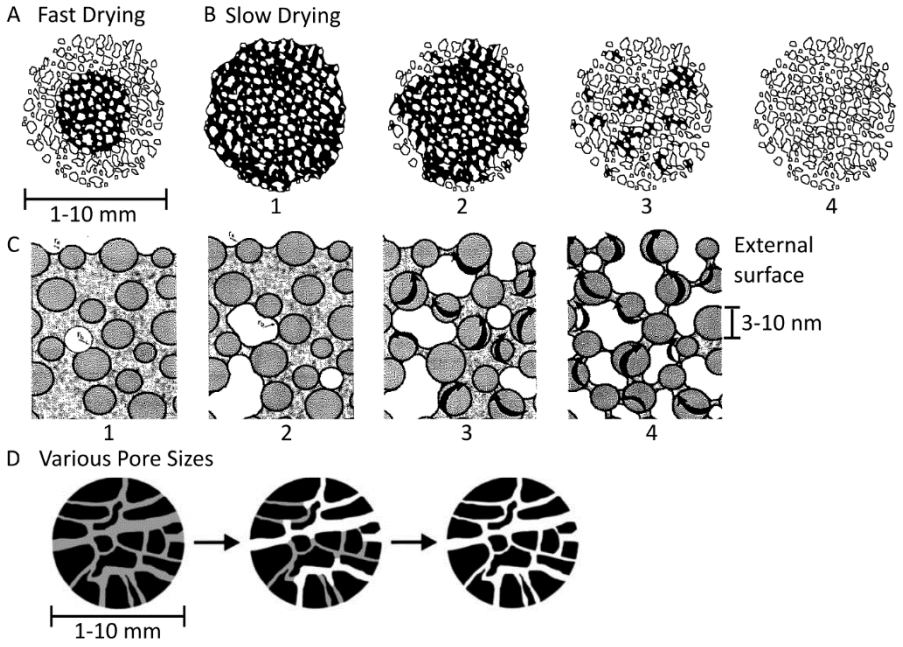

Figure 5 Water removal during drying. **A-B)** Drying regimes (white = porous and dry support granule; black = water): Fast Drying; liquid evaporation is much faster than capillary flow and precursor diffusion, which might result in metal accumulation in the pellet centre; Slow drying, evaporation occurs at the pellet surface, after partially receding into the pellet, the evaporation front breaks down, forming isolated liquid phase regions.[33] **C)** schematic representation of liquid flow during drying of porous supports: (1-2) formation of gas bubbles within the liquid due to the suction of narrow pore mouths at the external support surface, (3-4) emptying of the pores resulting from transport of liquid to the external surface of the support via narrow voids at the contact areas of elementary support particles.[32] **D)** Large pores are emptied in favour of small pores as a result of different capillary pressure.[34]

1.1.3.2 Intraparticle Heterogeneity

In contrast to millimetre sized catalyst bodies used in industry, at the laboratory scale metal nanoparticles are typically supported onto micrometre sized granules. Probing catalyst heterogeneity is thus not possible at this scale without the use of microscopes. Although laboratory catalysts are mostly assumed homogeneous in properties, intraparticle variations in defects, catalytic sites, nanoparticle size, dispersion and distribution have been shown for various catalytic systems. However these effects on supported metal catalysts at the micron granule scale is still largely unexplored. Fluorescence microscopy of single crystals is a powerful technique to reveal intraparticle heterogeneities. The catalytic conversion of a non-fluorescent substrate into emissive molecules allows to pinpoint the location of catalytic activity very precisely in 2D and 3D.[47] In contrast to what would be intuitively expected,

confocal fluorescence imaging showed that defect sites in MOF crystals are heterogeneously distributed inside the MOF-crystal, more specifically for solvothermally synthesised HKUST-1 they are formed along the [111] crystallographic planes (Figure 6A).[57] In ZSM-5 zeolite crystals, the heterogeneous distribution of both activity and the different reaction products after longer reaction, was also related to the different crystal planes and visualized by confocal microscopic imaging (Figure 6B).[58] A similar crystal plane dependency in photocatalysis was found on TiO_2 crystals (Figure 6C).[59] Furthermore, mapping of the spatial distribution of catalytic activity by counting single turnover events on layered double hydroxide catalysts indicated that the type of reaction that is catalysed is not homogeneous. More specifically, transesterification is detected on the entire outer crystal surface whereas ester hydrolysis occurs only on the lateral [1010] crystal planes (Figure 6D).[60]

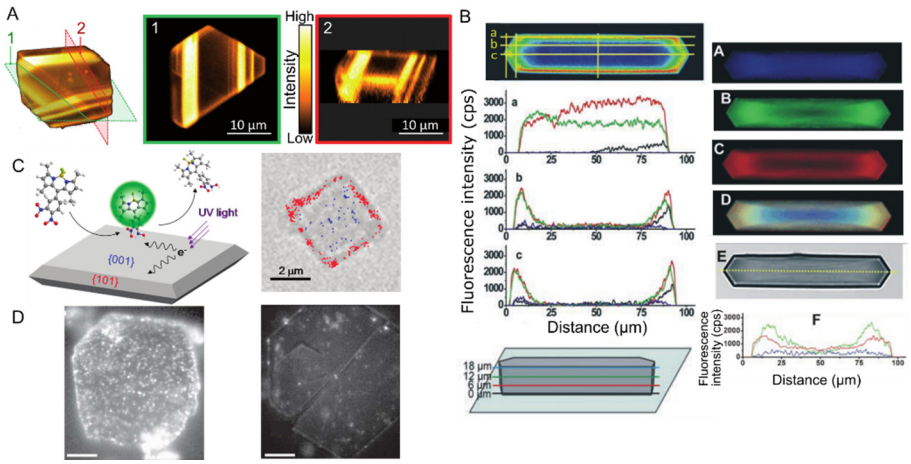

Figure 6 Confocal fluorescence microscopy studies revealing intraparticle heterogeneity. **A)** defect sites in metal-organic framework HKUST-1 crystals are heterogeneously distributed: cross sections through the crystal (yellow = defects), the angle between high fluorescence intensity and crystal surface indicated that defects are formed along the [111] crystal planes.[57] **B)** heterogeneous distribution in individual ZSM-5 zeolite crystals of activity (left, probed by fluorogenic condensation of furfuryl alcohol, intensity measured along different lines, a-c, at different depths, 0-6-12-18 µm from the bottom of the crystal indicated by black, red, green and blue lines respectively) and reaction products after longer reaction (right, A-C: colours represent different reaction products, measured in different detector channels, D: overlay image, E-F: line scan and relative intensity from channels A-C).[58] **C)** crystal plane dependency of photocatalytic generation of fluorescent HN-BODIPY from non-fluorescent DN-BODIPY on TiO_2 (red, blue dots: single product molecules located on the [101] and [001] crystal planes).[59] **D)** heterogeneity in 5-carboxyfluorescein diacetate conversion catalysed by layered double hydroxides: transesterification (left) and hydrolysis (right) occur at different crystal planes (white dots: single product molecules, scale bar = 5 µm).[60]

Also for supported metal catalysts intraparticle heterogeneities are reported. Here, electron tomography revealed a non-uniform distribution of Ni on SBA-15; combined characterisation with XRD and physisorption yielded well-dispersed small NiO nanoparticles by calcination in NO/He instead of air.[61] Freeze-drying of Co- and Ni-impregnated SBA-15 resulted in a more homogeneous distribution[31] while vacuum drying at room temperature and calcination in N_2-flow of Cu-impregnated silica resulted in a narrow size distribution of the nanoparticles.[36] Munnik and co-workers used a fluidized bed drying approach to impregnate mesoporous silica granules with $Co(NO_3)_2$.[35] The drying temperature turned out to be crucial to obtain uniformly spaced small cobalt nanoparticles (3–4 nm).

1.1.3.3 Interparticle Heterogeneity

From the examples given above it is clear that intraparticle heterogeneities are encountered on a wide range of catalyst materials and can have a large impact on the catalytic performance. Interparticle heterogeneities on the contrary are less thoroughly investigated. While the crystal plane dependency inside ZSM-5 crystals was observed in at least 90 % of the individual zeolite crystals, a few crystals showed a different behaviour.[58] Aluminium zoning could be the origin of this interparticle heterogeneity. More pronounced intra- and interparticle heterogeneity was discovered in dealuminated mordenite zeolites by super-resolution fluorescence and Raman microscopy.[62] In the same dealuminated zeolite batch crystals displayed three main types of catalytic activity profiles. One third of the mordenite crystals displayed some activity at the outer region of the crystal and no catalytic activity at the crystals' centre, a quarter of the crystals displayed the inverse behaviour with a highly active core and a zone at the crystal periphery with a much lower activity and about 30 % of the crystals showed a transitional behaviour between an active core and homogeneous reactivity (Figure 7A). Another example of interparticle heterogeneity in catalytic activity within a zeolite batch was revealed by optical microscopy based on styrene oligomerisation induced pink coloration at crystal defects (Figure 7B).[63]

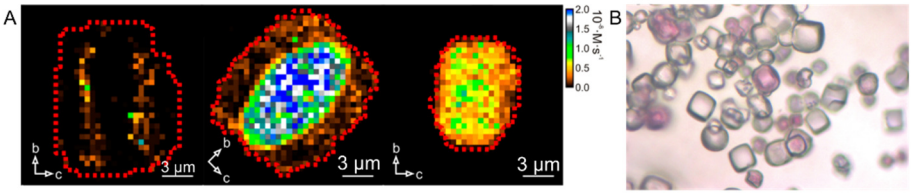

Figure 7 A) Super-resolution fluorescence microscopy reveals different stages of dealumination within the same batch of MOR zeolites via precise localisation of furfuryl alcohol oligomerisation products (colours indicate reaction product concentration: red = low, blue = high).[62] **B)** interparticle heterogeneity after styrene oligomerisation (pink colour) on H-SSZ-13 crystals (ø = 5 - 20 µm).[63]

In supported metal catalysts on the contrary, interparticle heterogeneities in catalyst loading or size are typically overseen because of the high resolution characterisation techniques, where there is no link between individual granules and the highly local characterisation or bulk averaging techniques in which all individual catalyst granules are assumed to be similar to the average obtained property. However, there is one example in which the Pt-loading varied between individual zeolite Y crystals with a factor of 35 as determined by 3D reconstruction of transmission electron microscopy images (Figure 8).[27]

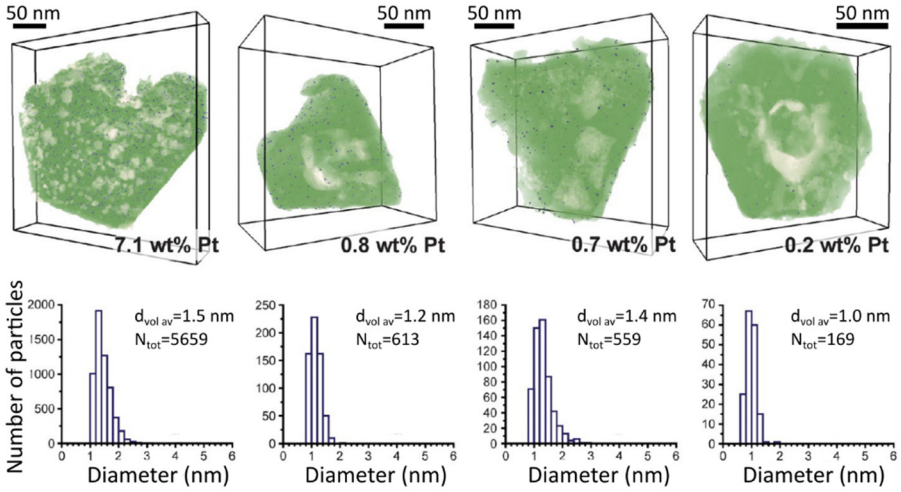

Figure 8 Electron tomography reveals 35-fold Pt-loading variation between individual zeolite Y particles. Top row shows 3D-representations of Pt/zeolite Y crystals with Pt loadings (wt%) calculated from semi-automated image analysis (zeolite crystals in green, Pt nanoparticles in blue, and mesopores in white). Bottom row shows Pt size distributions, volume-averaged Pt diameters, and total number of measured particles [Reproduced with permission from ref. 27, Copyright 2013 American Chemical Society].

1.2 CHEMOSELECTIVE CATALYSIS

Supported metal nanoparticles are obviously of interest for heterogeneous catalysis in general because a smaller particle size directly results in a larger surface to volume ratio for the same amount of metal.[64] Since the catalytically active sites are located on the surface in heterogeneous catalysts, decreasing the particle size to the nanometre range should increase the catalytic activity. However, catalytic activity and selectivity of supported metal nanoparticles are largely influenced by size, shape and distribution of the nanoparticles together with the accessibility and the support. Furthermore, activity and selectivity may tremendously differ when another metal with the same size and shape is used. As mentioned in the beginning of this introduction, nickel and Platinum Group Metal (PGM) nanoparticles are already used

for a long time; however non-PGM nanoparticles like gold and silver are gaining more and more attention because of their interesting properties at the nanometre scale.[41,64,65] Porous materials like silica, alumina, carbon, zeolites and metal-organic frameworks can be used to stabilize pre-formed nanoparticles and prevent their aggregation and hence loss in activity and/or selectivity, though more interestingly the pores of these supports can also be used to control the size of nanoparticles via pore confined synthesis strategies. A research area in which supported metal nanoparticles are heavily used is the chemoselective hydrogenation of unsaturated functionalized compounds to their unsaturated hydrogenated analogues.

1.2.1 Chemoselective hydrogenation

1.2.1.1 Nanometre sized silver as reduction catalyst

Silver is primarily known as oxidation catalyst in the industrial production of ethylene oxide via ethylene oxidation and dehydrogenation of methanol to formaldehyde.[66] Silver has a completely filled d-shell, suggesting it cannot dissociate hydrogen. Furthermore the hydrogen binding energy of silver is very low, implying silver is not a good hydrogenation catalyst. However, when small silver nanoparticles are formed, the electron density shifts from the 4d to the 5s orbital, making H_2 dissociation possible on silver.[67] Various research groups reported thus the use of supported silver nanoparticles as catalyst for the chemoselective hydrogenation of unsaturated aldehydes, esters and nitro compounds.[20,68–70] Furthermore, coordinatively unsaturated (CUS) silver sites were found to be crucial for the H_2 dissociation and since smaller particles possess more of these CUS sites, decreasing nanoparticle size was beneficial for the activity in the nitrostyrene hydrogenation.[18] Silver has an intrinsic chemoselectivity to reduce unsaturated nitroaromatics to the corresponding vinylanilines, which is not the case for PGMs.[65,71] Only by supporting nanosized crystals of non-chemoselective hydrogenation catalysts like Pt, Ru and Ni on TiO_2 and high temperature activation (450 °C), a high selectivity of 93 % to 4-vinylaniline was obtained in the hydrogenation of 4-nitrostyrene.[72]

1.2.1.2 Size does matter

Although contradictory statements concerning selective hydrogenation and structure sensitivity are encountered depending on the reaction under focus, nanoparticle size and support material play an important role in the selective carbonyl hydrogenation on supported silver catalysts.[73] In reactions of the unsaturated aldehydes crotonaldehyde and acrolein, an increased reactivity and selectivity to the corresponding allylic alcohols were observed with increasing silver nanoparticle size on silica[53] and TiO_2.[74] This observation was related to the larger fraction of silver [111] surfaces formed for 3 ± 2 nm sized silver nanoparticles. In the high pressure range on the contrary, the amount of allyl alcohol formed increased

when decreasing the silver nanoparticle size, which was explained by the larger fraction of low-coordinated surface sites on small nanoparticles, responsible for allyl alcohol formation.[75]

In contrast to the large amount of research reported on coordination and structure sensitivity in carbonyl group hydrogenation, less research has focussed on chemoselective hydrogenation of functionalized nitro-compounds. Besides the use of Raney nickel and Pt and Pd supported catalysts mentioned in the beginning of this introduction, hydrogenation of functionalized nitro aromatics with Au, Fe and Ag is gaining more and more interest.[76] Catalytic experiments with silver on Al_2O_3 and density functional theory calculations indicate that smaller nanoparticles are beneficial to reach high activity and selectivity in nitrostyrene hydrogenation.[77,78] This observation was rationalized by the rate-limiting dissociation of H_2 at coordinatively unsaturated silver sites and the adsorption geometry of the substrate.

1.2.1.3 Establishing structure-performance relationships

The above mentioned trends regarding the influence of size on the selectivity and activity of metal nanoparticles are typically obtained through bulk catalytic tests. By varying impregnation and other synthesis parameters, supported metal nanoparticle catalysts can be obtained with various sizes as determined by bulk and microscopic characterisation (vide supra), or as determined by the support pore dimension via pore confinement. An example is given in Figure 9A for gold nanoparticles on TiO_2. Typically the average nanoparticle size and dispersion are determined for a limited subset of the sample e.g. via high resolution transmission electron microscopy, assuming the observations can be extrapolated to the whole sample (Figure 9B). Finally the impact of different synthesis procedures and hence nanoparticle properties on the catalytic performance is probed via bulk reactions using milligrams to grams of powdered catalyst containing hundred thousands of individual catalyst support granules. The averaged catalytic performance of all these granules is then compared with the averaged nanoparticle property resulting from the highly resolved characterisation to establish structure-performance relationships. When establishing these relationships, a key parameter is the relation between the relative frequency of the different crystal planes and the nanoparticle diameter, as shown in Figure 9C. In this example the selectivity increase with size is attributed to the larger fraction of [111] planes that activate the substrate for reaction.[14] However, this conclusion and other structure-performance relationships in general are often drawn without considering the heterogeneities present in the catalyst bed. The examples given above however, clearly indicate that these heterogeneities might be present and influence the catalytic performance; but such detailed insights are masked in bulk catalytic tests.

A

Catalyst	Au content (wt%)	Preparation technique	d_{Au} (nm)[a]	msd (nm)[b]	D_{Au} (nm)[c]
Au/TiO_2-DP	1.7	Deposition–precipitation	5.3	0.3	0.36
Au/TiO_2-I	2.9	Impregnation	2.0	0.4	0.47
Au/TiO_2-SG	4.8	Sol–gel technique	1.1	0.2	0.78
Au/ZrO_2-F	1.0	Coprecipitation	1.4	0.3	0.63
Au/ZrO_2-DP	1.2	Deposition–Precipitation	3.8[d]	2.9	0.36
Au/SiO_2-IW	1.6	Incipient wetness	3.9	2.3	0.16
Au/SiO_2-CVD	2.4	Metal organic-chemical vapor deposition	1.4	0.3	0.70
Au/Al_2O_3/Al	0.02[f]	Dip-coating	NE	NE	NE

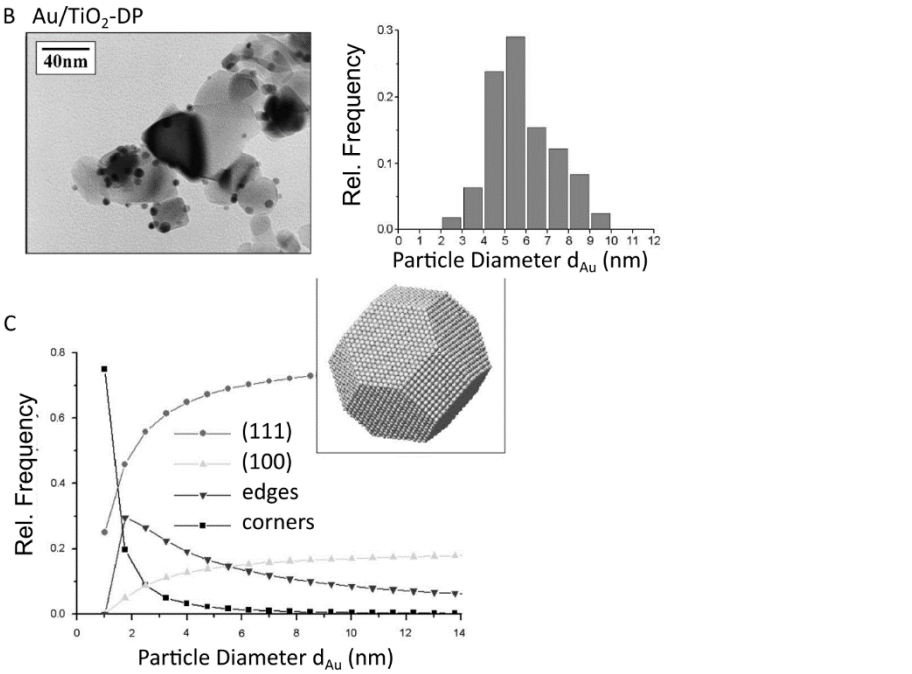

Figure 9 A-B) Structure-performance relationships are typically investigated by varying synthesis conditions and support that result in different nanoparticle sizes (table: a) mean diameter, b) mean square displacement, c) estimated dispersion, d) bimodal size distribution (2.1 and 7.4 nm), e) not estimated, f) estimated by removing the coating of two wafers), using size measurements based on TEM (B) and drawing conclusions from bulk catalysis tests. **C)** Catalytic activity is then related to the different fractions of specific crystal planes and egdes and corners on nanoparticles with different diameters.[14]

Another approach to examine the influence of nanoparticle properties on catalytic performance uses theoretical model calculations and density functional theory based simulations. Often these calculations are used to merely confirm the observations made by bulk catalytic experiments.[78] Although these calculations can be powerful to understand the phenomena happening at the atomic scale, modelling a complex system like heterogeneous catalysis is not straightforward and the underlying heterogeneity or other potentially important characteristics might be overlooked.

1.2.2 Meerwein-Ponndorf-Verley reduction

In 1925 Verley reported on an alternative route obtain allylic alcohols, more specifically the hydrogen transfer reaction of ketones to alcohols and its reverse reaction.[79] The same reversibility in the reduction of aldehydes with secondary alcohols was reported by Ponndorf one year later.[80] Meerwein and Schmidt made similar observations and pointed out one of the most interesting characteristics of this type of hydrogenation, namely that unsaturated ketones and aldehydes can be selectively reduced to the corresponding allylic alcohols without the risk of reducing the C=C double bound.[81] The transfer hydrogenation mechanism of aldehydes and ketones with alcohols was therefore named after three of these scientists, completed with the work done by Oppenauer on the reverse oxidation reaction resulting in the rather long name under which the hydrogen transfer reaction is known: Meerwein-Ponndorf-Verley-Oppenauer (MPVO) reaction.

1.2.2.1 From aluminium to zirconium catalysts

The catalysts used in the above-mentioned pioneering research were all metal alkoxides, mostly of aluminium.[79–81] Heterogenisation of the MPVO catalysts improved their recyclability and the presence of surface basicity or Lewis acidity turned out to be crucial for metal oxides to be good MPVO catalysts.[2] Even though research was initially focussed on aluminium, Zr-based MPV catalysts are gaining more and more interest. Optimisation led to the development of a Zr-grafted zeolite Beta catalyst that reached high cinnamyl alcohol yield within a reasonable reaction time. Even 100 % cinnamyl alcohol yield was reached by increasing the Lewis acidity of the Zr-atoms in zeolite Beta via a two-step post-synthesis modification.[82] Recently Zr-containing metal-organic frameworks (MOFs) are reported as MPV catalysts. MOFs are crystalline, porous materials composed of metal (oxide) nodes interlinked by polytopic organic ligands, forming three dimensional structures with well-defined cages and channels. UiO-66 is a zirconium-terephthalate MOF (Figure 10), which is best known for its high chemical and thermal stability and easy functionalisation. A major impact on the use of UiO-66, and other MOFs in general, in catalysis was the strategy of deliberately introducing defects into the MOF structure thereby increasing the availability and activity of Lewis acid metal sites.[57,83] To create these defect sites, ligands with a missing functional group or modulators can be added to the MOF synthesis mixture. Trifluoroacetate is used as a modulator in the UiO-66 synthesis, since it has a similar chemical functionality as the terephthalate linker, but has only one functional group, resulting in a more open framework with a large number of open sites.[84] These Zr-based modulated UiO-66 and UiO-66-NO_2 have already been successfully used as MPV reduction catalysts with *tert*-butylcyclohexanone as the reactant.[84]

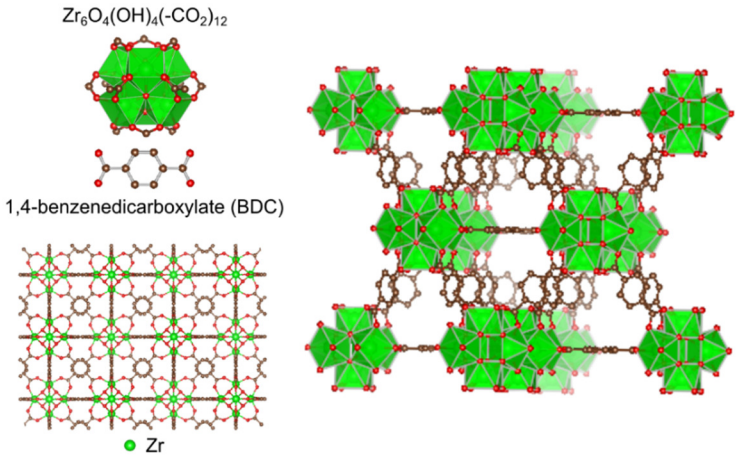

Figure 10 Schematic representation of the UiO-66 structure composed of metal (oxide) nodes ($Zr_6O_4(OH)_4(-CO_2)_{12}$; green octahedra) interlinked by polytopic organic ligands (1,4,-benzenedicarboxylate (BDC); C-atoms in brown, O-atoms in red).

1.2.2.2 Reaction mechanism

The high chemoselectivity in the MPV reduction directly stems from the reaction mechanism, which involves a six-membered ring formation in which both the hydride donor and acceptor are coordinated to the same metal active site and hydride transfer occurs with high selectivity. This reaction mechanism was first established for the homogeneous metal alkoxide catalysts (Figure 11A);[2] later on the same coordinative interaction and six-membered ring transition state was confirmed with the aluminium atoms of the heterogeneous zeolite Beta catalyst (Figure 11B).[85] The mechanism also reveals the role of the Lewis acid site, since in the first step metal-alkoxide bonds are formed with the substrate (Figure 11C). Detailed investigation of several heterogeneous zirconia catalysts resulted in the conclusion that also Zr forms a six-membered transition state (Figure 11D) and that surface hydroxyl groups are exchanged with the secondary alcohol hydride donor to start the catalytic reaction cycle.[86]

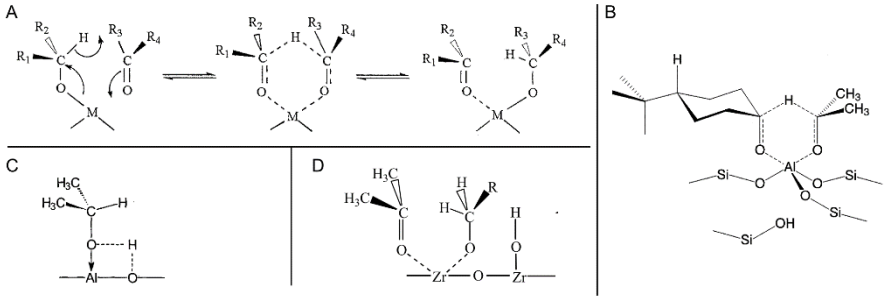

Figure 11 MPV mechanism reported for **A)** homogeneous alkoxides,[2] **B)** zeolite Beta,[85] **C)** Lewis acid site,[2] and **D)** hydrous Zr.[86]

1.3 SCOPE

Allylic alcohols and functionalized anilines are industrially important flavouring and fragrance compounds or valuable intermediates for pharmaceuticals, polymers and other fine chemicals.[2,65] In liquid phase hydrogenations forming these unsaturated compounds, supported platinum group metal (PGM) catalysts are often used. While PGMs often require complex doping schemes, silver has a very high intrinsic chemoselectivity in hydrogenations of polyfunctional molecules. To direct selectivity towards the desired products, there is a strong motivation to develop chemoselective reduction catalysts.

In this work the chemoselective hydrogenation of α,β-unsaturated aldehydes and 4-nitrostyrene will be investigated specifically. In the first experimental chapter (**Chapter 2**), the chemoselective reduction of 4-nitrostyrene using silver on silica catalyst, prepared via the standard incipient wetness procedure, is explored in detail. In contrast to traditional bulk averaging or spatially resolving characterisation methods that are typically used to study catalysts prepared at the lab scale, the most important characterisation technique used in this work will be optical microscopy. This technique is extremely well suited to uncover important interparticle silver loading heterogeneities at the single support particle level, and to link these to the catalytic performance at the same single crystal level. In the following chapter (**Chapter 3**) the origin of this interparticle heterogeneity in metal loading is investigated in detail using optical microscopy. The impregnation process is dissected into the individual synthesis steps to reveal the impact on the final interparticle silver distribution. Via simple optimisation of the impregnation, which is easy to implement in the lab and on large scale, the generation of a more homogeneous silver on silica catalyst is aimed.

An alternative strategy to form silver nanoparticles with strictly defined sizes is by pore confinement in crystalline microporous materials. The development of a new chemoselective nanometre sized silver reduction catalyst on an innovative material is pursued by pore confinement in a metal organic framework (MOF) (**Chapter 4**). Via MOF-supported silver catalysed hydrogenation of unsaturated aldehydes with H_2 at high temperature, not only the intrinsic high allyl alcohol selectivity of silver nanoparticles is probed; surprisingly the Lewis acidity of the support has a large impact on the reaction outcome. This finding was used to explore the power of Lewis acid sites in other metal-organic frameworks and resulted in a tremendous increase of the catalytic activity and allylic alcohol yield via metal-organic framework catalysed Meerwein-Ponndorf-Verley reduction (**Chapter 5**).

1.4 REFERENCES

(1) Belitz, H.-D.; Grosch, W.; Schieberle, P. *Food Chemistry*; Springer: Berlin, 2009; p 1070.
(2) Sheldon, R. A.; van Bekkum, H. *Fine Chemicals through Heterogeneous Catalysis*; WILEY-VCH Verlag GmbH Weinheim, 2001; p Chapter 8.
(3) Mikkola, J.; Virtanen, P.; Karhu, H.; Salmi, T.; Murzin, D. Y. *Green Chem.* **2006**, *8*, 197–205.
(4) Surburg, H.; Panten, J. *Common Fragrance and Flavor Materials*; Wiley-VCH Verlag GmbH & Co. KGaA: Weinheim, 2006; p 287.
(5) Yuan, Y.; Yao, S.; Wang, M.; Lou, S.; Yan, N. *Curr. Org. Chem.* **2013**, *17*, 400–413.
(6) Haake, M.; Gerlach, T.; Funke, F. Process for the selective liquid-phase hydrogenation of carbonyl compounds to the corresponding alcohols in the presence of a Pt/ZnO catalyst. EP1318129, 2003.
(7) Rylander, P.; Steele, D. Hydrogenation of unsaturated aldehydes to unsaturated alcohols. US3655777, 1972.
(8) Zhu, Y.; Chuah, G.; Jaenicke, S. *J. Catal.* **2006**, *241* (1), 25–33.
(9) Sanfilippo, D.; Rylander, P. *Ullmann's Encyclopedia of Industrial Chemistry*; 2012; pp 451–471.
(10) Vogt, P.; Gerulis, J. *Ullmann's Encyclopedia of Industrial Chemistry*; 2012; pp 699–718.
(11) White, R. J.; Luque, R.; Budarin, V. L.; Clark, J. H.; Macquarrie, D. J. *Chem. Soc. Rev.* **2009**, *38* (2), 481–494.
(12) Munnik, P.; de Jongh, P. E.; de Jong, K. P. *Chem. Rev.* **2015**, *115* (14), 6687–6718.
(13) Le Page, J.-F. *Applied heterogeneous catalysis*; Editions Technip.: Paris, 1988.
(14) Schimpf, S.; Lucas, M.; Mohr, C.; Rodemerck, U.; Brückner, A.; Radnik, J.; Hofmeister, H.; Claus, P. *Catal. Today* **2002**, *72*, 63–78.
(15) Ertl, G.; Knözinger, H.; Schüth, F.; Weitkamp, J. *Handbook of heterogeneous catalysis*; Wiley-VCH Verlag GmbH & Co. KGaA: Weinheim, Germany, 2008; p 3865.
(16) Jiao, L.; Regalbuto, J. R. J. R. *J. Catal.* **2008**, *260* (2), 329–341.
(17) de Jong, K. P. *Synthesis of Solid Catalysts*; Wiley-VCH: Weinheim, Germany, 2009; pp 1–401.
(18) Shimizu, K.; Miyamoto, Y.; Satsuma, A. *J. Catal.* **2010**, *270* (1), 86–94.
(19) Munnik, P.; Krans, N.; Jongh, P. De; Jong, K. De. *ACS Catal.* **2014**, *4*, 3219–3226.
(20) Bernas, H.; Simakova, I.; Prosvirin, I. P.; Mäki-Arvela, P.; Leino, R.; Murzin, D. Y. *Catal. Letters* **2012**, *142* (6), 690–697.
(21) Zhang, D. S.; Liu, X. Y.; Li, J. L.; Xu, H. Y.; Lin, H.; Chen, Y. Y. *Langmuir* **2013**, *29*, 11498–11505.
(22) Lyu, J.; Wang, J.; Lu, C.; Zhang, Q.; He, X.; Li, X. *J. Phys. Chem. C* **2014**, *118*, 2594–2601.
(23) Mäki-Arvela, P.; Hájek, J.; Salmi, T.; Murzin, D. Y. *Appl. Catal. A Gen.* **2005**, *292*, 1–49.
(24) Mäki-arvela, P.; Tiainen, L.; Lindblad, M.; Demirkan, K.; Kumar, N.; Sjoholm, R.; Ollonqvist, T.; Vayrynen, J.; Salmi, T.; Murzin, D. Y. *Appl. Catal. A Gen.* **2003**, *241*, 271–288.
(25) Neri, G.; Arrigo, I.; Corigliano, F.; De Luca, L.; Donato, A. *Catal. Letters* **2011**, *141* (11), 1590–1597.
(26) Hajek, J.; Kumar, N.; Francova, D.; Paseka, I.; Maki-Arvela, P.; Salmi, T.; Murzin, D. Y. *Chem. Eng. Technol.* **2004**, *27* (12), 1290–1295.
(27) Zečević, J.; van der Eerden, A. M. J.; Friedrich, H.; de Jongh, P. E.; de Jong, K. P. *ACS Nano* **2013**, *7* (4), 3698–3705.
(28) Guo, Z.; Xiao, C.; Maligal-Ganesh, R. V; Zhou, L.; Goh, T. W.; Li, X.; Tesfagaber, D.; Thiel, A.; Huang, W. *ACS Catal.* **2014**, *4*, 1340–1348.
(29) Houk, R. J. T.; Jacobs, B. W.; El Gabaly, F.; Chang, N. N.; Talin, A. A.; Graham, D. D.; House, S. D.; Robertson, I. M.; Allendorf, M. D. *Nano Lett.* **2009**, *9* (10), 3413–3418.
(30) Eggenhuisen, T. M.; Van Steenbergen, M. J.; Talsma, H.; de Jongh, P. E.; de Jong, K. P. *J. Phys. Chem. C.* **2009**, 16785–16791.
(31) Eggenhuisen, T. M.; Friedrich, H.; Nudelman, F.; Zecevic, J.; Sommerdijk, N. A. J. M.; de Jongh, P. E.; de Jong, K. P. *Chem. Mater.* **2013**, *25*, 890–896.
(32) Regalbuto, J. *Catalyst Preparation: Science and Engineering*; CRC Press: Boca Raton, 2016; p 488.
(33) Morbidelli, M.; Gavriilidis, A.; Varma, A. *Catalyst design: Optimal Distribution of Catalyst in Pellets, Reactors, and Membranes*; Cambridge University Press, 2001; p 227.
(34) Vergunst, T.; Kapteijn, F.; Moulijn, J. A. *Appl. Catal. A Gen.* **2001**, *213*, 179–187.
(35) Munnik, P.; de Jongh, P. E.; de Jong, K. P. *J. Am. Chem. Soc.* **2014**, *136*, 7333–7340.
(36) Prieto, G.; Zečević, J.; Friedrich, H.; de Jong, K. P.; de Jongh, P. E. *Nat. Mater.* **2013**, *12* (1), 34–39.
(37) Dinnebier, R.; Billinge, S. *Powder diffraction: theory and practice*; The Royal Society of Chemistry: Cambridge, 2008; pp 17–19.

(38) Lu, J.; Bravosuarez, J.; Takahashi, a; Haruta, M.; Oyama, S. *J. Catal.* **2005**, *232* (1), 85–95.
(39) Montazer, M.; Alimohammadi, F.; Shamei, A.; Rahimi, M. K. *Carbohydr. Polym.* **2012**, *87* (2), 1706–1712.
(40) Liz-Marzan, L. M. *Mater. Today* **2004**, *7* (2), 26–31.
(41) Díez, I.; Ras, R. H. A. *Nanoscale* **2011**, *3* (5), 1963–1970.
(42) Quinten, M. *Appl. Phys. B Lasers Opt.* **2001**, *73* (4), 317–326.
(43) Besson, S.; Gacoin, T.; Boilot, J. **2003**, 360–361.
(44) Moon, H. R.; Kim, J. H.; Suh, M. P. *Angew. Chem. Int. Ed. Engl.* **2005**, *44* (8), 1261–1265.
(45) Arve, K.; Kannisto, H.; Ingelsten, H. H.; Eränen, K.; Skoglundh, M.; Murzin, D. Y. *Catal. Letters* **2011**, *141* (5), 665–669.
(46) Mhamdi, M.; Khaddar-Zine, S.; Ghorbel, A. *Appl. Catal. A Gen.* **2009**, *357* (1), 42–50.
(47) Roeffaers, M. B. J.; Hofkens, J.; De Cremer, G.; De Schryver, F. C.; Jacobs, P. a.; De Vos, D. E.; Sels, B. F. *Catal. Today* **2007**, *126* (1-2), 44–53.
(48) Murphy, D. B. *Fundamentals of light microscopy and electronic imaging*; John Wiley and Sons: New York, 2001.
(49) Claus, P.; Bru, A.; Mohr, C.; Hofmeister, H. *J. Am. Chem. Soc.* **2000**, *122*, 11430–11439.
(50) Liv, N.; Zonnevylle, C. A.; Narvaez, A. C.; Effting, A. P. J.; Voorneveld, P. W.; Lucas, M. S.; Hardwick, J. C.; Wepf, R. a; Kruit, P.; Hoogenboom, J. P. *PLoS One* **2013**, *8* (2).
(51) Villegas, L.; Masset, F.; Guilhaume, N. *Appl. Catal. A Gen.* **2007**, *320*, 43–55.
(52) Niemantsverdriet, J. W. *Spectroscopy in Catalysis*; WILEY-VCH: Weinheim, Germany, 2007; p 325.
(53) Wei, H.; Gomez, C.; Liu, J.; Guo, N.; Wu, T.; Lobo, R.; Christopher, L.; Lobo-Lapidus, R.; Marshall, C. L.; Miller, J. T.; Meyer, R. J. *J. Catal.* **2013**, *298*, 18–26.
(54) Coutino-Gonzalez, E.; Grandjean, D.; Roeffaers, M.; Kvashnina, K.; Fron, E.; Dieu, B.; De Cremer, G.; Lievens, P.; Sels, B.; Hofkens, J. *Chem. Commun.* **2014**, *50* (11), 1350–1352.
(55) Espinosa-Alonso, L.; de Jong, K. P.; Weckhuysen, B. M. *Phys. Chem. Chem. Phys.* **2010**, *12* (1), 97–107.
(56) Espinosa-Alonso, L.; Lysova, A. A.; de Peinder, P.; de Jong, K. P.; Koptyug, I. V; Weckhuysen, B. M. *J. Am. Chem. Soc.* **2009**, *131* (14), 6525–6534.
(57) Ameloot, R.; Vermoortele, F.; Hofkens, J.; De Schryver, F. C.; De Vos, D. E.; Roeffaers, M. B. J. *Angew. Chem. Int. Ed. Engl.* **2013**, *52* (1), 401–405.
(58) Roeffaers, M. B. J.; Sels, B. F.; Uji-i, H.; Blanpain, B.; L'hoëst, P.; Jacobs, P. A.; De Schryver, F. C.; Hofkens, J.; De Vos, D. E. *Angew. Chem. Int. Ed. Engl.* **2007**, *46* (10), 1706–1709.
(59) Tachikawa, T.; Yamashita, S.; Majima, T. *J. Am. Chem. Soc.* **2011**, *133*, 7197–7204.
(60) Roeffaers, M. B. J.; Sels, B. F.; Uji-I, H.; De Schryver, F. C.; Jacobs, P. a; De Vos, D. E.; Hofkens, J. *Nature* **2006**, *439* (7076), 572–575.
(61) Sietsma, J. R.; Friedrich, H.; Broersma, A.; Versluijs-Helder, M.; Jos van Dillen, A.; de Jongh, P. E.; de Jong, K. P. *J. Catal.* **2008**, *260* (2), 227–235.
(62) Liu, K.; Kubarev, A. V; Van Loon, J.; Uji-i, H.; De Vos, D. E.; Hofkens, J.; Roeffaers, M. B. J. *ACS Nano* **2014**, *8* (12), 12650–12659.
(63) Sommer, L.; Svelle, S.; Lillerud, K. P.; Stöcker, M.; Weckhuysen, B. M.; Olsbye, U. *Langmuir* **2010**, *26* (21), 16510–16516.
(64) Stark, W. J.; Stoessel, P. R.; Wohlleben, W.; Hafner, A. *Chem. Soc. Rev.* **2015**.
(65) Corma, A.; Serna, P. *Science* **2006**, *313* (July), 332–335.
(66) Brumby, A.; Braumann, P.; Zimmermann, K.; Van Den Broeck, F.; Vandevelde, T.; Goia, D.; Renner, H.; Schlamp, G.; Weise, W.; Tews, P. T. *Ullmann's Encyclopedia of Industrial Chemistry*; Wiley-VCH Verlag GmbH & Co, 2012; p vol. 33 p 15–94.
(67) Sa, J.; Srebowata, A. *Hydrogenation with Low-Cost Transition Metals*; CRC Press: Boca Raton, 2016.
(68) Claus, P. *Top. Catal.* **1998**, *5*, 51–62.
(69) Yin, A.; Guo, X.; Dai, W.; Fan, K. *Chem. Commun.* **2010**, *46* (24), 4348–4350.
(70) Steffan, M.; Jakob, a; Claus, P.; Lang, H. *Catal. Commun.* **2009**, *10* (5), 437–441.
(71) Furukawa, S.; Yoshida, Y.; Komatsu, T. *ACS Catal.* **2014**, *4*, 1441.
(72) Corma, A.; Serna, P.; Concepcion, P., Calvino, J. J. *J. Am. Chem. Soc.* **2008**, *130* (9), 8748–8753.
(73) Corain, B.; Schmid, G.; Toshima, N. *Metal Nanoclusters in Catalysis and Materials Science: The Issue of Size Control*; Elsevier: Amsterdam, 2007; p 470.
(74) Claus, P.; Hofmeister, H. *J. Phys. Chem. B* **1999**, *103* (14), 2766–2775.

(75) Bron, M.; Teschner, D.; Knopgericke, a; Steinhauer, B.; Scheybal, a; Havecker, M.; Wang, D.; Fodisch, R.; Honicke, D.; Wootsch, a. *J. Catal.* **2005**, *234* (1), 37–47.
(76) Wei, H.; Liu, X.; Wang, A.; Zhang, L.; Qiao, B.; Yang, X.; Huang, Y.; Miao, S.; Liu, J.; Zhang, T. *Nat. Commun.* **2014**, *5* (457), 5634.
(77) Shimizu, K.; Sawabe, K.; Satsuma, A. *Catal. Sci. Technol.* **2011**, *1* (3), 331.
(78) Hirunsit, P.; Shimizu, K.; Fukuda, R.; Namuangruk, S.; Morikawa, Y.; Ehara, M. *J. Phys. Chem. C* **2014**, *118* (110), 7996–8006.
(79) Verley, A. *Bull. Soc. Chi. Fr.* **1925**, *37*, 871–874.
(80) Ponndorf, W. *Angew. Chemie* **1926**, *39*, 138–143.
(81) Meerwein, H.; Schmidt, R. *Justus Liebigs Ann. Chem.* **1925**, *444*, 221–238.
(82) Wang, J.; Okumura, K.; Jaenicke, S.; Chuah, G.-K. *Appl. Catal. A Gen.* **2015**, *493*, 112–120.
(83) Cliffe, M. J.; Wan, W.; Zou, X.; Chater, P. a; Kleppe, A. K.; Tucker, M. G.; Wilhelm, H.; Funnell, N. P.; Coudert, F.-X.; Goodwin, A. L. *Nat. Commun.* **2014**, *5* (May), 4176.
(84) Vermoortele, F.; Bueken, B.; Le Bars, G.; Van de Voorde, B.; Vandichel, M.; Houthoofd, K.; Vimont, A.; Daturi, M.; Waroquier, M.; Van Speybroeck, V.; Kirschhock, C.; De Vos, D. E. *J. Am. Chem. Soc.* **2013**, *135*, 11465–11468.
(85) Creyghton, E. J.; Ganeshie, S. D.; Downing, R. S.; van Bekkum, H. *J. Mol. Catal. A Chem.* **1997**, *115*, 457–472.
(86) Liu, S. H.; Jaenicke, S.; Chuah, G. K. *J. Catal.* **2002**, *206* (2), 321–330.

CHAPTER 2

RESOLVING INTERPARTICLE HETEROGENEITIES IN COMPOSITION AND HYDROGENATION PERFORMANCE BETWEEN INDIVIDUAL SUPPORTED SILVER ON SILICA CATALYSTS

E. Plessers, I. Stassen, S. Pulinthanathu Sree, K. P. F. Janssen, H. Yuan, J. Martens, J. Hofkens, D. De Vos, M. B. J. Roeffaers. Adapted with permission from: *ACS Catalysis*, **2015**, *5*, 6690-6695 (pubs.acs.org/doi/10.1021/acscatal.5b02119).

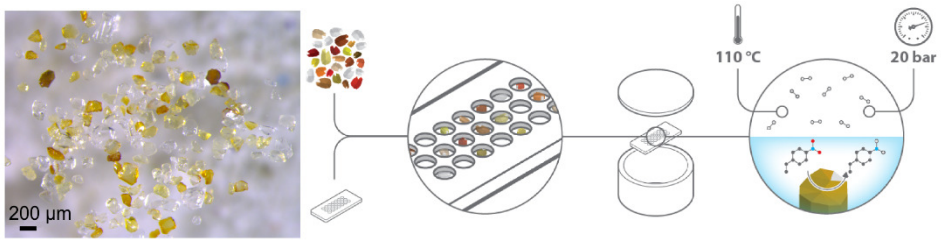

Abstract

Supported metal nanoparticle catalysts are commonly obtained through deposition of metal precursors onto the support using incipient wetness impregnation. Although typically homogeneous catalyst batches are assumed, here is shown how incipient wetness impregnation leads to 10-fold variations in silver loading between individual submillimetre-sized silica support granules. This heterogeneity has a profound impact on the catalytic performance, with 100-fold variations in hydrogenation performance between single catalyst granules. Optical microscopy is used to interlink single support particle level catalytic measurements to structural and compositional information, revealing the optimal silver loading.

Contributions and supporting information

The main part of the experimental work and article writing was performed by Eva Plessers. Ivo Stassen carried out the SEM microscopy, EDX analysis and nitrogen physisorption; Sree Pulinthanathu Sree measured high resolution SEM. Supporting information to Chapter 2 can be found in Appendix 1 on page 107.

CHAPTER 2 – RESOLVING INTERPARTICLE HETEROGENEITY

2.1 INTRODUCTION

Supported platinum group metal (PGM) nanoparticles are heavily used as hydrogenation catalysts; however, their price and future availability call for alternatives. Even though silver is mostly known as an oxidation catalyst, e.g. in the industrial production of ethylene oxide and methanol, various research groups have shown that supported silver nanoparticles can also chemoselectively catalyse the hydrogenation of unsaturated aldehydes, esters, and nitro-compounds;[1–5] for the last example silver offers the unique possibility to chemoselectively reduce functional nitroaromatics to the corresponding anilines, which is not possible with PGM nanoparticles.[6,7] The available information indicates that selective hydrogenation on supported silver catalysts is a structure sensitive reaction in which, in addition to the structure of the substrate, also nanoparticle size and support material play an important role.[1,2,8-10] In the selective hydrogenation of the unsaturated aldehydes crotonaldehyde and acrolein an increased reactivity and selectivity to the desired alcohol was found with increasing silver nanoparticle size.[1,9] This observation was related to the larger fraction of Ag (111) surfaces. In contrast, smaller silver nanoparticles (0.9 – 3 nm) were found to be superior in the selective hydrogenation of 4-nitrostyrene[11] and acrolein[12] in the high-pressure range. These observations can be rationalized by the rate-limiting dissociation of H_2 at coordinatively unsaturated silver sites and the adsorption geometry of the substrate. As often, these experimental results on the structure sensitivity of chemoselective hydrogenation with silver nanoparticles are seemingly contradictory, making clear-cut structure-activity assessments far from trivial. Supported metal catalysed reactions are inherently chemically complex and subtle changes in catalyst structure and properties can clearly have an important impact on the outcome.[13,14] Rationalization of bulk catalytic performances, even when supported by molecular simulations, often oversimplify the inherent complexity of the supported metal catalyst itself.[15] In addition to nanoparticle size and crystal facets also variations in loading, distribution and accessibility could play an important role in the overall catalytic performance. Essential when experimentally establishing correct structure-activity relationships is the generation of nanoparticles of well-controlled sizes. However, it is known that common catalyst synthesis strategies preclude variability

in nanoparticle size,[16-18] making validation of the nanoparticle size indispensable. In addition to bulk techniques such as X-ray diffraction, chemisorption, and EXAFS that generally yield average nanoparticle diameters within a supported catalyst,[9] direct imaging using transmission electron microscopy (TEM) allows precise determination of nanoparticle dimensions and dispersion.[19] As a result of the atomic resolution that can be achieved via TEM imaging, this approach is often the only suitable technique to study the size and dispersion of supported nanoparticles at the nanometre scale. Unfortunately, no direct link between these offline measurements and the catalytic performance can be made; thus, the catalytically active nanoparticles cannot be discriminated from spectator species.[20,21]

In this study we report that typical incipient wetness impregnation results in an unexpected 10-fold variation in silver loading between individual silica gel support granules, leading to inter support granule variations in number and size of the silver nanocatalysts. To validate the impact thereof on the catalytic performance, the selective reduction of 4-nitrostyrene to 4-vinylaniline was chosen. The aforementioned interparticle heterogeneity in silver loading leads to 100-fold variations in hydrogenation performance, and by using optical microscopy, it is possible to identify the optimal silver loading of the best performing supported metal catalyst granules.

2.2 EXPERIMENTAL SECTION

2.2.1 Catalyst preparation

An aqueous $AgNO_3$ solution (5.5 wt% Ag: 0.68 M $AgNO_3$), equalling the total pore volume of the support material based on physisorption (V_P = 0,79 cm^3/g), was added dropwise to dried silica gel (Sigma-Aldrich, Fluka 60752; pore ø = 6 nm, granule size 35 - 75 µm) at room temperature until a slurry formed. After equilibration at room temperature (0.5 h) the impregnated samples were dried overnight (16 h) in static air in an oven at 100 °C and finally calcined in static air at 500 °C for 2 h. Control samples were obtained by calcining commercially obtained $AgNO_3$ on silica gel (Sigma-Aldrich 248762; crystal size 75-300 µm) in air at 500 °C for 2 h, this catalyst is referred to as "commercial Ag/SiO_2".

2.2.2 Microscopy

2.2.2.1 Optical microscopy

Images were obtained via the eyepieces using an adapter from Micro-Tech-Lab (Austria) to connect a Canon EOS5D colour camera to an Olympus BX51 Upright microscope with a standard mercury lamp, equipped with infinity corrected air objectives 4x (0.16 N.A.) and 20x (0.40 N.A.). Colour sorting of individual supported

silver catalyst granules was performed on a stereomicroscope (Leica M165FC) by use of an eyelash manipulator.

2.2.2.2 Scanning electron microscopy

High Resolution-SEM images were obtained with a Nova NanoSEM 450 instrument (FEI), see supporting information. SEM-EDX was conducted using a FEI XL30FEG electron microscope equipped with an EDAX detector. Spectral analysis and quantification were performed with Genesis 4.61 software. Samples were mounted onto a copper TEM grid (300 mesh, Agar Scientific) fixed on a gold-coated cover slide which was then immobilized on to an aluminium stub using carbon sticker. These were imaged without any further sample modification.

2.2.3 Catalytic performance testing

2.2.3.1 Bulk level

Bulk hydrogenation reactions were performed in high pressure 15 mL TOP reactors and a 100 mL Parr reactor (2 h, 110 °C, 20 bar of H_2, 0.35 mol% of Ag, 70 mM 4-nitrostyrene in DMA, and 500 rpm unless stated otherwise). Analysis of the reaction products was carried out using a gas chromatograph (Shimadzu, CP-Sil 5, FID detector), and tetradecane was added as internal standard for quantitative GC analysis. Identification of the compounds was carried out using GC-MS (Agilent, HP-1, MS).

2.2.3.2 Single support particle level

Individual single granule hydrogenation reactions were performed by use of a multiwell placed in a 100 mL Parr reactor, enabling 21 reactions in parallel. Prior to the catalytic reaction, single support particles were carefully placed one by one in the different wells via an eyelash manipulator and a stereomicroscope (Leica M165FC). After this, the multiwell could be filled with the reaction solution using a micropipette and placed in the reactor. Since thermal hydrogenation of 4-nitrostyrene results in the formation of the unwanted 4-ethylnitrobenzene and little 4-vinylaniline, in each run several wells were not filled with a catalyst particle to account for this blank conversion and some wells were only filled with solvent to ensure that no cross contamination had occurred. To lower solvent evaporation as much as possible the high boiling *N,N*-dimethylacetamide (DMA) was used as a solvent and n-hexadecane as internal standard for quantitative GC-analysis. Optimization of reaction conditions led to the use of 18 µL of a 33 mM 4-NSt solution in each microwell, with hydrogenation performed under 20 bar H_2 on heating to 110 °C for 2.5 h in a Parr reactor filled with 3 mL of DMA. Analysis of the reaction products was carried out using a gas chromatograph (Shimadzu, CP-Sil 5, FID detector) after rinsing the wells two times with pure DMA (20 µL).

2.3 RESULTS AND DISCUSSION

2.3.1 Compositional heterogeneities at the micro- and nanoscale

Supported silver catalysts (5-6 wt% Ag) on silica gel were synthesized via standard incipient wetness impregnation.[4,17] During calcination of the white silver nitrate impregnated silica powder, silver oxide was formed and subsequently at temperatures above 400 °C completely decomposed into metallic silver.[22,23] The resulting silica supported silver nanoparticle catalyst powder has a typical yellowish appearance and looks seemingly homogeneous. However close inspection using optical microscopy revealed an unexpected variability in colour between different support granules (Figure 1A-C); to our knowledge this interparticle colour heterogeneity has not been reported so far for supported metal catalysts. An even more pronounced interparticle colour heterogeneity, ranging from transparent to yellow to red-brown, was observed in a supported silver catalyst (6 wt% Ag) made by calcining $AgNO_3$ on silica gel obtained from Sigma-Aldrich, further referred to as "commercial Ag/SiO_2" (Figure 1D-F). Strikingly, within one large support granule of about 100 µm in diameter no significant colour variation was observed.

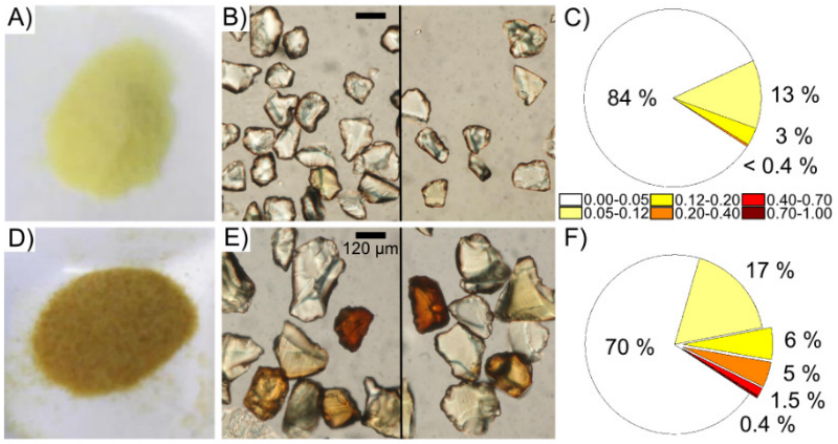

Figure 1 Interparticle heterogeneity in Ag/SiO_2 at the support granule level revealed by optical microscopy: **A–C)** silver on silica gel obtained via typical incipient wetness impregnation; **D–F)** commercial $AgNO_3$ on silica gel after calcination on the macroscale (A, D) and microscale (B, E). **C, F)** Interparticle heterogeneity (n = 250) illustrated with pie diagrams. Colours represent the red colour index of individual Ag/SiO_2 granules (for determination see the text in the Supporting Information and Figure S1).

Since pure silica powder is optically transparent, also after a similar heat treatment, the observed colour formation must be associated with the silver nanoparticles. It is well-known that the optical appearance of silver nanoparticles is related to the

surface plasmon resonance. Next to nanoparticle shape and refractive index of the environment, plasmon absorbance and hence selective (visible) light absorption is largely determined by the nanoparticle size.[24] For silver nanoparticles in silica below about 10 nm diameter the surface plasmon resonance peaks at around 420 nm, resulting in a yellow appearance upon white light illumination. Increasing the size to around 100 nm, diameter results in a strong red-shift of about 100 nm which causes red coloration.[25] Nitrogen physisorption measurements of the used silica gel provide a BJH desorption average pore width of 60 Å (Figure S2 in the supporting information). Although the rather broad pore size distribution would give rise to polydisperse silver nanoparticles formed inside the support pores, their size is restricted to below 10 nm resulting in an overall yellowish appearance. The presence of larger, unconfined silver nanoparticles at the outer surface of the support granules could give rise to colour variations. However, several other factors will influence the optical appearance such as the local nanoparticle concentration and the absolute support granule size, which is directly linked to the optical path length and hence the resulting light absorption.[25] Since no relation was found between optical appearance and the absolute support granule size, the latter can be excluded and the colour heterogeneity between individual silica granules must be sought at the level of the supported silver nanoparticles.

In order to investigate the colour heterogeneity at the silver nanoparticle level, we resorted to high-resolution scanning electron microscopy (HR-SEM) correlated with optical microscopy. First, the optical appearance of the silica supported silver catalyst was examined via optical microscopy after deposition of the granules on a cover slip with a marked copper grid. Then, HR-SEM was performed to probe the outer surface of the same support granules of which the optical colour is known. Marks on the copper grid and the irregular shape of the support granules make the correlation of the optical images and SEM micrographs highly reliable (Figure 2A,B). By specifically probing of the outer surface of transparent, yellow and red granules, three distinct silver nanoparticle size ranges were noticed: 1-10, 20-50 and > 400 nm (Figure S3 in the supporting information). The relative contribution of the larger 20-50 nm nanoparticles increases with increasing coloration, and the extremely large silver crystals (> 400 nm) were only visible on the dark red coloured silica granules (Figure 2C and Figure S3E). These electron micrographs thus evidence that there is a clear relation between colour targeted via optical imaging and silver nanoparticle size at the outer surface of the support granules.

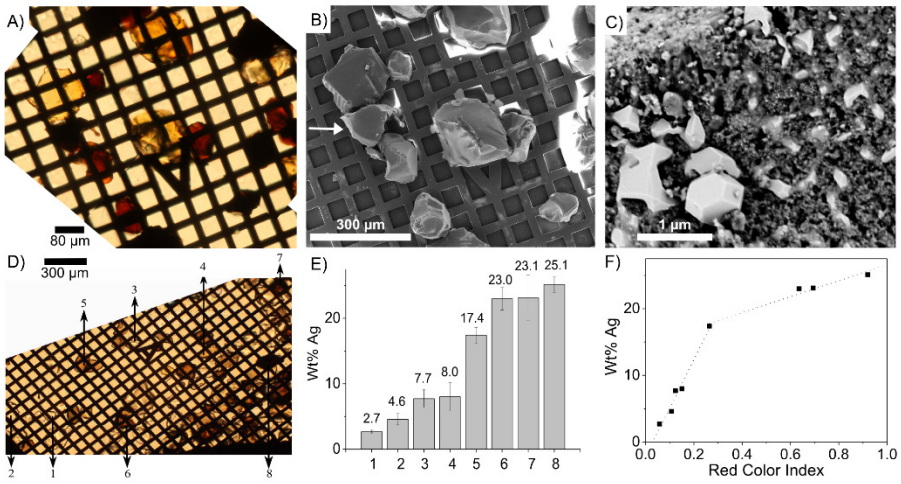

Figure 2 Correlation of the optical appearance of single Ag/SiO_2 granules to silver nanoparticle size (A–C) and silver loading (D–F). **A)** Optical micrograph of single Ag/SiO_2 granules. **B)** HR-SEM micrograph showing the overview of the same area. **C)** HR-SEM micrograph of a dark support granule showing small nanoparticles (<10 nm, centre) and very large silver nanoparticles (700–1000 nm, left lower corner). **D)** Optical micrograph of single Ag/SiO_2 granules. **E)** Silver loading of the numbered single Ag/SiO_2 granules measured via energy dispersive X-ray analysis. **F)** Link between red colour index of individual Ag/SiO_2 granules and their silver loading. The results shown here were obtained from the commercial 6 wt% Ag/SiO_2 catalyst.

However, these findings do not exclude the possibility that the optical heterogeneity can also be induced by a difference in silver nanoparticle concentration, analogous to the observed heterogeneity in Pt/zeolite Y catalysts.[19] Therefore, we adopted energy dispersive X-ray (EDX) spectroscopy to probe the silver content of individual silica support granules, again directly correlated to the optical appearance of the exact same granules (Figure 2D). Figure 2E shows that typical supported silver catalysts, obtained from commercial sources or via standard impregnation methods, display at least a 10-fold variation in silver loading between different silica support granules. Comparison of the EDX-results and colour indexing of the optical images led to a clear trend between optical appearance and silver content (Figure 2F). Since the silver content determined via SEM-EDX is limited to the first few micrometres below the outer surface, this approach could lead to a misinterpretation of the total silver loading of this support granule because a silver gradient might exist along the cross-section of the support granule.[26] To further validate the SEM-EDX measurements, focused ion beam (FIB) milling was used to section a yellow granule in the middle. A clear silver gradient can be observed with silver concentrations decreasing from the outer surface of the granule toward the centre; even in the centre significant silver amounts could still be detected (Figure S4 in the Supporting

Information). Furthermore, on these FIB sections no large silver nanoparticles were observed in the interior of the support granules with high resolution SEM.

These correlated microscopy data link the optical appearance of a support granule to both silver concentration and size of non-pore confined silver nanoparticles at the outer surface. The increasing coloration observed in optical microscopy is related to both variations in silver loading and the presence of larger silver nanoparticles at the outer surface of the support granules. These calibration data can now be used to quantify the amount of silver in every support granule by simply using optical images. Optical microscopy is easily accessible without lengthy sample preparation and allows rapid determination of interparticle heterogeneity on the support granule level. Metal loading quantifications based on optical images rely on correlations with other analytical methods such as EDX, HR-SEM, etc.

2.3.2 **Linking hydrogenation performance to catalyst composition via catalytic measurements at the single support particle level**

Because of the large variability in silver loading and nanoparticle size it is not straightforward to unequivocally link performance to catalyst properties, certainly not from typical ensemble averaged measurements using at least milligrams of powdered catalyst. In this study we measured for the first time the catalytic performance at the level of the individual silica support granule. In order to minimize variations in experimental conditions, multiwell plates were used enabling 21 reactions in parallel in the same high pressure Parr reactor; the multiwell catalytic measurements at the single support particle are shown schematically in Figure 3.

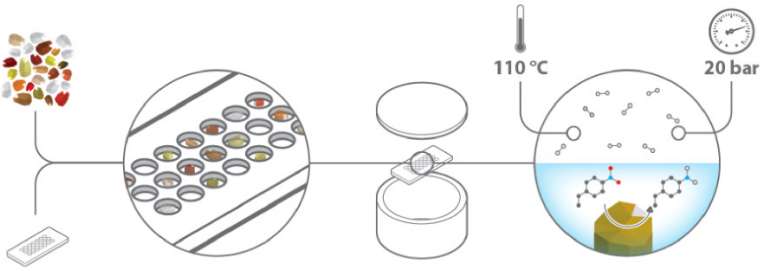

Figure 3 Schematic representation of a multiwell catalytic measurement at the single support particle level. In a typical run around 13 catalyst granules were tested together with four blank tests and two wells were only filled with solvent (18 μL of a 33 mM 4-nitrostyrene solution in each microwell, 20 bar of H_2, 110 °C, 2.5 h, 100 mL Parr reactor filled with 3 mL of DMA).

These multiwell plates also allow recording of optical transmission images of the individual supported catalyst granules placed in each reaction well; from these optical images the exact silver content in every microwell is determined, which is

critical for normalizing catalyst performance. Subsequently, after 590 nmol of 4-nitrostryrene (4-NSt) in 18 µL of *N,N*-dimethylacetamide (DMA) solvent was loaded, the multiwell plate was loaded in the Parr hydrogenation reactor at 20 bar of H_2 and heated to 110 °C; under these conditions no distillation of the reactant or its products was observed. After 2.5 h the reaction mixture of every microwell was analysed via gas chromatography. Figure 4A shows the normalized catalytic performance of 47 individual supported catalyst granules as a function of their total silver loading (more details are given in the Supporting Information, and Figures S5 - S6).

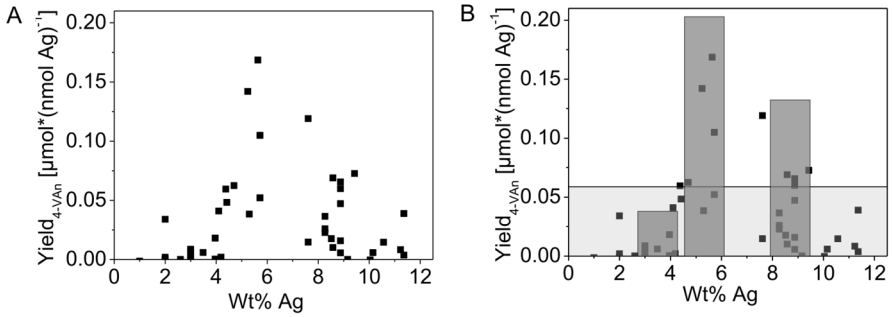

Figure 4 A) Single-granule catalytic hydrogenation of 4-nitrostyrene with commercial Ag/SiO_2 catalyst: results of 47 individual silver supported silica granules. Estimation of silver loading was based on red colour index and SEM-EDX, complemented by ICP-AES measurements of colour-sorted granules. More details can be found in the text and Figure S6 of the Supporting Information. **B)** Bulk hydrogenation reactions with colour-sorted commercial Ag/SiO_2 samples (column bars), displaying up to a 2.5-fold increase of yield with respect to unsorted commercial catalyst (filled area) (110 ℃, 20 bar of H_2, 2.5 h). 4-VAn = 4-vinylaniline.

These single support particle data undoubtedly reveal an optimal silver loading. Granules with about 6 wt% of silver show up to 100-fold higher normalized 4-vinylaniline yield than catalyst granules from the same batch containing < 4 wt% or > 8 wt% of silver. From the detailed physicochemical characterization (vide supra) the highest hydrogenation performance can be attributed to support granules with yellow appearance (red colour index 0.12-0.20) i.e. 5-7 wt% silver. These yellow coloured granules contain besides the 6 nm pore confined silver nanoparticles also a reasonable amount of larger, 20-50 nm sized, silver nanoparticles on the support granule's surface. When considering a whole support granule the pore confined silver nanoparticles represent over 99.9 % of the total number of nanoparticles. Silver in these yellow coloured support granules is up to 100 times less efficiently used as well in highly loaded (> 8 wt% Ag) support granules, with silver nanoparticles larger than 400 nm on the support's outer surface, as in transparent support granules with silver loadings below 4 wt% which only contain the pore confined 6

nm silver nanoparticles. Hence it can be concluded that in this sample support granules with 6 wt% silver and the highest relative contribution of 20-50 nm sized silver nanoparticles are the most active in the selective 4-nitrostyrene reduction contradicting earlier reports based on ensemble-averaged hydrogenation data.[11]

2.3.3 **Rationally improving the hydrogenation performance of supported silver catalysts**

In order to validate these single support particle results, namely that the catalyst granule's optical appearance is linked to the silver content and its catalytic performance, we carried out bulk catalytic hydrogenation reactions. Ag/SiO_2 samples with four different silver contents ranging from 4 to 19 wt% at the bulk level were synthesized. As expected, all of these materials showed a significant interparticle heterogeneity in optical appearance (Figure S7 in the supporting information). Using the average performance determined for every colour of catalyst granule via single support particle experiments, the estimated theoretical 4-vinylaniline yield of each of these catalyst samples was estimated (Figure 5: the calculation is explained in the Supporting Information). These calculations predict that the sample with a bulk loading of 13 wt% in silver should show the best selective hydrogenation performance. Indeed, in a typical hydrogenation reaction with 0.35 mol% silver and with the same relative amounts of substrate and solvent as were used in the multiwell experiments, a similar performance trend was observed (Figure 5). In addition, the results of the commercial Ag/SiO_2 sample (6 wt%) fit perfectly within the results of the self-synthesized samples. The outcome of the single support particle experiments can thus undoubtedly be extrapolated to the bulk level. Although the normalized yield of the commercial sample increased by 38 % upon increasing the overall silver loading to 13 wt%, a considerably higher improvement must be possible on the basis of the observed heterogeneity. Ideally one would rationally synthesize a batch which consists of only yellow supported silver catalyst granules; however, none of the typical impregnation approaches gave a satisfactory result. In an attempt to obtain a more homogeneous catalyst sample, the commercial silver on silica catalyst was manually sorted into three different fractions (Figure S8). As can be expected from the single support particle experiments, the batch with yellow support granules outperforms the batches with transparent or orange and red granules to the same degree as could be expected from the single support particle studies (Figure 4B).

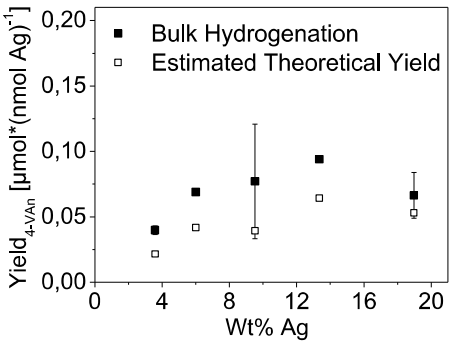

Figure 5 Bulk hydrogenation reactions of 4-nitrostyrene with self-synthesised (4 to 10, 13, and 19 wt % Ag) and commercial 6 wt % Ag/SiO_2 catalysts (■), and estimated theoretical yield based on optical appearance (□) (for the determination see the Supporting Information, silver loading based on ICP-AES) (110 °C, 20 bar of H_2, 2 h).

2.4 CONCLUSIONS

We have shown that typical incipient wetness impregnation brings about severe heterogeneity in metal loading at the support particle level. Specifically, 10-fold variations in silver metal loading between individual silica support granules are no exception within one catalyst batch. These differences in metal loading severely impact the catalytic performance on measurement at the same scale. Here optical microscopy proved to be a convenient tool to directly interlink the physicochemical properties and hydrogenation performance of individual support particles. Following this approach, we could resolve 100-fold variations in normalized catalytic performance for the selective 4-nitrostyrene reduction and determine the optimal silver loading for this reaction. More specifically, these single particle experiments indicate that support granules which have the relative highest contribution of silver nanoparticles of about 20–50 nm show the highest 4-vinylaniline (4-VAn) yield. Following traditional catalyst impregnation optimization based on ensemble averaged characterization and catalytic performance measurements it would be far from trivial to find this optimal catalyst composition. The proposed optical screening method is widely applicable to supported metal catalysts: e.g., similar heterogeneity in colour and thus loading were also observed in Pt/SiO_2 (Figure S9 in the supporting information).

2.5 REFERENCES

(1) Wei, H.; Gomez, C.; Liu, J.; Guo, N.; Wu, T.; Lobo, R.; Christopher, L.; Lobo-Lapidus, R.; Marshall, C. L.; Miller, J. T.; Meyer, R. J. *J. Catal.* **2013**, *298*, 18.
(2) Shimizu, K.; Sawabe, K.; Satsuma, A. *Catal. Sci. Technol.* **2011**, *1*, 331.
(3) Yin, A.; Guo, X.; Dai, W.; Fan, K. *Chem. Commun.* **2010**, *46*, 4348.
(4) Steffan, M.; Jakob, a; Claus, P.; Lang, H. *Catal. Commun.* **2009**, *10*, 437.
(5) Chen, Y.; Wang, C.; Liu, H.; Bao, X.; Qiu, J. *Chem. Commun.* **2005**, *2*, 5298.
(6) Corma, A.; Serna, P. *Science* **2006**, *313*, 332.
(7) Furukawa, S.; Yoshida, Y.; Komatsu, T. *ACS Catal.* **2014**, *4*, 1441.
(8) Corain, B.; Schmid, G.; Toshima, N. *Metal Nanoclusters in Catalysis and Materials Science: The Issue of Size Control;* Elsevier: Amsterdam, 2007; Chapter 8.
(9) Claus, P.; Hofmeister, H. *J. Phys. Chem. B* **1999**, *103*, 2766.
(10) Hirunsit, P.; Shimizu, K.; Fukuda, R.; Namuangruk, S.; Morikawa, Y.; Ehara, M. *J. Phys. Chem. C* **2014**, *118*, 7996.
(11) Shimizu, K.; Miyamoto, Y.; Satsuma, A. *J. Catal.* **2010**, *270*, 86.
(12) Bron, M.; Teschner, D.; Knopgericke, a; Steinhauer, B.; Scheybal, A.; Havecker, M.; Wang, D.; Fodisch, R.; Honicke, D.; Wootsch, A. *J. Catal.* **2005**, *234*, 37.
(13) de Jong, K. P. *Synthesis of Solid Catalysts*; Wiley-VCH: Weinheim, Germany, **2009**; Chapters 1-5.
(14) Morbidelli, M.; Gavriilidis, A.; Varma, A. *Catalyst Design: Optimal Distribution of Catalyst in Pellets, Reactors, and Membranes*; Cambridge University Press, 2001; Chapter 7.
(15) Gao, F.; Goodman, D. W. *Ann. Rev. Phys. Chem.* **2012**, 63, 265.
(16) Ertl, G.; Knözinger, H.; Schüth, F.; Weitkamp, J. *Handbook of heterogeneous catalysis*; Wiley-VCH: Weinheim, Germany, 2008; Chapter 2.
(17) White, R. J.; Luque, R.; Budarin, V. L.; Clark, J. H.; Macquarrie, D. J. *Chem. Soc. Rev.* **2009**, *38*, 481.
(18) Prieto, G.; Zečević, J.; Friedrich, H.; de Jong, K. P.; de Jongh, P. E. *Nat. Mater.* **2012**, *12*, 34.
(19) Zečević, J.; van der Eerden, A. M. J.; Friedrich, H.; de Jongh, P. E.; de Jong, K. P. *ACS Nano* **2013**, *7*, 3698.
(20) Sambur, J. B.; Chen, P. *Annu. Rev. Phys. Chem.* **2014**, *65*, 395.
(21) Niemantsverdriet, J. W. *Spectroscopy in Catalysis*; Wiley-VCH: Weinheim, Germany, 2007; p 325.
(22) Waterhouse, G. I. N.; Bowmaker, G. a.; Metson, J. B. *Phys. Chem. Chem. Phys.* **2001**, *3*, 3838.
(23) Weaver, J. F.; Hoflund, G. B. *J. Phys. Chem.* **1994**, *98*, 8519.
(24) Sun, Y.; Xia, Y. *Analyst* **2003**, *128*, 686.
(25) Quinten, M. *Appl. Phys. B: Lasers Opt.* **2001**, *73*, 317.
(26) Espinosa-Alonso, L.; Beale, A. M.; Weckhuysen, B. M. *Acc. Chem. Res.* **2010**, *43*, 1279.

CHAPTER 3

OPTICAL MICROSCOPY REVEALS THE ORIGIN OF HETEROGENEITY AT THE SUPPORT GRANULE SCALE OF SILVER ON SILICA CATALYSTS

E. Plessers, J. E. van den Reijen, P. E. de Jongh, K. P. de Jong, M. B. J. Roeffaers.
Submitted.

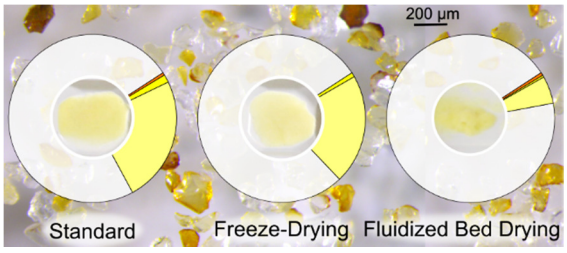

Abstract

As shown in Chapter 2, traditional incipient wetness impregnation may induce severe interparticle heterogeneity between catalyst granules of the same silver on silica batch. However, the origin of this heterogeneity is still unclear. Here we show that every elementary step in the synthesis procedure has an effect on the resulting interparticle heterogeneity, but the influence of the drying step is the most important. Specifically, it is shown that the position of a granule in the stagnant drying bed has a large influence on the resulting colour and thus silver distribution. This is further demonstrated by varying the drying conditions: fluidized bed drying in contrast to static drying leads to a more homogeneous silver loading of the granules.

Contributions and supporting information

The main part of the experimental work and article writing was performed by Eva Plessers. Fluidized bed synthesis experiments were carried out in collaboration with J. van den Reijen from Utrecht University under the supervision of prof. K. P. de Jong and prof. P. E. de Jongh. Supporting information to Chapter 3 can be found in Appendix 2 on page 118.

CHAPTER 3 – ORIGIN HETEROGENEITY

3.1 INTRODUCTION

Supported metal nanoparticles are widespread in heterogeneous catalysis since they combine both high activity and stability. These metal nanoparticle catalysts are commonly synthesized via a procedure that is often designated as incipient wetness impregnation (IWI). In IWI a porous support is filled with a metal precursor solution that equals the pore volume of the support, therefore also called pore volume impregnation or dry impregnation.[1,2] By subsequent evaporation of the solvent, the precursor solution becomes supersaturated inducing precipitation and crystallization onto the support. Drying proceeds until the solvent is completely removed and finally conversion of the precipitated precursor to the supported metal nanoparticle catalyst is executed via decomposition of the precursor, so-called calcination at elevated temperatures.[2–4] The simplicity of this synthesis procedure, that also minimizes waste, makes impregnation a widespread technique at the laboratory and industrial scale. Furthermore, for precious metals impregnation ensures that all the metal added as precursor ends up in the final catalyst. Alternatively when aiming for high metal loadings or working with sparsely soluble or thermally instable precursors wet impregnation, employing an excess of water, may be used.[4] Other frequently used approaches to deposit metals onto a support are co-precipitation, deposition-precipitation and chemical vapour deposition.[1,3,4]

It is generally accepted that the catalytic performance of supported metal nanoparticles is mainly related to the nanoparticle size and distribution inside the support.[3] This forced the field to employ various characterization techniques. The most frequently used characterization methods, such as X-ray diffraction and transmission electron microscopy, often assume homogeneous catalyst batches. For example the average crystallite size can be estimated by modelling the experimentally obtained peak width of the Bragg reflection in X-ray diffraction (XRD) using the Scherrer equation.[5] Other bulk techniques to estimate nanoparticle size are chemisorption, EXAFS and specifically for silver nanoparticles UV/Visible-Diffuse Reflectance Spectroscopy.[6–11] The obtained nanoparticle size from all of these bulk techniques is an averaged value for all nanoparticles present in the powder, revealing no information about nanoparticle distribution and/or dispersion within a single and between different support particles. Zooming in on the nanoparticles using transmission electron microscopy (TEM) on the contrary, allows precise determination of individual supported nanoparticle dimensions and distribution

given that a representative sample of the powder has been investigated.[12–14] Next to size and spatial distribution, metal loading is another important parameter in supported metal nanoparticle catalysts. This value can also routinely be determined as bulk averaged value via inductive coupled plasma (ICP) spectroscopy techniques after complete decomposition of the sample or on a microscopic scale via energy dispersive X-ray scattering (EDX) or using advanced electron tomography.[13] As mentioned above, both bulk averaging techniques and spatially resolving measurements assume homogeneous batches.

On the contrary, studies on metal nanoparticle catalysts loaded onto millimetre sized support bodies have shown non-uniform intraparticle metal loadings such as 'egg-shell', 'egg-yolk' or 'egg-white' to be more generally obtained than a 'uniform' homogeneous distribution.[1,4,15] Based on literature reports and model calculations Morbidelli, Gavriilidis and Varma[15] conclude that several experimental factors e.g. precursor solution concentration, pH, ionic strength and temperature as well as drying conditions cause this heterogeneity during supported metal synthesis. Visual examination of the Ni distribution in Al_2O_3 monoliths reveals that static drying results in an egg-shell profile while freeze-drying and microwave drying result in an uniform distribution.[16] The same conclusion was obtained by Liu and co-workers,[17] who found a more uniform distribution of Ni/Alumina after microwave drying and further determined that an egg-shell profile was observed for low metal loadings while metal distribution was uniform at high initial metal precursor concentrations.

Also for micrometre-sized granules, typically used for catalysts discovery at the laboratory scale, intraparticle variations in nanoparticle size, dispersion and distribution have been shown. Electron tomography for example revealed that typical impregnation and drying results in a non-uniform metal distribution and nanoparticle size whereas optimization of drying and calcination resulted in more homogeneous loading.[12,18–20] Studies on interparticle heterogeneities at the support granule level however have to the best of our knowledge only been reported twice: (1) advanced electron tomography on platinum loaded sub-micron USY zeolites[13] (2) a correlative approach using optical microscopy on silver loaded mesoporous silica granules.[21] In both cases at least 10-fold variations in metal loading between different support particles were found.[13,21] Furthermore, these differences in metal loading severely affect the catalytic performance of individual catalyst granules.[21] In contrast to millimetre-sized support bodies, where transport of the metal precursor via the impregnation solution during drying is responsible for the heterogeneous metal loading, the origin of the heterogeneity during the preparation of supported nanoparticles at micrometre-sized granules is still unclear. In this work, optical microscopy was used to study the influence of the different elementary steps on the loading heterogeneity during the preparation of supported silver on silica using

typical impregnation procedures and a silver nitrate precursor solution that displays limited chemical or electrostatic interactions with the support. Variations in silver loading were assessed via the coloration of individual support granules within the resulting powder. From the conducted experiments it can be concluded that each of the elementary steps namely impregnation, drying, calcination and activation induces interparticle heterogeneity at the granule level. For this particular support and metal (precursor) system the drying step brings about most of the heterogeneity. Specifically, from this work it is proven that fluidized bed drying results in the most homogeneously loaded silver on silica.

3.2 EXPERIMENTAL SECTION

3.2.1 **Catalyst preparation**

5 wt% Ag/SiO_2 was synthesized via standard incipient wetness impregnation. To 950 mg of dried silica gel (Aldrich 60752; pore ø = 6 nm, granule size 35 - 75 µm, V_P= 0,79 cm^3/g – N_2 physisorption) an aqueous solution of $AgNO_3$ (78 mg $AgNO_3$, 750 µL dist. water) was added dropwise under vigorous stirring with a spatula at room temperature (RT) until a slurry formed. After equilibration at RT (0.5 h), the silver impregnated silica was dried in static air at 100 °C (16 h) and calcined in static air (1-5 °C/min 500 °C, 2 h).

Modifications to the synthesis procedure: (1) NaOH pre-treatment: 0.1 M NaOH aqueous solution (5 mL/g silica), 2 h stirred, supernatant removed via centrifugation (1000 rpm), washed with dist. H_2O (7 times, 1000 rpm), dried (80 °C) and calcined; (2) wet impregnation**:** 1.5 mL dist. H_2O added to silica gel before impregnation, equilibrated 1 h at RT; (3) vacuum drying**:** RT, 16 h, 10 mbar; (4) freeze drying**:** frozen at -20 °C (4 h) and liquid N_2 cooled (1 h); freeze drying 4 h 0.3 mbar; (5) fluidized bed drying: 200 mg impregnated powder is transferred to a tubular quartz reactor (Ø 1 cm), 2 quartz wool plugs were used to create a homogeneous flow through the bed and to prevent the powder being blown out, a controlled flow of 30 mL/min 80% N_2 20% O_2 was used, oven was heated to 100 °C (10 °C/min) for 8 h; (6) fluidized bed calcination**:** 200 mg dry powder, tubular quartz reactor, 30 mL/min 80% N_2 20% O_2, 1 °C/min 500 °C, 2 h.

3.2.2 **Characterisation**

Optical microscopic images were obtained via the eyepieces using an adapter from Micro-Tech-Lab (Austria) to connect a Canon EOS5D colour camera to an Olympus BX51 Upright microscope with a standard mercury lamp, equipped with infinity corrected air objectives 4x (0.16 N.A.) and 20x (0.40 N.A.). Overview images of the powder bed were obtained with a Leica (M165FC) stereomicroscope. Colour indexing is described in detail in ref. 21. Images were adjusted to obtain optimal contrast and brightness (ImageJ). The mean 8-bit value in the blue channel was used to increase the sensitivity towards transparent, light yellow and yellow coloured granules.

Nitrogen adsorption and desorption isotherms were measured using a Micromeritics 3Flex 3500 physisorption instrument at 77 K. The sample was degassed before measurement at 423 K for 6 h under vacuum (10^{-2} mbar). The pore size distribution was calculated using the BJH method (Harkins and Jura thickness curve and Faas correction, 3Flex 3.00 software).

3.3 RESULTS

First, 5 wt% silver supported on a silica gel (Sigma-Aldrich, Fluka 60752) with 409 m^2/g BET specific surface area and 6 nm pore diameter was prepared via standard incipient wetness impregnation (IWI) using a 0.62 M silver nitrate solution.[1,3,4] After calcination, the resulting silica supported silver nanoparticles powder has a typical yellowish and homogeneous appearance. However, as reported before, optical microscopy revealed an unexpected colour variability with support granules ranging from transparent over yellow to red. The colour at the support granule level is associated to the silver nanoparticles, more specifically to the surface plasmon resonance. The plasmon absorbance is largely determined by the nanoparticle size, next to nanoparticle shape and refractive index of the environment.[22] Increasing the silver nanoparticle diameter inside a silica matrix from below 10 to about 100 nm results in a red-shift of the surface plasmon resonance absorbance peak from 420 nm to about 520 nm. This red-shift results in a changing coloration from weak yellow to intense red.[6] However, not only size, but also silver nanoparticle concentration will influence the overall optical appearance of the support granule. As evidenced before, via correlation of optical microscopy with high resolution SEM and EDX, the coloration in our silver on silica sample is related to both the nanoparticle loading and size.[21] Transparent granules contain a low concentration of pore confined 6 nm silver nanoparticles, whereas an increased coloration was associated to an elevated silver concentration and the formation of large silver nanoparticles on the outer surface of the granules.

To further examine the origin of this interparticle heterogeneity for silver loading at the granule level, the incipient wetness impregnation procedure was divided into its 3 main steps: impregnation, drying and calcination (and if necessary activation) (Figure 1).

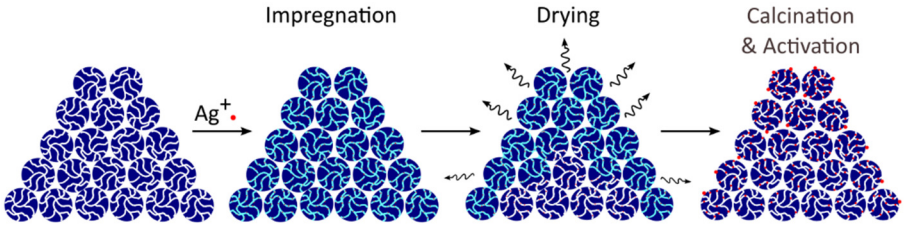

Figure 1 Schematic representation of incipient wetness impregnation (IWI) without strong precursor-support interaction.

In the impregnation step a dried, empty porous support is filled with a metal precursor solution that equals the pore volume of the support, assuring complete filling of the pores and an even distribution of the (silver nitrate) precursor over the

granules. By subsequent evaporation of the solvent in the drying step, the precursor solution becomes supersaturated inducing precipitation and crystallization onto the support. Drying proceeds until the solvent is completely removed and finally conversion of the precipitated precursor to the supported metal (silver) nanoparticle catalyst is executed via decomposition of the precursor, so-called calcination at elevated temperatures. The influence of each of these steps on the resulting interparticle heterogeneity, was assessed based on the colour heterogeneity of the powder obtained after the last calcination and activation step. But before focusing on the impregnation procedure, interparticle heterogeneities present in the support were examined.

3.3.1 **Heterogeneity at the support granule level**

It is generally known that the adsorption strength of the metal precursor onto the support plays an important role during the impregnation.[4,15,23] For this particular system, silver cations show a weak adsorption onto the silica support surface because of the limited surface charge density at the prevailing pH.[15,24] Silica immersed in neutral water acquires some negative surface charges of about -0,02 C/m^2,[25] predominantly through the deprotonation of terminal silanol groups.[26] For 1 gram of silica gel with a BET specific surface area of 409 m^2/g (Figure S1), this corresponds to 85 µmol negatively charged O-atoms on the surface. To prepare a 5 wt% silver on silica material, a solution with 460 µmol ionic silver is used, so less than 20% of the silver can be electrostatically adsorbed on the silica surface. The surface charge density of the support granules was probed via the ion exchange of a cationic dye Rhodamine 6G. Based on the literature reported silica surface charge density,[25] the silica gel powder was contacted with an aqueous Rhodamine 6G solution containing sufficient cationic dye to compensate all surface charges (see supporting information, Figure S2). Using confocal microscopy with a 405 nm laser, it can be concluded that there is a 5-fold interparticle heterogeneity in Rhodamine concentration. Since this interparticle heterogeneity in Rhodamine concentration can be used as a measure for the surface charge heterogeneity, this could partially explain the observed 10-fold heterogeneity in silver loading between different silica support granules,[21] although as mentioned above only less than 20 % of the used silver ions at this loading of 5 wt% can be electrostatically adsorbed on the silica surface. In an attempt to homogenize this surface charge and to further enhance the interaction between the silver cations and the silica surface, the silica gel was pre-treated with an aqueous 0.1 M NaOH solution followed by extensive washing with distilled water before impregnation (see supporting information). When using this pre-activated silica support in the regular IWI procedure, the bulk powder showed a reduced yellow coloration (Figure 2). Zooming in via optical microscopy confirms that the support particles show a reduced coloration compared to the original sample,

hence increasing and homogenization of the surface charges deceases heterogeneity. Unfortunately, the base pre-treatment results in silica dissolution and fragmentation making a detailed comparison at the single support particle level difficult.

Besides intrinsic heterogeneities in surface charge density, metal impurities (Na, Al, Ti, ...) present in the silica gel before impregnation also severely influence the resulting surface charge. As silica gel is typically made starting from less pure water glass solutions,[2] the IWI procedure was repeated using a self-synthesized silica gel made from tetraethyl orthosilicate (TEOS) and a commercially obtained ultra-pure silica (CARiACT) (see supporting information and Figure S1). The thus obtained powders showed an even larger coloration (Figure 2), which cannot be explained by the presence of impurities in the silica gel, but more likely is the result of differences in silver nanoparticle sizes and loadings per granule since the same powder averaged silver loadings are used. These different silica materials all have a completely different surface area, pore size and possibly different surface chemistry that influence the resulting silver nanoparticle size and distribution. Further impregnation studies described in this work were therefore always executed with the commercially obtained silica gel (from Sigma-Aldrich) with a pore diameter of 6 nm and granule size ranging between 35 - 75 µm.

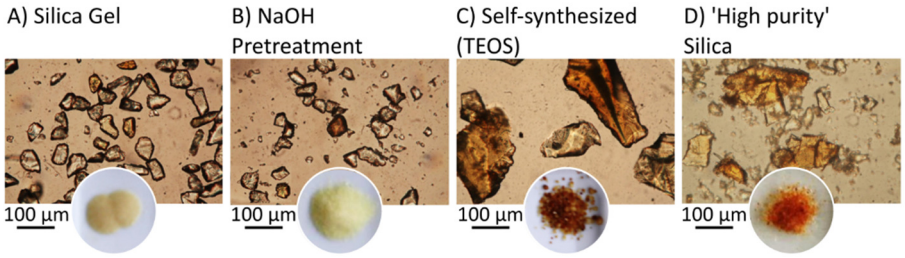

Figure 2 Silver incipient wetness impregnation on various silica supports: **A)** standard silica gel (Aldrich), **B)** NaOH pre-activated silica gel, **C)** tetraethyl orthosilicate (TEOS) based self-synthesized silica gel and **D)** high purity silica (CARiACT) (5-6 wt% Ag, vacuum drying at RT 16 h, calcination 16 h 500 °C).

3.3.2 Heterogeneity induced during impregnation

Since variation in surface charge at the granule level can partially explain the observed heterogeneity in silver loading, a co-impregnant can be introduced in the impregnation solution to compete with the cationic silver for the negatively charged adsorption sites. This strategy is for example often used for platinum impregnation of Al_2O_3 pellets.[2,15] The effect of co-impregnation with an excess of ammonium nitrate was investigated. Additionally, also the effect of adding an excess of solvent,

with the same total amount of silver precursor, was investigated. Both procedures however did not lead to complete homogeneity (see supporting information, Figure S3).

An important question when performing the conventional incipient wetness impregnation procedure is if all pores are effectively filled with the precursor solution. A positive indication of the latter, often used in the laboratory, is the transition of a seemingly 'dry' powder to a moist state when adding the last drop of the precursor solution.[3] Besides macroscopic observation of pore filling, differential scanning calorimetry (DSC) also confirmed that upon impregnation of silica gel with an aqueous $Ni(NO_3)_2$ solution, 97 % of the pore volume is filled.[27] Cryo-electron tomography further evidenced that pore filling of SBA-15 with $Co(NO_3)_2$ was homogeneous after impregnation.[19] Since the correct determination of the support mesopore volume is an important parameter to reach this situation, nitrogen physisorption was performed on the silica gel supports under study (see supporting information). Using 100 % of the N_2-physisorption determined pore volume precludes that up until adding the last drop of the precursor solution, capillary forces drive the uptake of the solution into the support. However, careful execution and observation of the impregnation step indicated that vigorous stirring while adding the precursor solution is very important to maintain the 'dry' powder state until the very last drop. Although impregnation in vacuum conditions is known to be beneficial for the resulting homogeneity, this was practically difficult with the small silica gel granules making up the support material used in this work.

Besides IWI, another frequently used impregnation method is 'wet impregnation' or 'diffusional impregnation' in which the support is wetted with the pure solvent before impregnation with the precursor solution.[2,4] Visual inspection of the powder obtained via wet-impregnation after the calcination step however, suggests an even larger heterogeneity because of the darker yellow colour of the obtained bulk powder. As mentioned above, the intensity of the plasmon absorbance of silver nanoparticles decreases upon decreasing their size, while an increasing size results in a more intense and red-shifted absorbance. In addition, also silver loading determines the colour of the resulting powder. Close inspection using optical microscopy indeed reveals the fraction of dark coloured orange to red granules containing excessive amounts of silver and larger silver nanoparticles is strongly increased. The complete colour distribution among the individual supported silver granules as observed via optical microscopy is shown in Figure 3.

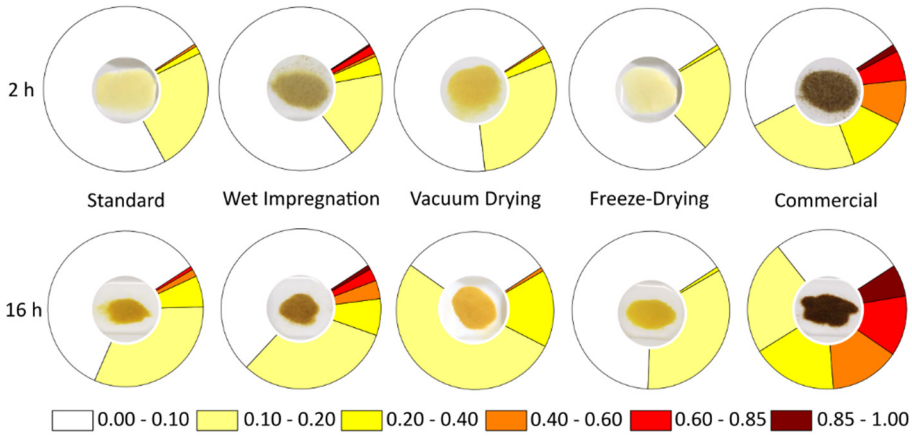

Figure 3 Schematic representation of colour distribution at the catalyst granule level as the result of varying synthesis conditions (5-6 wt% Ag, calcination 2 h (top) and 16 h (bottom) 500 °C). Colour heterogeneity (n = 250) illustrated with pie diagram, colours represent colour index of individual Ag/SiO_2 granules (determination see Supporting Information and ref. 21).

3.3.3 Heterogeneity induced during drying

Typically, drying after impregnation is performed in a static oven without taking into consideration metal precursor redistribution within the bulk powder between individual support granules. To minimize redistribution of metal precursor within individual support granules and to optimize metal dispersion alternative drying methods such as freeze-drying or vacuum drying have been explored.[12,28] Based on these earlier findings, the influence of vacuum drying and freeze-drying on the resulting heterogeneity at the granule scale for our silver on silica powder was evaluated. From the colour distribution shown in Figure 3 it is clear that vacuum drying has a positive effect. Not only does it increase the fraction of light yellow coloured granules, the fraction of darkly coloured orange to red granules decreases similarly. An even more homogeneous colour distribution at the granule scale was obtained after freeze-drying (Figure 3).

3.3.3.1 Drying bed

Clearly, the drying conditions of the freshly impregnated powder play an important role. Within the static drying bed temperature gradients as well as concentration gradients might develop. In order to examine the influence of the position of a support granule inside the drying bed on the resulting colour and thus silver loading, the powdered bed was sliced in half and afterwards calcined while carefully maintaining this same powder configuration. The overview picture taken of the powdered bed after calcination, Figure 4, clearly shows that granules that were present in the interior of the bed during drying are markedly less coloured than

granules that resided closer to the exterior of the bed. This observation conflicts with the general assumption that during drying metal precursor precipitation takes place within or at the outside of the original granule and no migration between granules exists; note that within one support granule precursor migration has been observed.

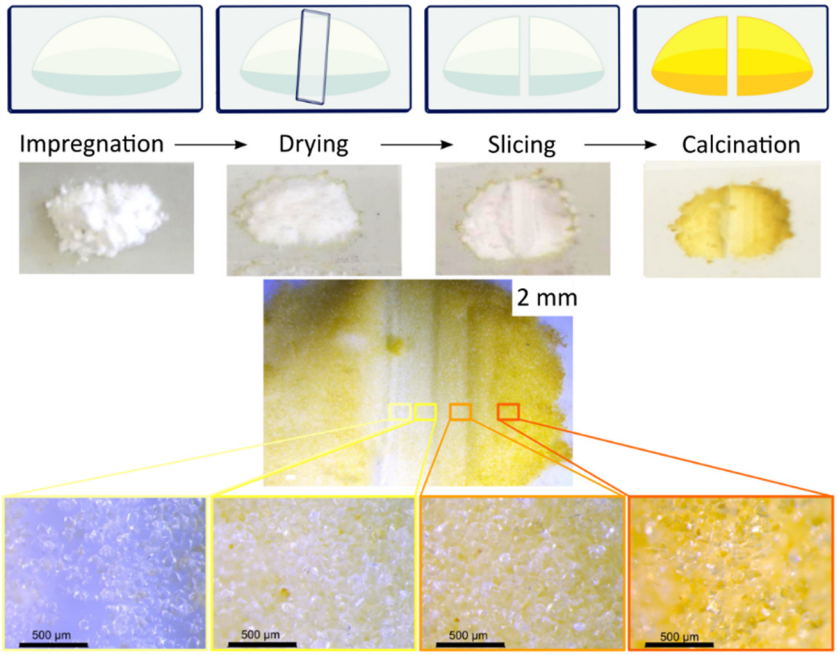

Figure 4 Influence of drying on resulting interparticle colour heterogeneity after incipient wetness impregnation of a silica gel with a silver nitrate solution.

3.3.3.2 Fluidized bed drying

To prevent directional transport of the metal precursor between support granules as is observed during the static drying, an alternative to static drying was investigated. De Jong and co-workers have explored fluidized bed drying approaches to improve the cobalt distribution within mesoporous silica when impregnating with $Co(NO_3)_2$.[20] The impregnated powder is loaded into a tubular reactor through which a gas is blown from bottom to top, creating a fluidized bed. The effect of fluidized bed drying on the resulting colour heterogeneity was tested by drying freshly prepared silver impregnated silica in a fluidized bed reactor under air flow (30 mL/min, 80 % N_2 20 % O_2) at 100 °C for 8 hours. Macroscopically the fluidized bed dried and calcined powder appear more lightly coloured indicating a more homogeneous silver distribution which was also confirmed by optical transmission microscopy. Figure 5 shows the colour distribution in the sample, the fraction of transparent particles is strongly increased from 74 % to 94 %, while the average silver

loading is maintained. Both fluidized bed drying and fluidized bed calcination can be at the origin of the improved homogeneity of the powder. Subsequently a traditionally dried silver on silica powder (100 °C static, 16 h) was calcined in similar fluidized bed condition (air flow 30 mL/min, 80 % N_2 20 % O_2, 1 °C/min to 500 °C for 2 h). The obtained powder strongly resembles that obtained by following the standard impregnation procedure (Figure 2: 2h standard). The remarkable increase in homogeneity can hence be attributed to the fluidized bed drying. Note that also under fluidized bed conditions, the drying temperature plays a crucial role.[20,28] For this particular system a drying temperature of 100 °C was found to give the best results.

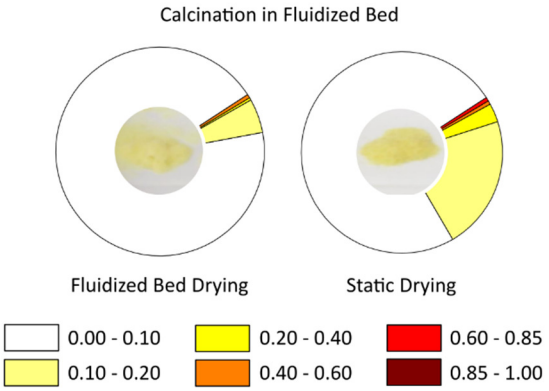

Figure 5 Colour distribution in Ag/SiO_2 after static drying and fluidized bed drying, followed by calcination in fluidized bed (drying 100 °C 8-16 h; calcination 1 °C/min 500 °C – 2 h).

3.3.4 **Heterogeneity induced during calcination**

From the experiments discussed above, the calcination seems not to play a decisive role in the final coloration of the silica supported silver powder i.e. comparison between fluidized bed and static calcination of the standard dried catalysts. When increasing the calcination time from 2 h to 16 h, the increase in coloration of the sample however is significant (Figure 3, top versus bottom row). The prolonged calcination induces thus a transition from non-coloured 6 nm pore confined silver nanoparticles to larger (coloured) silver nanoparticles formed on the outer surface of the granules. Even though the calcination temperature, 500 °C, is well below the melting temperature of silver (962 °C),[29] metal mobility is known to start already at half the melting point, the so-called Tamman temperature. However, nanoparticles do generally not migrate but rather diffuse around their initial position, and since in our sample relatively low loadings compared to the granule diameter are used resulting in relatively large inter nanoparticle distances, nanoparticles moving and coalescing is most likely not the reason for the particle growth. On the other hand,

during calcination in air silver is partially oxidized to silver ions.[30] These silver ions are highly mobile and can migrate between silver nanoparticles, leading to particle growth. This phenomenon, similar to the heterogeneities as a consequence during the drying step, is also related to the relative position of the granule inside the powdered bed during the calcination (see supporting information). When well dispersed individual granules are calcined in an in situ heating stage with minimal temperature gradients, still colour heterogeneities can be observed (see supporting information, Figure S4). The colour heterogeneities that develop under such conditions are however due to the variability induced by the previous steps in the IWI procedure (vide supra).

3.4 DISCUSSION

The experiments with Rhodamine 6G clearly indicate the presence of interparticle heterogeneity in surface charge between the individual silica support granules even before impregnation. This interparticle heterogeneity originates from the calcination step in the preparation procedure of the dry silica gel. Temperature gradients from the outside towards the inside of the of the wet gel must develop. In certain regions more severe heating results in a more drastic dehydration and hence loss of surface hydroxyls. After calcination the solidified gel is crushed into the micrometre-sized granules used as support for metal nanoparticles. In this way, only limited intraparticle heterogeneities in surface hydroxyls can be expected within the granules, as the whole particle originates from the same position within the calcined gel. Moreover, interparticle heterogeneities are expected because of the same reason. This is supported by the Rhodamine 6G experiment, showing a 5-fold variation in negatively charged surface hydroxyl groups between individual granules and no severe variations within the particles.

The experiments focusing on the drying step after impregnation clearly indicate that drying has a large influence on the resulting colour heterogeneity. The influence of the drying step onto to the resulting metal dispersion and distribution inside and on the the support has been extensively studied at the support body level.[15] It has been found that the two factors that determine the final metal loading are (1) convective flow from the inside of the body towards the outer surface induced by evaporation and (2) diffusive transport induced by concentration gradients. Fast drying minimizes such effects preserving maximally the metal precursor distribution inside the support body.[15] However, reports have indicated that for weakly adsorbing metal precursors accumulation of the precursor at the external surface of the support body is significant even at fast drying.[31] This results in the so-called egg-shell metal distribution.[1,4] The final metal distribution in support bodies has thus been shown to be determined by the relative strength of convection, diffusion, and adsorption and

it can be influenced by a variety of parameters like viscosity and pH of the solution, solubility and concentration of the precursor, adsorption strength and size of the support.[1,4,31] To rule out the latter, laboratory scale nanoparticle catalysts are often supported on micrometre-sized granules in which it is believed that these phenomena are not important in contrast to millimetre-sized industrial pellets.[1] The coloration in function of the position in the drying bed (Figure 4) clearly refutes this general assumption. Although the convective and diffusional transport of silver between different granules seems unlikely, these experiments show that silver nitrate transport during drying towards the 'evaporative zone' happens.

Since granule colour is related to silver loading and size of the silver particles on the granule's outer surface, a homogeneous colour distribution originates from both an equal silver loading inside all the individual granules and the formation of only pore confined 6 nm sized silver nanoparticles. The more homogeneous colour distribution as the result of freeze-drying can be attributed to fixation of the solvent to the granules, restricting the exchange of solution between two adjacent granules and is thus a good indication of equal loading. Additionally, by freeze drying there is no liquid-gas interface and hence no capillary effects. Under normal drying conditions a meniscus is formed, which ensures that upon drying larger pores are emptied first, while smaller pores remain fully filled with solution, and the meniscus retracts to the smaller pores, causing redistribution of the active material. Freezing prevents thus migration of the silver nitrate during drying, so more of the silver nanoparticles are located inside the support granule and less large silver particles are formed on the outer surface. The beneficial effect of restricting the exchange of solution between two adjacent granules is further evidenced by the large fraction of transparent granules (94 %) after fluidized bed drying. The transparent colour does not mean that all the fluidized bed dried granules have a very low silver loading, since the same initial silver salt concentration is used in all impregnated samples. The silver nanoparticles inside the transparent granules in the fluidized bed sample are thus all present as pore confined 6 nm sized nanoparticles. In the wet impregnated sample on the contrary, it is more likely that larger silver nanoparticles form on the outer surface giving rise to a higher fraction of orange and red coloured granules. Furthermore, fluidized bed and freeze-drying randomizes the granules within the drying bed. This granule randomization also counters the effect of temperature gradients that develop during traditional drying. The fact that the position inside the drying bed plays such an important role during the IWI procedure probably has been overlooked because of randomization of the granules position between the different steps i.e. the dried powder is typically transferred to a heat resistant crucible for calcination, removing the direct link between final properties and the location.

3.5 CONCLUSION

Optical microscopy was successfully used as a characterization tool to improve the incipient wetness impregnation synthesis of silver nanoparticles supported on silica gel. Variations in silver loading were assessed via the coloration of individual support granules within the resulting powder. The use of other silica support materials, wet-impregnation and prolonged calcination in air induced an even larger interparticle colour heterogeneity at the support granule scale. By changing drying conditions to fluidized bed drying on the contrary, a nearly homogeneous sample was obtained. Comparing the resulting granule colour and its position in the static drying and calcination bed revealed the large impact of temperature gradients and silver transport across the bed on the heterogeneity. In fluidized bed drying, the position of the individual granules is continuously randomized eliminating this impact. During freeze-drying the exchange of solution between two adjacent granules is restricted leading to a homogeneous loading. Additionally, freezing prevents migration of the silver nitrate to the surface during drying, resulting in more silver nanoparticles located inside the support granule and resulting in less large silver particles at the silica's outer surface. This is even more pronounced in fluidized bed drying, the large fraction of transparent granules (94 %) indicates that almost all the silver nanoparticles in this sample are pore confined 6 nm sized nanoparticles. Interestingly, this adaptation to the drying step of the IWI procedure can be easily implemented at the laboratory scale, is scalable and does not require the use of expensive solvents or metal precursors.

Future work will involve determination of single particle silver loading and size and distribution characterization both at the outer surface and inside the granules requiring additional characterization techniques like energy- dispersive X-ray spectroscopy (EDX), scanning electron microscopy (SEM) and transmission electron microscopy (TEM) combined with 3D-representation or sectioning. This work shows that such detailed characterization are best repeated whenever changes to the IWI procedure are implemented. The power of optical microscopy is that simple and fast observation can be easily combined with other more advanced characterization techniques.[21,32,33] Furthermore, optical screening could become a general technique to study catalyst synthesis procedures as it can equally be used for a variety of other metals and metal oxides that also develop colours like Au, Cu, Pt, Pd and Mn.

3.6 REFERENCES

(1) Munnik, P.; de Jongh, P. E.; de Jong, K. P. *Chem. Rev.* **2015**, *115* (14), 6687–6718.
(2) Ertl, G.; Knözinger, H.; Schüth, F.; Weitkamp, J. *Handbook of heterogeneous catalysis*; Wiley-VCH Verlag GmbH & Co. KGaA, 2008; p 3865.
(3) White, R. J.; Luque, R.; Budarin, V. L.; Clark, J. H.; Macquarrie, D. J. *Chem. Soc. Rev.* **2009**, *38* (2), 481–494.
(4) de Jong, K. P. *Synthesis of Solid Catalysts*; Wiley-VCH: Weinheim, Germany, 2009; pp 1–401.
(5) Dinnebier, R.; Billinge, S. *Powder diffraction: theory and practice*; The Royal Society of Chemistry: Cambridge, 2008; pp 17–19.
(6) Quinten, M. *Appl. Phys. B Lasers Opt.* **2001**, *73* (4), 317–326.
(7) Lyu, J.; Wang, J.; Lu, C.; Zhang, Q.; He, X.; Li, X. *J. Phys. Chem. C* **2014**, *118*, 2594–2601.
(8) Arve, K.; Kannisto, H.; Ingelsten, H. H.; Eränen, K.; Skoglundh, M.; Murzin, D. Y. *Catal. Letters* **2011**, *141* (5), 665–669.
(9) Corro, G.; Pal, U.; Ayala, E.; Vidal, E. *Catal. Today* **2013**, *212*, 63–69.
(10) Wei, H.; Gomez, C.; Liu, J.; Guo, N.; Wu, T.; Lobo, R.; Christopher, L.; Lobo-Lapidus, R.; Marshall, C. L.; Miller, J. T.; Meyer, R. J. *J. Catal.* **2013**, *298*, 18–26.
(11) Shimizu, K.; Miyamoto, Y.; Satsuma, A. *J. Catal.* **2010**, *270* (1), 86–94.
(12) Prieto, G.; Zečević, J.; Friedrich, H.; de Jong, K. P.; de Jongh, P. E. *Nat. Mater.* **2013**, *12* (1), 34–39.
(13) Zečević, J.; van der Eerden, A. M. J.; Friedrich, H.; de Jongh, P. E.; de Jong, K. P. *ACS Nano* **2013**, *7* (4), 3698–3705.
(14) Zečević, J.; Vanbutsele, G.; de Jong, K. P.; Martens, J. A. *Nature* **2015**, *528* (7581), 245–248.
(15) Morbidelli, M.; Gavriilidis, A.; Varma, A. *Catalyst design: Optimal Distribution of Catalyst in Pellets, Reactors, and Membranes*; Cambridge University Press, 2001; p 227.
(16) Vergunst, T.; Kapteijn, F.; Moulijn, J. A. *Appl. Catal. A Gen.* **2001**, *213*, 179–187.
(17) Liu, X.; Khinast, J. G.; Glasser, B. J. *Chem. Eng. Sci.* **2012**, *79*, 187–199.
(18) Sietsma, J. R.; Friedrich, H.; Broersma, A.; Versluijs-Helder, M.; Jos van Dillen, A.; de Jongh, P. E.; de Jong, K. P. *J. Catal.* **2008**, *260* (2), 227–235.
(19) Eggenhuisen, T. M.; Friedrich, H.; Nudelman, F.; Zecevic, J.; Sommerdijk, N. A. J. M.; de Jongh, P. E.; de Jong, K. P. *Chem. Mater.* **2013**, *25*, 890–896.
(20) Munnik, P.; de Jongh, P. E.; de Jong, K. P. *J. Am. Chem. Soc.* **2014**, *136*, 7333–7340.
(21) Plessers, E.; Stassen, I.; Sree, S. P.; Janssen, K. P. F.; Yuan, H.; Martens, J.; Hofkens, J.; De Vos, D.; Roeffaers, M. B. J. *ACS Catal.* **2015**, *5*, 6690–6695.
(22) Sun, Y.; Xia, Y. *Analyst* **2003**, *128* (6), 686.
(23) Lee, S.-Y.; Aris, R. *Catal. Rev.-Sci.Eng.* **1985**, *27* (2), 207–340.
(24) Park, J.; Regalbuto, J. *J. Colloid Interface Sci.* **1995**, *175*, 239–252.
(25) Kosmulski, M. *Chemical Properties of Material Surfaces*; Marcel Dekker Inc: New York Basel, 2001.
(26) Behrens, S. H.; Grier, D. G. *J. Chem. Phys.* **2001**, *115* (14).
(27) Eggenhuisen, T. M.; Van Steenbergen, M. J.; Talsma, H.; de Jongh, P. E.; de Jong, K. P. *J. Phys. Chem. C.* **2009**, 16785–16791.
(28) Munnik, P.; Krans, N.; Jongh, P. De; Jong, K. De. *ACS Catal.* **2014**, *4*, 3219–3226.
(29) Brumby, A.; Braumann, P.; Zimmermann, K.; Van Den Broeck, F.; Vandevelde, T.; Goia, D.; Renner, H.; Schlamp, G.; Weise, W.; Tews, P. T. *Ullmann's Encyclopedia of Industrial Chemistry*; Wiley-VCH Verlag GmbH & Co, 2012; p vol. 33 p 15–94.
(30) Hu, J.; Cai, W.; Zeng, H.; Li, C.; Sun, F. *J. Phys. Condens. Matter* **2006**, *18* (23), 5415–5423.
(31) Lekhal, A.; Glasser, B. J.; Khinast, J. G. *Chem. Eng. Sci.* **2001**, *56*, 4473–4487.
(32) Liv, N.; Zonnevylle, C. A.; Narvaez, A. C.; Effting, A. P. J.; Voorneveld, P. W.; Lucas, M. S.; Hardwick, J. C.; Wepf, R. a; Kruit, P.; Hoogenboom, J. P. *PLoS One* **2013**, *8* (2).
(33) Debroye, E.; Van Loon, J.; Gu, X.; Franklin, T.; Hofkens, J.; Janssen, K. P. F.; Roeffaers, M. B. J. *Part. Part. Syst. Charact.* **2016**, 1–7.

CHAPTER 4

CHEMOSELECTIVE REDUCTION OF α,β-UNSATURATED CARBONYL COMPOUNDS WITH UIO-66 MATERIALS

E. Plessers, D. E. De Vos, and M. B. J. Roeffaers. Adapted with permission from: *Journal of Catalysis*, **2016**, *340*, 136-143 (dx.doi.org/10.1016/j.jcat.2016.05.013).

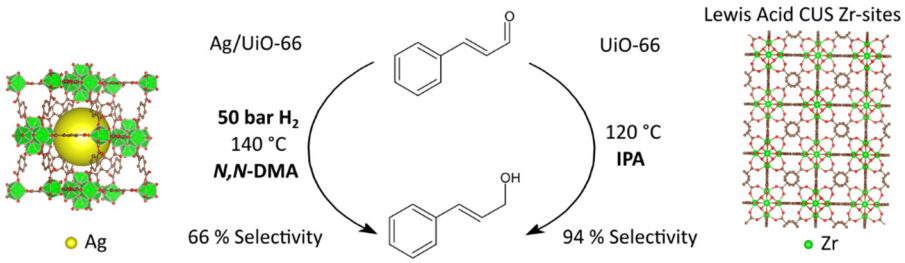

Abstract

In contrast to the traditional silica supported silver catalysts used in chapters 2 and 3, here a new selective silver reduction catalyst is developed by pore confinement in an innovative material: zirconium-based metal–organic framework UiO-66. A recyclable 10 wt% Ag/UiO-66 catalyst reached complete conversion in the chemoselective hydrogenation of cinnamaldehyde with 66 % selectivity for cinnamyl alcohol in the inert solvent *N,N*-dimethylacetamide. Surprisingly, pure UiO-66 as Meerwein-Ponndorf-Verley catalyst with isopropyl alcohol reached complete conversion with > 90 % selectivity. The substrate scope was extended to other α,β-unsaturated carbonyl compounds and introduction of a NO_2-functional group into the UiO-66 linker increased the Lewis acidity and was clearly beneficial for the conversion of carvone.

Contributions and supporting information

The main part of the experimental work was performed by Eva Plessers, Dries De Sloovere and Xian Gu; the article writing was performed by Eva Plessers. Supporting information to Chapter 4 can be found in Appendix 3 on page 123.

CHAPTER 4 – UIO-66 AS AG SUPPORT AND MPV CATALYST

4.1 INTRODUCTION

Allylic alcohols, important intermediates in the pharmaceutical, fragrance and agrochemical industry, are typically obtained through chemoselective reduction of α,β-unsaturated aldehydes. Hydrogenation of the olefinic group yields saturated aldehydes whereas hydrogenation of the carbonyl group produces allylic alcohols. Cinnamaldehyde, citral and crotonaldehyde are widely used as reference α,β-unsaturated aldehydes.[1] The former two are attractive since the unsaturated alcohol products are used as raw material in e.g. the pharmaceutical and fragrance industry; the cardiovascular drug cinnarizine is derived from cinnamyl alcohol[2] and nerol and geraniol derived from citral are useful for the production of perfumes, food flavours and insecticides.[3-5] The chemoselective reduction of carbonyl bonds in enones or enals is however challenging. Typically, this reduction is performed either under high hydrogen pressure conditions with supported metal nanoparticle catalysts or via transfer hydrogenation with an alcohol as hydride donor and a Lewis acid catalyst. The former process is not straightforward since olefins are often preferentially reduced, due to thermodynamic and kinetic reasons,[6-9] the latter on the contrary is selective in carbonyl-hydrogenation but also produces by-products[10-13] and has minor atom efficiency since besides the desired product also a ketone is formed.[14]

The chemoselectivity in the metal nanoparticle catalysed hydrogenation of unsaturated carbonyl compounds to the unsaturated alcohol product depends on various factors such as the metal used as catalyst as well as the chemical nature of the aldehyde and reaction conditions. Various supported metal nanoparticles have been reported so far aiming for the selective hydrogenation of α,β-unsaturated aldehydes.[2,5,15-22] In these catalysts the use of small metal nanoparticles maximises the catalyst surface area; however, it also demands proper stabilisation by an appropriate catalyst support.[23] A well-considered choice of support is a key parameter in superior catalyst development as pore size, specific surface area and acidity can differ largely. These supports could also influence the selectivity towards carbonyl bond hydrogenation through metal–support interaction.[24] Typical supports are metal oxides, such as acidic Al_2O_3, SiO_2, TiO_2 and basic MgO, as well as active carbon.[2,18,25-30] Less studied support materials are metal–organic frameworks (MOFs). MOFs are crystalline, porous materials composed of metal (oxide) nodes

interlinked by polytactic organic ligands, thus forming three dimensional zeolite-like structures with well-defined micropores and pore channels. These solids have attracted researchers' interest mainly due to their versatility, high surface area and acid-base properties. To the best of our knowledge there are only three reports on the use of a MOF-support in the chemoselective hydrogenation of α,β-unsaturated aldehydes. Pt nanoclusters were confined in the cavities of amino-functionalised UiO-66 and displayed high selectivity (92 %) to cinnamyl alcohol;[31] MIL-101 supported Pt nanoparticles on the contrary were >99.9 % selective in the hydrogenation of the C=C bond to form hydrocinnamaldehyde.[15] The results when using Pd/MIL-53(Cr) and Ru/MIL-53(Cr) in the hydrogenation of cinnamaldehyde and crotonaldehyde were somewhat mixed. In the case of cinnamaldehyde the Pd-catalyst preferentially hydrogenated the C=C bond while the Ru-catalyst preferentially hydrogenated the C=O bond. In the case of crotonaldehyde however, the selectivity trend was totally different: the C=C double bond was preferentially hydrogenated on Ru/MIL-53(Cr) whereas C=C and C=O hydrogenation occurred at a similar reaction rates on Pd/MIL-53(Cr).[19]

Alternatively, unsaturated aldehydes and ketones can be selectively reduced to the corresponding allylic alcohols with high chemoselectivity in the absence of hydrogen gas via the Meerwein–Ponndorf–Verley (MPV) reduction.[10] The earliest reported MPV catalysts were aluminium alkoxides,[32] but in the last 15 years zirconium-based catalysts are attracting more and more attention.[12,13,33-39] With Zr-grafted siliceous MCM-41 and SBA-15 yields up to 95% were obtained within reasonable reaction times with relatively small amounts of catalyst (5–8.4 mol%).[12,33,34] Catalytic performance was increased by incorporation of Zr in zeolite beta.[35,36,40] This heterogeneous catalyst was reusable, stable in water and only 1.3 mol% Zr was used. Recently a mesoporous zirconium–phytic acid hybrid material was tested as a MPV catalyst for the conversion of levulinic acid into γ-valerolactone and other carbonyl compounds;[39] high yield and selectivity were obtained, however with 65 mol% Zr. In these MPV catalysts the presence of Lewis acid zirconium sites is essential. Recently, Cirujano and co-workers[41] successfully showed the presence of Lewis acid centres in UiO-66 and used these Zr-based MOFs for the esterification of levulinic acid with various alcohols. The catalytically active sites are coordination vacancies of the Zr-metal, arising from crystalline defects associated with linker deficiencies or from thermal dehydroxylation of the Zr-cluster.[41,42] Preliminary experiments with Zr-containing MOFs, UiO-66 and UiO-66-NO_2, as MPV reduction catalysts with *tert*-butylcyclohexanone as the reactant, already showed the potential of these materials for application in more challenging selective reductions such as those of unsaturated aldehydes and ketones used in this work.[38] Literature suggests that the use of HCl

and trifluoroacetic acid can be used in the modulated UiO-66 synthesis to yield a more open framework structure with a large number of coordinative vacancies.[38]

In this work we explored the use of UiO-66 as support for silver nanoparticles for the chemoselective high pressure hydrogenation of α,β-unsaturated aldehydes. From the literature it is known that the hydrogenation of C=O bonds over C=C bonds in α,β-unsaturated aldehydes decreases, roughly, in the order Ag > Au > Pd > Pt > Ru.[2] Alternatively, we explored the potential of bare UiO-66 materials without supported noble-metal particles as catalysts in the chemoselective formation of allylic alcohols in the MPV reduction using isopropyl alcohol.

4.2 EXPERIMENTAL SECTION

4.2.1 **Synthesis**

All chemicals and solvents used in the syntheses were of reagent grade and used without further purification.

4.2.1.1 UiO-66 materials

All UiO-66 MOFs were made in a closed Schott DURAN® pressure plus bottle with a volume of 1 L under static conditions. UiO-66 and UiO-66-NO_2 were synthesised in the presence of a modulator, starting from an equimolar solution of $ZrCl_4$ (3.5 g, 15 mmol) and terephthalic acid (2.5 g, 15 mmol) or 2-nitroterephthalic acid (3.2 g, 15 mmol), dissolved in *N,N*-dimethylformamide (DMF) (155 mL, 2 mol). 1.5 mL of a 36 wt% solution of HCl (17 mmol) and 20 equivalents (23 mL) of the modulator CF_3COOH were also added to the mixture. UiO-66-NH_2 was synthesised without the modulator,[31] also starting from an equimolar mixture of $ZrCl_4$ (0.48 g, 2.1 mmol) and 2-aminoterephthalic acid (0.372 g, 2.1 mmol) dissolved in DMF (120 mL), to which 0.15 mL of H_2O was added. All synthesis mixtures were placed in a preheated oven at 120 °C for 21 h (modulated) or 24 h (non-modulated synthesis). The powders were collected via centrifugation (10 min, 11 000 rpm) and thoroughly washed with DMF (3 times) and methanol (3 times). The powders were then dried at 60 °C over night and at 200 °C for 24 h to yield 3.48 g (UiO-66), 3.70 g (UiO-66-NO_2) and 0.727 g (UiO-66-NH_2) of activated sample, which correspond to respectively 84%, 80% and 98% molar Zr yield.

4.2.1.2 Supported Ag nanoparticles

Before Ag infiltration of the MOF-supports, they are activated at 150 °C for 16 h in static air. Silver nitrate (512 mg $AgNO_3$, 3 mmol) is dissolved in 6 mL of a H_2O:EtOH 1:5 solution. This aqueous–ethanolic $AgNO_3$ solution is added to a vial containing 200 mg MOF; the vial is sealed with a crimp cap and flushed with nitrogen to remove all O_2. Interaction of Ag^+ ions with light is prevented by a protective layer of aluminium foil around the vial. The MOF–$AgNO_3$ mixture is sonicated for 2 min and stirred continuously for 16 h at 500 rpm. The sample is thoroughly washed (5 times) with ethanol to remove remaining $AgNO_3$ and unbound Ag particles formed in solution; centrifugation (8 min, 3000 rpm), removal of the supernatant and addition of fresh EtOH are performed under an inert atmosphere. Drops of a NaCl-solution are added to the supernatant solution to check whether there is still some Ag^+ present. After washing, the sample is dried in a vacuum oven at room temperature for 16 h.

4.2.1.3 Reference catalysts

γ-Al_2O_3 (Product No. 199974; pore ø = 6 nm, granule size 100 µm), silica gel (Product No. 60752; pore ø = 6 nm, granule size 35 - 75 µm) and ZrO_2 (Product No. 230693; granule size 5 µm) were obtained from Sigma Aldrich. 13 wt% Ag/SiO_2 and Ag/Al_2O_3 were synthesised according to literature procedures.[18,43]

4.2.2 Characterisation

Powder X-ray diffractograms were routinely collected on a STOE STADI COMBI P diffractometer in High-Throughput mode, equipped with an image plate detector using Cu Kα radiation (λ = 1.54056 Å). Scanning Electron Microscopy (SEM) images were obtained using a JEOL SEM (JSM-6010LV). Nitrogen adsorption and desorption isotherms at 77 K were measured using a Micromeritics 3Flex 3500 physisorption instrument. The sample was degassed before measurement at 423 K for 6 h under vacuum (10^{-2} mbar). The pore size distribution was calculated using the BJH method (Harkins and Jura thickness curve and Faas correction, 3Flex 3.00 software). Diffuse Reflectance spectra (DRS) were measured on a Perkin Elmer UV/VIS spectrophotometer (Lambda 950) equipped with a integrating sphere. ICP-AES measurements (Varian 720-ES) were used to determine the Ag-loading. Thermogravimetric Analysis (TGA) was performed under a stream of N_2-gas using a Universal V4.5A TA Instrument running from room temperature to 800 °C with a scan rate of 3.5 °C/min.

4.2.3 Catalytic experiments

4.2.3.1 High H_2 pressure hydrogenation

For the high pressure hydrogenation reaction, 25 mg of catalyst (UiO-66, Ag-loaded and pure, crystal size 0.4 µm aggregated into 1-10 µm sized clusters, pore diameter 1.1 nm and 0.8 nm), 1.15 mmol (145 µL) of cinnamaldehyde, 0.95 mmol tetradecane (245 µL, internal standard) and 3.3 mL of *N,N*-dimethylacetamide (DMA, solvent) were introduced into a 15 mL autoclave. After flushing with N_2, the autoclave was pressurised with H_2 to 20–50 bar of H_2 and stirred with a magnetic stirring bar at 500 rpm. The hydrogenation reaction was performed at 140 °C for 6 h, unless stated otherwise. For analysis of the liquid products, the catalyst was removed by centrifugation (3000 rpm, 8 min) and analysis of the reaction products was carried out using a gas chromatograph (Shimadzu 2010 GC, CP-Sil 8, FID detector). Tetradecane was added as internal standard for quantitative GC analysis. Identification of the compounds was carried out using GC–MS (Agilent, HP-1, MS).

For the recycling test, the used catalyst was isolated from the reaction mixture by centrifugation (3000 rpm, 10 min) and thoroughly washed with DMA (at least three times) until the supernatant was purely solvent, as confirmed by GC. The recovered

catalyst was reactivated overnight (16 h) at room temperature in a vacuum oven (10 mbar) and reused under the same reaction conditions.

4.2.3.2 MPV reduction

Before reaction, each catalyst was dried at 200 °C to remove residual solvent molecules; catalytic reactions were carried out in 10 ml glass crimp cap vials loaded with 20–30 mg catalyst (Zr/substrate ratio was kept constant by varying the amount of catalyst; UiO-66-x: crystal size ± 0.4 µm aggregated into 1-10 µm sized clusters, BET surface area 1237 m^2/g UiO-66 and 1163 m^2/g UiO-66-NO_2) and a magnetic stirring bar. A solution of the substrate (1.15 mmol) in 3.3 mL isopropyl alcohol (IPA) was added; tetradecane was added as internal standard. For each catalyst, a substrate to Zr ratio of 7.8 was used as to compare the activity of each catalyst. After introduction of the reaction mixture, the vials were placed in an aluminium heating block (at 120 °C) and stirred. Reaction samples were filtered through a 0.2 µm PTFE filter (Thermo scientific), and analysed with gas chromatography (Shimadzu 2010 GC, CP-Sil 8, FID detector). Reaction products were identified using GC–MS (Agilent, HP-1, MS). Reactions were performed in duplicate, and the results shown are averaged.

For the recycling test, the used catalyst was isolated from the reaction mixture by centrifugation (3000 rpm, 10 min) and thoroughly washed with isopropyl alcohol (at least three times) until the supernatant was purely solvent, as confirmed by GC. The recovered catalyst was reactivated at 60 °C (2–4 h) and 150 °C (overnight, 16 h) and reused under the same reaction conditions.

4.3 RESULTS AND DISCUSSION

4.3.1 **Chemoselective reduction of cinnamaldehyde under high H_2 pressure**

UiO-66 is a zirconium-terephthalate based metal–organic framework (MOF) which is best known for its high chemical and thermal stability and easy functionalisation. When HCl and trifluoroacetic acid are added to the MOF synthesis mixture, terephthalate linkers are partially replaced by trifluoroacetate, resulting in a more open framework with a large number of open sites.[38] Trifluoroacetate acts as a modulator in this case since it has a similar chemical functionality as the terephthalate linker, but has only one functional group. Since modulated synthesis also increases physical stability,[44] we followed this approach to synthesise our catalyst support. Characterisation was performed with powder X-ray diffraction (XRD), Scanning Electron Microscopy (SEM), N_2-physisorption and Fourier Transform Infrared (FTIR) spectroscopy (see supporting information, Figures S1–4). Ag nanoparticles were introduced into the porous MOFs via infiltration with an aqueous-ethanolic silver nitrate solution. Further, addition of a reductant or inclusion of an additional reduction step was not necessary since Ag(I) is effectively reduced in the presence of EtOH to Ag(0).[45] The formation of Ag nanoparticles was evidenced by diffuse reflectance spectroscopy of the yellow Ag/UiO-66 powder (DRS) (Figure 1); the extra absorption maximum around 400 nm can be assigned to surface plasmon resonance (SPR) of small Ag nanoparticles (<10 nm).[46] The absence of larger silver particles was further supported by powder XRD of the Ag/UiO-66 which would give rise to 38.1° reflection of Ag [111], and further no significant framework decomposition was observed (Figure S1). ICP-AES measurements show a Ag-loading of 10–14 wt%.

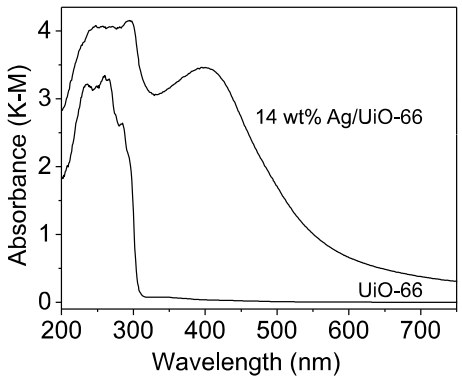

Figure 1 Diffuse Reflectance UV/Visible spectra of UiO-66 and 14 wt% Ag-loaded UiO-66 after Kubelka-Munk (K-M) correction.

Chemoselective hydrogenation of cinnamaldehyde (CALD) was carried out at 140 °C and 30 bar of H_2 in *N,N*-dimethylacetamide (DMA) as the solvent. Catalytic activity of UiO-66 supported silver is clearly visible; in contrast to the thermodynamically favoured C=C hydrogenation, cinnamyl alcohol (CALH) is the preferentially formed product with a selectivity of 66 ± 3 % (Table 1, entry 1). As expected, the hydrogenation rate increases with higher hydrogen pressures, increasing pressure from 30 to 40 and 50 bar of H_2 increases the turn-over frequency to respectively 3.5 ± 0.1 and 5.5 ± 0.1 mol cinnamyl alcohol per mol Ag per hour (Table 1, entry 1–3). Interestingly this pressure increase has no significant effect on the selectivity towards cinnamyl alcohol, which remains 65–70 %. Reference Ag/SiO_2 and Ag/Al_2O_3 catalysts with similar Ag-loadings were used under the same reaction conditions (Table 1, entry 5–6). The Ag/SiO_2 powder shows a comparable reaction selectivity (71 ± 3 %), however with a slightly higher hydrogenation rate (TOF of 6.1 ± 0.1 mol CALH/mol Ag/h). On the other hand, strongly reduced CALH selectivity of 47 ± 5 % was obtained with Ag/Al_2O_3. This is most probably related to the formation of larger Ag nanoparticles as seen on powder XRD of this black powder (Figure S1). The choice of the support has thus an important influence on the formation and stabilisation of the Ag nanoparticles and the resulting catalytic properties. The chemoselective formation of CALH has been reported before for PVP-stabilized Ag nanocolloids, with up to 93 % selectivity after 48 h.[17] Although these stabilized nanoparticles were successfully recycled, heterogenisation of nanoparticles on solid supports typically facilitates synthesis and removal of the reaction medium, and improves thermal and chemical stability.[47] In contrast, the use of silica supported copper catalysts resulted exclusively in the undesired HCAL during the initial stages of the reaction.[27]

Table 1 Conversion and selectivity in the reduction of cinnamaldehyde (CALD) in *N,N*-dimethylacetamide, catalysed by UiO-66, Ag/UiO-66 and a Ag/SiO_2 reference catalyst.

Entry	Catalyst	H_2 (bar)	Wt% Ag[a]	X (%)	TOF[b]	S_{CALH} (%)	S_{HCAL} (%)	S_{HCALH} (%)
1	Ag/UiO-66	30	14	82	3.3	66	30	2
2	Ag/UiO-66	40	10	64	3.5	69	29	1
3	Ag/UiO-66	50	10	>99	5.5	66	27	6
4	UiO-66	30	0	<1	/	/	/	/
5[c]	Ag/SiO_2	30	13	90	6.1	71	28	1
6	Ag/Al_2O_3	50	13	96	2.9	47	36	18

CALD=cinnamaldehyde, CALH =cinnamyl alcohol, HCAL=hydrocinnamaldehyde, HCALH=hydrocinnamyl alcohol ; Reaction conditions: CALD (1.15 mmol), *n*-tetradecane (0.95 mmol), solvent *N,N*-DMA (3.3 mL), 25 mg catalyst, 140 °C, 6 h, 500 rpm. a) determined via ICP-AES b) mol CALH per mol Ag per h c) 4 h.

As can be seen in Table 1 the main products are cinnamyl alcohol (CALH, 66-69 % selectivity) and hydrocinnamaldehyde (HCAL, 27-30 % selectivity). The consecutive hydrogenation product of both compounds, hydrocinnamyl alcohol (HCALH), is only formed in small amounts, even at high conversions. One other by-product was detected in small amounts, typically 1-2 %, and identified by GC-MS as *N,N*-dimethylcinnamylamine (DMC). As shown in Scheme 1, in the presence of an acid catalyst cinnamaldehyde can react with a secondary amine, like dimethylamine, the thermal decomposition product of *N,N*-dimethylacetamide, to form an enamine.[48,49] After selective hydrogenation catalysed by the Ag/UiO-66 catalyst, *N,N*-dimethylcinnamylamine (DMC) is formed, which proves that the Ag catalyst typically also prefers C=N over C=C hydrogenation. *N*,*N*-DMA was chosen as solvent since the amide group will coordinate with free Zr-sites of the MOF framework, avoiding the influence hereof (vide infra) and thus only the catalytic selectivity of the Ag nanoparticles is observed.

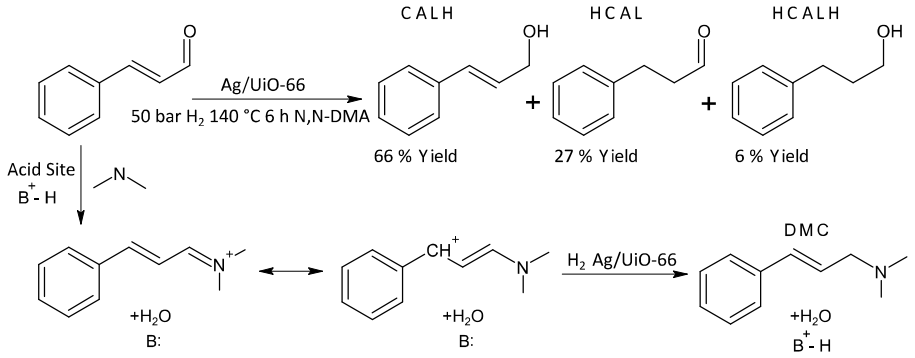

Scheme 1 Reaction products of the hydrogenation of cinnamaldehyde with UiO-66 supported Ag nanoparticles, determined via GC-MS (CALD = cinnamaldehyde, CALH = cinnamyl alcohol, HCAL = hydrocinnamaldehyde, HCALH = hydrocinnamyl alcohol).

To confirm that the observed catalytic activity can solely be attributed to the Ag nanoparticles, the reaction was also performed with pure UiO-66. As can be seen in Table 1 (entry 4) no significant conversion of CALD was detected in this blank reaction after 6 h. A known problem with supported silver catalysts is the facile silver aggregation during the catalytic experiment resulting in a rapidly decreasing catalytic performance. The aggregation of silver in larger clusters typically induces a colour change in the material. Upon visual inspection no significant colour changes occurred with the yellow Ag/UiO-66 powder during the catalytic test which shows that the UiO-66 support strongly suppresses Ag nanoparticle aggregation. This is further supported by powder XRD of the Ag-loaded materials before and after CALD hydrogenation (Figure S5). Powder XRD of the Ag-loaded UiO-66 after catalytic

reaction indicates that the crystallinity of the UiO-66-framework remained intact and no additional diffraction peaks were observed. In the case of Ag-loaded silica on the contrary, an additional diffraction at 38.3° can be attributed to Ag [111] reflections from larger aggregated Ag particles. Ag leaching from the UiO-66 support to the reaction mixture during the course of the reaction was furthermore not detected by ICP-AES on the product mixture (< 0.05 ppm, detection limit). To further test the stability of the Ag/UiO-66 catalyst, a recycle study was conducted. The used catalyst was isolated from the reaction mixture by centrifugation (3000 rpm, 10 minutes) and thoroughly washed with DMA until the supernatant was purely solvent, as evidenced by GC. The recovered catalyst was reactivated overnight at room temperature in a vacuum oven (10 mbar) and reused under the same reaction conditions. Powder XRD and SEM showed that the crystallinity was retained after the washing and reactivation (see supporting information, Figure S5). In reactions with the recycled catalysts, the original catalytic activity was retained at > 99 % up to 5 times recycling with only minor loss in chemoselectivity which in the last reaction was still 60 $\pm$ 3 % to cinnamyl alcohol (see supporting information, Figure S6). These recycling experiments evidence the durability and reusability of the catalyst. The conversion and selectivity obtained with these recyclable UiO-66 supported silver catalysts are however still lower than the results for the reference silver on silica catalyst. Under these high pressure and temperature conditions with an inert solvent such as DMA, higher selectivity can probably only be achieved by the use of multi-component metal nanoparticles.[6,25]

4.3.2 Transfer hydrogenation with UiO-66 and analogues

High conversions in the cinnamaldehyde (CALD) chemoselective hydrogenation are often reported when using isopropyl alcohol (IPA) as a solvent. Under such conditions, using IPA instead of DMA as solvent and with 30 bar of H_2, the Ag/UiO-66 catalyst shows a remarkably higher hydrogenation selectivity of 83 $\pm$ 2 % and a conversion of 81 $\pm$ 3 % after 6 h at 140 °C (Table 2, entry 1). Even higher reaction selectivity is obtained in the absence of the supported silver nanoparticles; pure UiO-66 displays over 90 $\pm$ 2 % selectivity towards cinnamyl alcohol (CALH) at complete conversion (Table 2, entry 2). This can be explained by the fact that zirconium is known to be a transfer hydrogenation catalyst, often in combination with IPA as hydride donor, a mechanism called the Meerwein-Ponndorf-Verley (MPV) reduction.[50] MPV reduction with modulated UiO-66 and UiO-66-NO_2 as catalysts and with *tert*-butylcyclohexanone as the reactant obtained 93 $\pm$ 2 % yield with 10 mol % Zr within 24 h.[38] The excellent catalytic performance of UiO-66, even in the absence of H_2 (Table 2, entry 3), can thus be explained by the MPV reduction mechanism.[10,51]

Table 2 Conversion and selectivity in the reduction of cinnamaldehyde in isopropyl alcohol, catalysed by Ag-loaded UiO-66 or by UiO-66 as such.

Entry	Catalyst	H_2 (bar)	X (%)	S_{CALH} (%)	S_{HCAL} (%)	S_{HCALH} (%)	$S_{Ether}^{(a)}$ (%)	$S_{Acetal}^{(b)}$(%)
1	Ag/UiO-66	30	81	83	5	11	<1	1
2	UiO-66	30	>99	93	0	6	1	<1
3	UiO-66	0	>99	92	0	6	1	<1

CALD=cinnamaldehyde, CALH=cinnamyl alcohol, HCAL=hydrocinnamaldehyde, HCALH=hydrocinnamyl alcohol ; Reaction conditions: CALD (1.15 mmol),*n*- tetradecane (0.95 mmol), solvent IPA (3.3 mL), 25 mg catalyst, 500 rpm, 140 °C, 6 h, 30 bar of H_2. a) 1-cinnamyl-2-propyl ether and b) cinnamaldehyde diisopropyl acetal side products (Scheme 2).

As mentioned above MPV reduction of unsaturated aldehydes and ketones to the corresponding alcohols is an alternative route to obtain allylic alcoholic intermediates with high chemoselectivity and without the use of hydrogen gas. MPV reductions in isopropyl alcohol (IPA) are typically performed at reflux conditions, more specifically at 82 °C with IPA in large excess, to force the equilibrium reaction towards the allylic alcohol product. With Zr-grafted siliceous SBA-15 cinnamyl alcohol yield of 56 % was obtained at 82 °C within 5 h with 8.4 mol % Zr.[34] Catalytic performance was increased by incorporation of Zr in zeolite beta, after 3 h at 82 °C, 96 % yield was obtained with 1.3 mol% Zr.[36] When UiO-66 is used in these conditions, conversion is relatively low (17 $\pm$ 2 %) and the selectivity for the desired CALH drops back to 68 $\pm$ 3 % after 24 h (Table 3, entry 1). The reported selectivity in this case however does not reflect the intrinsic hydrogenation selectivity towards the carbonyl group as the unwanted hydrocinnamaldehyde (HCAL) is not formed, but rather reflects the formation of other side products. Based on GC-MS these compounds were identified as 1-cinnamyl-2-propyl ether and cinnamaldehyde diisopropyl acetal (Scheme 2) which form as a result of etherification with an excess

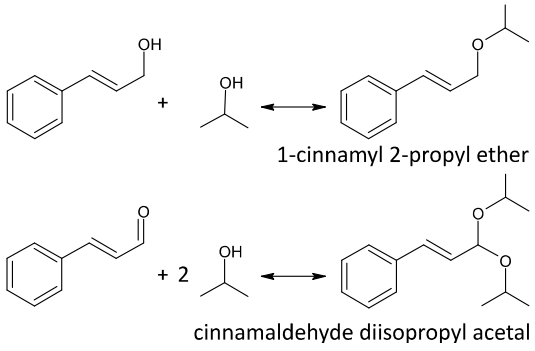

Scheme 2 Side products during transfer hydrogenation of cinnamaldehyde in isopropyl alcohol: 1-cinnamyl 2-propyl ether and cinnamaldehyde diisopropyl acetal.

of isopropyl alcohol. These side products are also reported in literature when hydrous zirconia is used in the MPV reduction of cinnamaldehyde.[11] After 24 h of reaction at 80 °C, the selectivity to 1-cinnamyl 2-propyl was 7.8 % with this hydrous Zr catalyst.

Table 3 Conversion and selectivity in the CALD transfer hydrogenation catalysed by UiO-66, NO_2- and NH_2-functionalized UiO-66 and a reference ZrO_2 catalyst in isopropyl alcohol.

Entry	Catalyst	T (°C)	t (h)	X (%)	S_{CALH} (%)	S_{Ether}[(a)] (%)	S_{Acetal}[(b)] (%)
1	UiO-66	82	24	17	68	2	29
2	UiO-66-NO_2	82	24	18	78	4	17
3	UiO-66-NH_2	82	24	7	28	2	66
4a	UiO-66	120	8	82	95	1	< 1
4b			24	> 99	94	2	0
5a	UiO-66-NO_2	120	8	52	94	1	1
5b			24	84	93	1	< 1
6a	UiO-66-NH_2	120	8	10	87	1	7
6b			24	17	90	1	5
7	ZrO_2	120	24	2	0	0	100

CALD (1.15 mmol), *n*-tetradecane (0.95 mmol), solvent IPA (3.3 mL),7.8 mol% Zr, 500 rpm. a) 1-cinnamyl-2-propyl ether and b) cinnamaldehyde diisopropyl acetal side products (Scheme 2)

Electron withdrawing groups (NO_2) on the organic UiO-66 linker are known to enhance the Lewis acid strength of coordination vacancies of the Zr atoms in the adjacent node,[52] while introducing a basic amino site creates an acid-base catalyst.[53] When UiO-66-NO_2 is used (Table 3, entry 2) conversions only slightly increase from 17 to 18 %, but the selectivity clearly increases to 78 $\pm$ 3 % due to decreased side product formation. As expected amine-functionalization of the linker has the opposite effect; it slows down the reaction with a conversion of only 7 % after 24 h and has a dramatic impact on selectivity, that decreases to 28 $\pm$ 5 % (Table 3, entry 3). However, the decreased performance can also partly be explained by the fact that the UiO-66-NH_2 sample was prepared without modulation. As mentioned before, when HCl and trifluoroacetic acid are used in the modulated UiO-66 synthesis, terephthalate linkers are partially replaced by trifluoroacetate, resulting in a more open framework with a large number of coordinative vacancies.

Recently a mesoporous zirconium-phytic acid hybrid material was tested as a MPV catalyst for the conversion of carbonyl compounds in isopropyl alcohol;[39] high yield

and selectivity were obtained, however with 65 mol% Zr and at 100 °C instead of 82 °C. When increasing reaction temperature to 120 °C for all three UiO-66 materials, conversion and selectivity are considerably improved and side product formation markedly decreases, especially for UiO-66 and UiO-66-NO_2. After 24 h respectively 94 $\pm$ 4 % and 93 $\pm$ 1 % selectivity to cinnamyl alcohol is reached at complete conversion for UiO-66 and 84 $\pm$ 2 % conversion for UiO-66-NO_2. At low conversion cinnamaldehyde diisopropyl acetal was the major side product, when conversion increased also the formation of 1-cinnamyl-2-propyl ether increased. However the side products only account for maximum 2 mol % of the product mixture after 24 h in the case of UiO-66 and UiO-66-NO_2. In the MPV reduction with UiO-66-NH_2 at 120 °C, the selectivity to cinnamaldehyde diisopropyl acetal and 1-cinnamyl-2-propyl ether is respectively 7 and 1 %, considerably less than the reduction at 82 °C where selectivity was respectively 66 and 2 %. All reactions were carried out in duplicate and after hot filtration of the reaction mixture after 5 h to remove the catalyst, conversion did not increase after 24 h, indicating that there is no leaching of Zr into the solution and the catalyst is truly heterogeneous (Figure 2).

To test the recycling of the UiO-66 catalyst, the used catalyst was isolated from the reaction mixture by centrifugation and thoroughly washed with isopropyl alcohol until the supernatant was purely solvent, as evidenced by GC. The recovered catalyst was reactivated at 150 °C and reused under the same reaction conditions. Every recycling step causes a loss in activity of about 35 %, however selectivity to the alcohol is retained at > 90 %. After three recycling steps about 25 % of the initial cinnamyl alcohol yield is preserved. Powder XRD confirms that recycling does not cause a measurable loss in crystallinity (see supporting information, Figure S5). Further, thermal gravimetric analysis (TGA) shows an increase of about 50 °C in the temperature at which the BDC linker is lost from the UiO-66 framework and decomposed (see supporting information, Figure S7). This indicates stronger bonding of the remaining linkers as the result of a decrease in linker molecules per Zr-cluster during reaction and washing.[54] In a UiO-66 metal-organic framework, the Zr-metal is theoretically 8-fold coordinated and possesses no free coordination sites. But as the result of thermal activation and linker deficiency, coordinatively unsaturated Zr-sites (cus Zr) arise turning the Zr-metal into Lewis-acid catalytically active site. The further BDC linker loss during recycling makes the Zr-sites more accessible and also more prone for poisoning, which is confirmed by a visual colour change to light yellow. Linker loss can also lead to leaching of zirconium and empty microdomains.[55,56] However, hot filtration of the catalyst (Figure 2) indicates that leached species are not active as MPV catalyst. Clearly UiO-66 is a very active and selective cinnamaldehyde MPV catalyst, although there is still room for improvement in recyclability of the material.

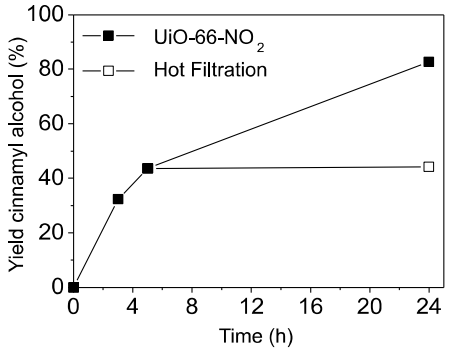

Figure 2 MPV reduction of CALD with UiO-66-NO_2 (■) and hot filtration of the catalyst (□).

With the reference ZrO_2 catalyst no MPV reduction activity is measured (Table 3, entry 7), indicating the successful development of catalytically active cus Zr-sites by incorporation in a metal-organic framework.

UiO-66 was thus successfully used as heterogeneous MPV reduction catalyst for the α,β-unsaturated aldehyde CALD (Figure 3A). Even more challenging is the selective reduction of the α,β-unsaturated linear aldehyde citral and the α,β- unsaturated ketone carvone (Figure 3B,C). The unsaturated alcohol product of the latter is also an important component in the flavour industry.

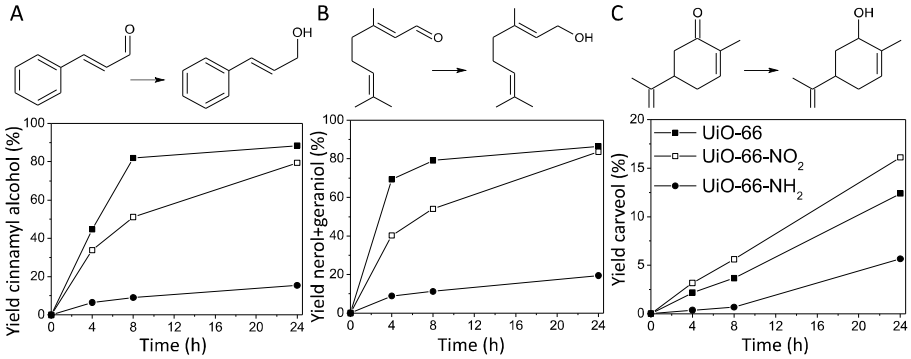

Figure 3 MPV reduction of 3 different α,β-unsaturated carbonyl compounds: **A)** cinnamaldehyde, **B)** *cis,trans*-citral and **C)** carvone catalysed by UiO-66 (■), UiO-66-NO_2 (□) and UiO-66-NH_2 (●) (120 °C, 3.3 mL IPA, substrate:Zr = 7.8).

After 24 h more than 90 % citral conversion is reached, with both UiO-66 and UiO-66-NO_2 and selectivities of respectively 93 ± 1 % and 91 ± 2 %. The negative impact of amine-functionalised linkers is also clearly observed in hydrogenation of both citral and carvone; in all reactions lower conversions and selectivities were reached. Unsaturated ketones are typically harder to selectively reduce than aldehydes, so it

is no surprise carveol yields are lower. In this more demanding reduction reaction higher the stronger acidic UiO-66-NO_2 outperforms UiO-66 (Figure 3C), both catalysts display an excellent hydrogenation selectivity of 92 $\pm$ 3 % towards the desired carveol. Infrared spectroscopy with CD_3CN as probe,[27] confirmed that the NO_2-functionalisation enhances the Lewis acidity of coordination vacancies of the adjacent Zr-metal. Therefore, the catalytic performance in MPV reactions can be expected to decrease in the following order: UiO-66-NO_2 > UiO-66 > UiO-66-NH_2. This trend is not fully obeyed in the MPV reduction of CALD (Figure 3A) and citral (Figure 3B). This can be due to several reasons: (1) the already high transfer hydrogenation activity of UiO-66 with these substrates might mask the enhancement by the NO_2-group, (2) NO_2-functionalisation not only induces the electronic effect of increased Lewis acidity, but may also increase steric hindrance, (3) UiO-66 and UiO-66-NO_2 do not necessarily have exactly the same amount of active sites. However, with more difficult substrates such as carvone the beneficial effect of NO_2-functionalization on the conversion is clearly observed in the transfer hydrogenation.

4.4 CONCLUSION

Zr-based UiO-66 metal-organic frameworks were successfully used for the chemoselective hydrogenation of cinnamaldehyde, both in high pressure hydrogenation as supports for Ag nanoparticles, and as transfer hydrogenation catalyst in the Meerwein-Ponndorf-Verley reduction. A 10 wt % Ag/UiO-66 catalyst reached complete conversion after 24 h at 50 bar of H_2 with 66 % selectivity for cinnamyl alcohol in the inert solvent *N,N*-dimethylacetamide (DMA). Recycling experiments evidenced the durability and reusability of the catalyst since the original catalytic activity was retained up to 5 times recycling with only minor loss in chemoselectivity. Compared to silver loaded alumina and silica, the UiO-66 framework offers a more efficient stabilization of the Ag nanoparticles during catalytic reaction as evidenced by powder XRD. The conversion and selectivity obtained with these UiO-66 supported silver catalysts are however still lower than the reported results for other supported metal catalysts. If high pressure hydrogen driven reduction of α,β-unsaturated carbonyl compounds is compared to Meerwein-Ponndorf-Verley (MPV) reduction, MPV is much more selective in the hydrogenation of C=O bonds when pure UiO-66 was used as transfer hydrogenation catalyst. Complete conversion was reached with > 90 % selectivity without the need of a precious metal. The substrate scope was further extended to citral and carvone, two other α,β-unsaturated carbonyl compounds that are harder to selectively reduce. Although there are side products, the higher selectivity obtained at milder conditions and excellent Lewis acid properties of the Zr-metal in the modulated UiO-66 framework make transfer hydrogenation with this material preferable over high H_2

pressure hydrogenation. The successful use of one material, such as UiO-66, for the same reaction both as support or as catalyst demands critical interpretation of experimental results when using a Lewis acid support material in the high pressure hydrogenation of carbonyl compounds. The catalytic performance of the supported metal nanoparticles in the H_2-driven hydrogenation could be strongly biased by the support-catalysed transfer hydrogenation. Advances in both H_2-driven hydrogenation and MPV reduction are reported on a regular basis, however reports investigating both mechanisms at the same time are rare.

4.5 REFERENCES

(1) Nishimura, S. Handbook of Heterogeneous Catalytic Hydrogenation for Organic Synthesis; John Wiley and Sons: New York, 2001; p 737.
(2) Yuan, Y.; Yao, S.; Wang, M.; Lou, S.; Yan, N. *Curr. Org. Chem.* **2013**, *17*, 400–413.
(3) Saudan, L. A. *Acc. Chem. Res.* **2007**, *40* (12), 1309–1319.
(4) Belitz, H.-D.; Grosch, W.; Schieberle, P. *Food Chemistry*; Springer: Berlin, 2009; p 1070.
(5) Mikkola, J.; Virtanen, P.; Karhu, H.; Salmi, T.; Murzin, D. Y. *Green Chem.* **2006**, *8*, 197–205.
(6) Gallezot, P.; Richard, D. *Catal. Rev. Sci. Eng.* **1998**, *40* (1-2), 81–126.
(7) Claus, P. *Top. Catal.* **1998**, *5*, 51–62.
(8) Ponec, V. *Appl. Catal. A Gen.* **1997**, *149*, 27–48.
(9) Corain, B.; Schmid, G.; Toshima, N. *Metal Nanoclusters in Catalysis and Materials Science: The Issue of Size Control*; Elsevier: Amsterdam, 2007; p 470.
(10) Chuah, G. K.; Jaenicke, S.; Zhu, Y. Z.; Liu, S. H. *Curr. Org. Chem.* **2006**, *10*, 1639–1654.
(11) Liu, S. H.; Jaenicke, S.; Chuah, G. K. *J. Catal.* **2002**, *206* (2), 321–330.
(12) De bruyn, M.; Limbourg, M.; Denayer, J.; Baron, G. V.; Parvulescu, V.; Grobet, P. J.; De Vos, D. E.; Jacobs, P. A. *Appl. Catal. A Gen.* **2003**, *254* (2), 189–201.
(13) Zhu, Y.; Liu, S.; Jaenicke, S.; Chuah, G. *Catal. Today* **2004**, *97* (4), 249–255.
(14) Hagen, J. *Industrial catalysis: a practical approach*; WILEY-VCH: Weinheim, Germany, 2006; pp 281–292; 327.
(15) Liu, H.; Li, Z.; Li, Y. *Ind. Eng. Chem. Res.* **2015**, *54* (5), 1487–1497.
(16) Neri, G.; Arrigo, I.; Corigliano, F.; De Luca, L.; Donato, A. *Catal. Letters* **2011**, *141* (11), 1590–1597.
(17) Mertens, P. G. N.; Vandezande, P.; Ye, X.; Poelman, H.; Vankelecom, I. F. J.; De Vos, D. E. *Appl. Catal. A Gen.* **2009**, *355* (1-2), 176–183.
(18) Steffan, M.; Jakob, a; Claus, P.; Lang, H. *Catal. Commun.* **2009**, *10* (5), 437–441.
(19) Sawai, T.; Yonehara, T.; Yonezawa, A.; Sano, M.; Suzuki, T.; Miyake, T. *J. Japan Pet. Inst.* **2014**, *57* (1), 58–64.
(20) Wei, H.; Gomez, C.; Liu, J.; Guo, N.; Wu, T.; Lobo, R.; Christopher, L.; Lobo-Lapidus, R.; Marshall, C. L.; Miller, J. T.; Meyer, R. J. *J. Catal.* **2013**, *298*, 18–26.
(21) Ide, M. S.; Hao, B.; Neurock, M.; Davis, R. J. *ACS Catal.* **2012**, *2*, 671–683.
(22) Tian, Z.; Li, Q.; Hou, J.; Pei, L.; Li, Y.; Ai, S. *J. Catal.* **2015**, *331*, 193–202.
(23) White, R. J.; Luque, R.; Budarin, V. L.; Clark, J. H.; Macquarrie, D. J. *Chem. Soc. Rev.* **2009**, *38* (2), 481–494.
(24) Furman, K.; Baudouin, D.; Margossian, T.; Sabnis, K. D.; Cui, Y.; Ribeiro, F. H.; Copéret, C. *J. Catal.* **2015**, *324*, 9–13.
(25) Mäki-Arvela, P.; Hájek, J.; Salmi, T.; Murzin, D. Y. *Appl. Catal. A Gen.* **2005**, *292*, 1–49.
(26) Volckmar, C.; Bron, M.; Bentrup, U.; Martin, a; Claus, P. *J. Catal.* **2009**, *261* (1), 1–8.
(27) Chambers, A.; Jackson, S. D.; Stirling, D.; Webb, G. *J. Catal.* **1997**, *168*, 301–314.
(28) Claus, P.; Hofmeister, H. *J. Phys. Chem. B* **1999**, *103* (14), 2766–2775.
(29) Handjani, S.; Marceau, E.; Blanchard, J.; Krafft, J.-M.; Che, M.; Mäki-Arvela, P.; Kumar, N.; Wärnå, J.; Murzin, D. Y. *J. Catal.* **2011**, *282* (1), 228–236.
(30) Bernas, H.; Simakova, I.; Prosvirin, I. P.; Mäki-Arvela, P.; Leino, R.; Murzin, D. Y. *Catal. Letters* **2012**, *142* (6), 690–697.

(31) Guo, Z.; Xiao, C.; Maligal-Ganesh, R. V; Zhou, L.; Goh, T. W.; Li, X.; Tesfagaber, D.; Thiel, A.; Huang, W. *ACS Catal.* **2014**, *4*, 1340–1348.
(32) Wilds, A. L. *Org. React.* **1944**, *2*, 178–223.
(33) De bruyn, M.; De Vos, D. E.; Jacobs, P. A. *Adv. Synth. Catal.* **2002**, *344* (10), 1120–1125.
(34) Zhu, Y.; Jaenicke, S.; Chuah, G. K. *J. Catal.* **2003**, *218* (2), 396–404.
(35) Zhu, Y.; Chuah, G.; Jaenicke, S. *J. Catal.* **2004**, *227* (1), 1–10.
(36) Zhu, Y.; Chuah, G.; Jaenicke, S. *J. Catal.* **2006**, *241* (1), 25–33.
(37) Ramanathan, A.; Castro Villalobos, M. C.; Kwakernaak, C.; Telalovic, S.; Hanefeld, U. *Chem. - A Eur. J.* **2008**, *14* (3), 961–972.
(38) Vermoortele, F.; Bueken, B.; Le Bars, G.; Van de Voorde, B.; Vandichel, M.; Houthoofd, K.; Vimont, A.; Daturi, M.; Waroquier, M.; Van Speybroeck, V.; Kirschhock, C.; De Vos, D. E. *J. Am. Chem. Soc.* **2013**, *135*, 11465–11468.
(39) Song, J.; Zhou, B.; Zhou, H.; Wu, L.; Meng, Q.; Liu, Z.; Han, B. *Angew. Chemie (International Ed.* **2015**, *54*, 9399–9403.
(40) Luo, H. Y.; Consoli, D. F.; Gunther, W. R.; Román-Leshkov, Y. *J. Catal.* **2014**, *320*, 198–207.
(41) Cirujano, F. G.; Corma, a.; Llabrés i Xamena, F. X. *Chem. Eng. Sci.* **2015**, *124*, 52–60.
(42) Valenzano, L.; Civalleri, B.; Chavan, S.; Bordiga, S.; Nilsen, M. H.; Jakobsen, S.; Lillerud, K. P.; Lamberti, C. *Chem. Mater.* **2011**, *23*, 1700–1718.
(43) Shimizu, K.; Sawabe, K.; Satsuma, A. *Catal. Sci. Technol.* **2011**, *1* (3), 331.
(44) Van de Voorde, B.; Stassen, I.; Bueken, B.; Vermoortele, F.; De Vos, D.; Ameloot, R.; Tan, J.-C.; Bennett, T. D. *J. Mater. Chem. A* **2015**, *3* (4), 1737–1742.
(45) Houk, R. J. T.; Jacobs, B. W.; El Gabaly, F.; Chang, N. N.; Talin, A. A.; Graham, D. D.; House, S. D.; Robertson, I. M.; Allendorf, M. D. *Nano Lett.* **2009**, *9* (10), 3413–3418.
(46) Quinten, M. *Appl. Phys. B Lasers Opt.* **2001**, *73* (4), 317–326.
(47) Astruc, D.; Lu, F.; Aranzaes, J. R. *Angew. Chem. Int. Ed. Engl.* **2005**, *44* (48), 7852–7872.
(48) Clayden, J.; Greeves, N.; Warren, S. *Organic Chemistry*; Oxford Universitey Press: New York, 2012; p 1512.
(49) Bruice, P. Y. *Organic Chemistry*, 7th ed.; Pearson: New York, 2014; p 814.
(50) Sheldon, R. A.; van Bekkum, H. *Fine Chemicals through Heterogeneous Catalysis*; WILEY-VCH Verlag GmbH Weinheim, 2001; p Chapter 8.
(51) Boronat, M.; Corma, A.; Renz, M. *J. Phys. Chem. B* **2006**, *110*, 21168–21174.
(52) Vermoortele, F.; Vandichel, M.; Van de Voorde, B.; Ameloot, R.; Waroquier, M.; Van Speybroeck, V.; De Vos, D. E. *Angew. Chem. Int. Ed. Engl.* **2012**, *51* (20), 4887–4890.
(53) Hajek, J.; Vandichel, M.; Van de Voorde, B.; Bueken, B.; De Vos, D.; Waroquier, M.; Van Speybroeck, V. *J. Catal.* **2015**, *331*, 1–12.
(54) Trickett, C. a; Gagnon, K. J.; Lee, S.; Gándara, F.; Bürgi, H.-B.; Yaghi, O. M. *Angew. Chem. Int. Ed. Engl.* **2015**, *54* (38), 11162–11167.
(55) Ling, S.; Slater, B. *Chem. Sci.* **2016**.
(56) Cliffe, M. J.; Wan, W.; Zou, X.; Chater, P. a; Kleppe, A. K.; Tucker, M. G.; Wilhelm, H.; Funnell, N. P.; Coudert, F.-X.; Goodwin, A. L. *Nat. Commun.* **2014**, *5* (May), 4176.

CHAPTER 5

ZR-BASED MOF-808 AS MEERWEIN-PONNDORF-VERLEY REDUCTION CATALYST FOR CHALLENGING CARBONYL COMPOUNDS

E. Plessers, G. Fu, C. Y. X. Tan, D. E. De Vos and M. B. J. Roeffaers. Adapted with permission from: *Catalysts,* **2016**, *6,* 140 (dx.doi.org/10.3390/catal6070104).

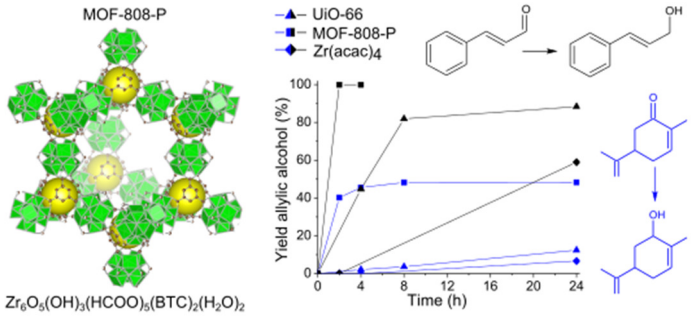

Abstract

Supported by the high activity of the Lewis acid sites of UiO-66 in the Meerwein-Ponndorf-Verley (MPV) reduction described in the previous chapter, another Zr-based metal-organic framework (MOF) MOF-808-P was successfully used as MPV catalyst. After only 2 h 99 % yield of cinnamyl alcohol was obtained (8 mol% Zr). The highly active MOF-808-P is also a good catalyst for the selective reduction of more challenging substrates. Two strategies were successfully used to shift the equilibrium towards the desired allylic alcohol products: 1) evaporation of formed acetone and 2) the use of the more strongly reducing 1-indanol. These results highlight the great potential of this recently discovered Zr-MOF as chemically and thermally stable catalyst.

Contributions and supporting information

The main part of the experimental work and article writing was performed by Eva Plessers, Guangxia Fu synthesized and characterised the materials via SEM and TGA; Collin Tan performed CD_3CN chemisorption measurements. Supporting information to Chapter 5 can be found in Appendix 4 on page 129.

CHAPTER 5 – MOF-808 CATALYSED MPV

5.1 INTRODUCTION

In the fragrance and pharmaceutical industry, allylic alcohols are important intermediates and flavouring compounds.[1] A widespread route to obtaining these allylic alcohols is via the chemoselective reduction of unsaturated aldehydes and ketones. This reduction can be performed via hydrogen transfer from easily oxidizable alcohols catalysed by a Lewis acid or basic catalyst, a procedure called Meerwein–Ponndorf–Verley reduction (MPV).[2] MPV reductions are typically performed under mild conditions and with high chemoselectivity because of the low risk of reducing other functional groups or unsaturated C=C-bonds. The high selectivity can be explained by the mechanism in which a cyclic six-membered transition state is formed.[3,4] Hydrogen donor and acceptor coordinate simultaneously to the Lewis acidic metal centre; via this coordination, the carbonyl group of the substrate is activated for the hydride transfer and the reduction is performed with high selectivity.[5] Isopropyl alcohol (IPA) is the most widely used hydride donor because it is easily oxidized to acetone and is environmentally friendly.[6] The major disadvantage of IPA, however, is the reversibility of the reaction.[7] The reverse complementary oxidation of alcohols is known as the Oppenauer oxidation, resulting in an equilibrium called the Meerwein–Ponndorf–Verley–Oppenauer (MPVO) redox equilibrium.[5] To direct the equilibrium towards the desired allylic alcohol, IPA is often used in excess as the solvent of the reaction.

The earliest reported MPV catalysts were aluminium alkoxides,[8] recent improvements of these homogeneous aluminium catalysts lead to the development of highly efficient aluminium siloxide[9] and enantioselective calixarene-based MPV catalysts.[10,11] However, in the last 15 years, zirconium-based catalysts are gaining interest.[3,7,12-15] The earliest reported Zr-catalysts were unsupported zirconia. In the MPVO reaction of ethanol and acetone, the weakly basic ZrO_2 performed less well than the strongly basic MgO.[16] Hydrous zirconia, on the other hand, proved to be a good MPV catalyst, giving a 78 % cinnamyl alcohol yield,[3] and could be used under flow conditions.[17] Grafting of Zr on siliceous SBA-15 (SBA for Santa Barbara Amorphous type material) or zeolite Beta dramatically decreased the necessary Zr/substrate ratio.[18-20] The Zr-zeolite Beta catalyst—with Zr substituted isomorphously into the lattice—was reusable, stable in water, and only 1.3 mol % Zr was used to reach 96 % cinnamyl alcohol yield within reasonable reaction time. Lewis

acidity of the Zr-atoms in zeolite Beta was increased by a two-step post-synthesis method to reach 100% cinnamyl alcohol yield.[21]

Cinnamaldehyde is one of the most widely used α,β-unsaturated aldehydes. It is an attractive MPV substrate since the unsaturated alcohol product is used as a flowery note,[3] and as raw material in the fragrance and pharmaceutical industry—e.g., for the cardiovascular drug cinnarizine, which is derived from cinnamyl alcohol.[22] Another reason for studying cinnamaldehyde as a reactant is the fact that it is relatively easily reduced chemoselectively compared to other unsaturated aldehydes or ketones because of favourable steric and electronic properties. Citral is another widely studied MPV substrate for which typically lower yields are reached, so longer reaction time or higher Zr-loadings are necessary.[15,19,21,23] Carvone, isophorone, and β-ionone are examples of α,β-unsaturated ketones that are even more difficult to chemoselectively reduce to obtain allylic alcohols in high yields. De bruyn *et al.*[7,24] however, overcame this limitation by using the more strongly reducing 1-indanol as hydrogen donor and siliceous MCM-41 (MCM for Mobil Crystalline Material) immobilized Zr and Hf as catalysts.

Aside from zeolites and mesoporous silicas, Zr-containing metal-organic frameworks (MOFs) have recently been proposed as MPV catalyst. MOFs are crystalline, porous materials composed of metal (oxide) nodes interlinked by polytopic organic ligands, forming three-dimensional structures with well-defined cages and channels. These microporous solids have attracted researchers' interest mainly due to their versatility, high surface area and acid-base properties. Even though concerns have been raised about their thermal and physical stability, MOFs are promising catalysts for the synthesis of high-added-value products.[25-27] UiO-66 (UiO for University of Oslo) is a zirconium-terephthalate-based MOF best known for its high chemical and thermal stability and easy functionalization. When HCl and/or trifluoroacetic acid are added to the MOF synthesis mixture, terephthalate linkers are partially replaced by trifluoroacetate, resulting in a more open framework with a large number of open sites.[14] These Zr-based modulated UiO-66 and UiO-66-NO_2 were already successfully used as MPV reduction catalysts with *tert*-butylcyclohexanone as the reactant[14] and in other challenging selective reductions, such as those of unsaturated aldehydes and ketones.[28] Llabres and co-workers[29] successfully showed the presence of Lewis acid centres in UiO-66 and used these Zr-based MOFs for the esterification of levulinic acid with various alcohols. The catalytically-active sites are coordination vacancies on the Zr-metal, arising from crystalline defects associated to linker deficiencies or from thermal dehydroxylation of the Zr-cluster.[29,30]

Recently, a new range of Zr-MOFs has been reported, all based on the $Zr_6O_4(OH)_4(-CO_2)_n$ secondary building unit (SBU) and variously shaped carboxylic organic linkers.[31] One of these Zr-materials is MOF-808, in which the Zr-SBU is connected to six 1,3,5-

benzenetricarboxylate (BTC) organic linkers and six formate ligands (Figure 1A,B). Every linker is coordinated to three SBUs, resulting in tetrahedral and adamantane-shaped cages with an internal pore diameter of respectively 4.8 Å and 18 Å (Figure 1C,D). These large pores are of interest for use of MOF-808 as MPV reduction catalyst since they might alleviate mass transport limitations and facilitate formation of the six-membered transition state. Furthermore, a new crystalline form of MOF-808—designated as MOF-808-P—has been described; it contains five instead of six formate ligands per cluster, resulting in a coordinatively unsaturated Zr-site.[32] Citronellal cyclization experiments already indicated that MOF-808-P contains Lewis acid sites; such sites are suitable to catalyse MPV reduction.[1]

In this work, MOF-808-P is successfully used as MPV catalyst for various α,β-unsaturated carbonyl compounds. For cinnamaldehyde and citral, allylic alcohol yields of respectively 99 % and 95 % were obtained within a very short reaction time. More challenging substrates, such as *R*-carvone, reached the equilibrium point, but this equilibrium could be shifted towards the desired allyl alcohol by evaporation and the use of 1-Indanol.

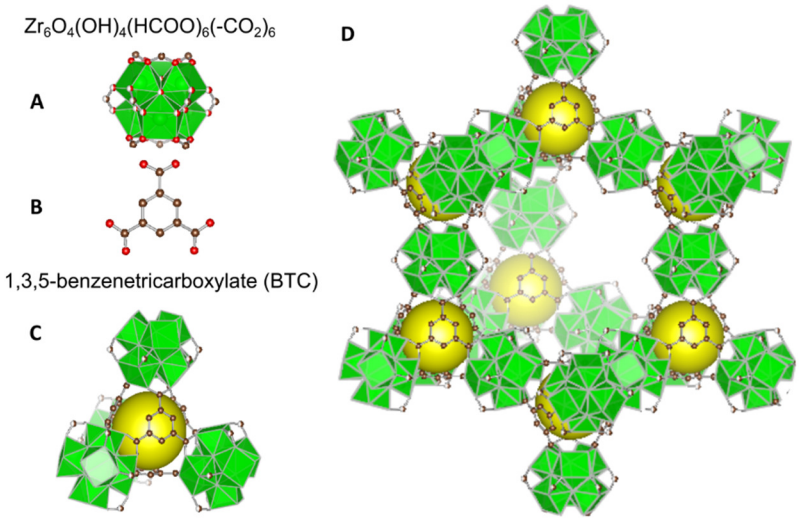

Figure 1 **A)** $Zr_6O_4(OH)_4(HCOO)_6(-CO_2)_6$ metal clusters, and **B**) 1,3,5-benzenetricarboxylate (BTC) linkers form **C**) tetrahedral cages (yellow spheres represent the internal free volume inside these cages with a diameter of 4.8 Å), and **D**) large adamantane-shaped cages, internal free volume with diameter of 18 Å. Zr coordination polyhedral: green; C: brown spheres; O: red spheres; formate C and O: half-filled; H omitted for clarity (based on ref. 31).

5.2 EXPERIMENTAL SECTION

All chemicals and solvents used in the syntheses and catalytic experiments were of reagent grade and used without further purification.

5.2.1 Synthesis and characterisation

5.2.1.1 MOF synthesis

The synthesis was performed according to the reported procedure. All materials were made in a closed Schott DURAN® (VWR, Leuven, Belgium) pressure plus bottle with a volume of 1 L under static conditions starting from a non-equimolar solution of $ZrOCl_2 \cdot 8H_2O$ (9.7 g, 30 mmol, 95 %, ABCR GmbH, Karlsruhe, Germany) and 1,3,5-benzenetricarboxylic acid (BTC) (2.1 g, 10 mmol, 98 %, ABCR GmbH, Karlsruhe, Germany) dissolved in a mixture of N,N-dimethylformamide (DMF) (450 mL, 6 mol, 99+ %, Acros Organics, Geel, Belgium) and formic acid (450 mL, 12 mol, 98+ %, Acros Organics, Geel, Belgium). The synthesis mixture was placed in a preheated oven at 120 °C for 48 h. The powder was collected via centrifugation (10 min, 11 000 rpm) and thoroughly washed with DMF (3 times/day for 3 days) and methanol (HPLC grade, Chem-Lab Analytical BVBA, Zedelgem, Belgium) (3 times/day for 3 days). Finally, the material was activated at 150 °C in air to remove residual solvent molecules.

5.2.1.2 MOF characterisation

Powder X-ray diffractograms were routinely collected on a STOE STADI COMBI P diffractometer (STOE & Cie GmbH, Darmstadt, Germany) in High-Throughput mode, equipped with an image plate detector using Cu Kα radiation (λ = 1.54056 Å). Scanning Electron Microscopy (SEM) images were obtained using a JEOL SEM (JSM-6010LV, Jeol Europe BV, Zaventem, Belgium). MOF-808-P was analysed by Thermogravimetric Analysis (TGA) under a stream of O_2-gas using a Universal V4.5A TA Instrument (TA Instruments, New Castle, USA). CD_3CN chemisorption spectra were measured on a Nicolett 6700 (Thermo Scientific) FTIR (128 scans, resolution of 2 cm^{-1}) and analysed with Omnic software (Version 8.0, Thermo Scientific, Waltham, USA). Inductively Coupled Plasma (ICP)—Atomic Emission Spectra (AES) were recorded on a Varian 720-ES (Varian Inc., Walnut Creek, USA).

5.2.2 Catalytic experiments

Before reaction, each catalyst was dried at 150 °C for 16 hours to remove residual solvent molecules. Catalytic reactions were carried out in 10 ml glass crimp cap vials loaded with 20-30 mg catalyst (Zr/substrate ratio was kept constant by varying the amount of catalyst; crystal size 0,5 µm aggregated into 1-5 µm sized clusters) and a magnetic stirring bar. A solution of the substrate in 3.3 ml isopropyl alcohol (IPA) was

added; tetradecane (99 %, TCI Europe NV, Zwijndrecht, Belgium) was added as internal standard. For each catalyst and substrate, a substrate to Zr ratio of 7.8 was used to compare the activity of each catalyst for every substrate. After introduction of the reaction mixture, the vials were placed in an aluminium heating block (at 120 °C) and stirred (250 rpm). Reaction samples were filtered through a 0.45 µm PTFE filter (Thermo scientific, VWR, Leuven, Belgium) and analysed with a Shimadzu 2010 GC (Shimadzu Benelux BV, Brussel, Belgium) equipped with a CP-Sil 8 column and a FID detector. Reaction products were identified using GC-MS (Agilent Technologies Belgium, Diegem, Belgium).

5.3 RESULTS

5.3.1 **Reduction of cinnamaldehyde and carvone**

Zr-based MOF-808-P was synthesized according to the reported procedure, starting from $ZrOCl_2.8H_2O$ and 1,3,5-benzenetricarboxylic acid (BTC) dissolved in a mixture of *N,N*-dimethylformamide (DMF) and formic acid.[32] In contrast to the MOF-808 synthesis employing stoichiometric amounts of linker ($ZrOCl_2$/BTC = 1/1),[31] MOF-808-P is synthesized with an excess of Zr-source ($ZrOCl_2$/BTC = 3/1), resulting in formic acid ligand deficiency and an increased number of Lewis acid sites at the under-coordinated Zr-metal. Characterization via powder X-ray diffraction (XRD, see supporting Figure S1), scanning electron microscopy (SEM, see supporting Figure S2) and thermogravimetric analysis (TGA, see supporting Figure S3) confirms that the correct structure is formed and that it crystallizes in octahedral microcrystals. Prior to the catalytic test, the metal-organic framework (MOF) is activated at 150 °C overnight to remove residual solvent molecules; at this temperature, activation under vacuum or in a regular oven had no effect on the resulting powder XRD nor on the catalytic activity.

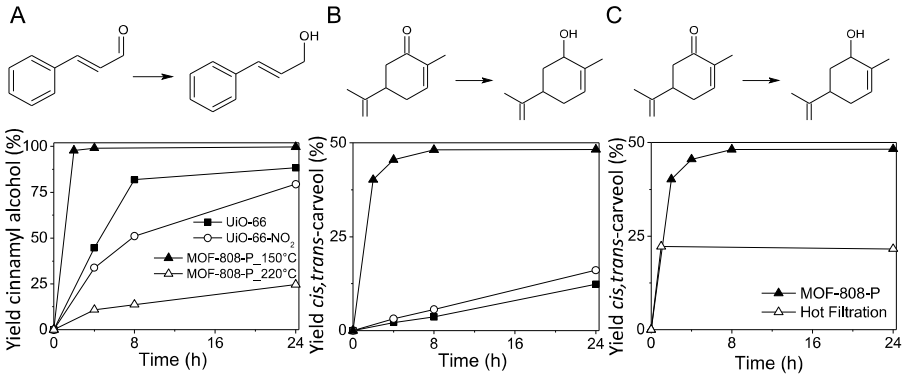

Figure 2 Meerwein-Ponndorf-Verley reduction of **A)** *trans*-cinnamaldehyde and **B**) *R*-carvone in isopropyl alcohol, catalysed by Zr-based MOFs UiO-66-x and MOF-808-P activated at different temperatures: 150 °C (▲) and 220 °C (∆). **C**) Hot filtration of the catalyst to confirm that the catalysis is truly heterogeneous. (120 °C, Zr/Substrate/IPA = 1/13/480, 250 rpm).

Meerwein–Ponndorf–Verley (MPV) reductions were carried out at 120 °C with isopropyl alcohol (IPA) as hydrogen donor and as solvent to move the equilibrium towards the desired allylic alcohol products. Catalytic activity of MOF-808-P is compared to UiO-66 and UiO-66-NO_2 by keeping the Zr/substrate ratio constant (Zr wt% is based on inductively coupled plasma–atomic emission spectra (ICP–AES) measurements and theoretical structure calculations; see supporting information

and Table S1). Figure 2 shows that MOF-808-P is an excellent MPV catalyst with both high *trans*-cinnamaldehyde conversion (>99 %) and high *trans*-cinnamyl alcohol selectivity (>99 %). Not only the yield is higher compared to the UiO-66 materials; the reaction rate is considerably increased: after only 2 h, complete conversion with high selectivity is obtained. The outstanding catalytic performance of MOF-808-P is even more clearly visible in the MPV reduction of *R*-carvone in Figure 2B. After 2 h, the *cis,trans*-carveol yield is 20-fold higher than the yield obtained with UiO-66 and UiO-66-NO_2 at the same time in the same reaction conditions. Even after reaction for 24 h, the UiO-66 materials only reach half of the MOF-808-P yield after 2 h. The increased activity of MOF-808-P can be partly attributed to the larger pores, enhancing the accessibility of under-coordinated Zr-atoms and facilitating the formation of the six-membered transition state, but more importantly to the Lewis acid sites on the under-coordinated Zr-atoms. Similar to mechanisms reported in literature,[1,3,33] a metal-alkoxide bond is formed with an isopropyl alcohol molecule while the substrate carbonyl-group is simultaneously activated via similar coordination to a Zr-atom. Both C-O bonds in hydride donor and acceptor are in close proximity, and hydride transfer occurs via a six-membered transition state while maintaining stereochemistry. Probing of the Lewis acid sites via sorption with deuterated acetonitrile (CD_3CN) (Figure S4) indicated a larger ratio of chemisorbed molecules on Lewis acid sites to physisorbed molecules (vibration frequency at 2297 cm^{-1} and 2265 cm^{-1}, respectively) for MOF-808-P compared to UiO-66 after activation at 150 °C. Furthermore, a large fraction of the CD_3CN molecules on the Lewis acid sites of MOF-808-P stay chemisorbed upon desorption under vacuum by increasing temperature to 150 °C, indicating a high acid strength.

It has often been observed that traces of DMF can be strongly adsorbed in the MOF structure, especially for MOF-808-P, since the missing formate ligand is most likely replaced by a DMF or water molecule.[32] ICP-AES indicates a Zr weight percentage of 39.4 +/− 0.7 wt %, a little lower than the theoretical 40 wt % when all missing linkers would be replaced by water. To investigate if some residual DMF molecules might still be adsorbed in the MOF on the catalytically active sites as suggested by thermogravimetric analysis, the activation temperature was increased from 150 °C to 220 °C under vacuum overnight. The elevated activation temperature clearly has a detrimental impact on the catalytic performance, as is shown in Figure 2A. Powder X-ray diffraction of MOF-808-P after activation at 220 °C indicates structure breakdown of the material after this activation step. Further experiments reported in this work were therefore always obtained with MOF-808-P catalyst activated at 150 °C.

Leaching of Zr into the solution was investigated by hot filtration of the reaction mixture after 1 h to remove the catalyst. Filtrate conversion did not increase after 24

h, indicating that there is no leaching of catalytically-active Zr into the solution, and the catalysis is truly heterogeneous (Figure 2C). The stability of MOF-808-P was retained upon activation and during the course of the reaction, as indicated by powder X-ray diffraction (XRD) of recycled catalyst (supporting Figure S1). This recycled catalyst is collected via centrifugation after reaction and washed with ethanol and IPA four times, after which it was activated first at 60 °C and overnight at 150 °C. Although hot filtration and powder XRD indicate there is no leaching nor perceptible structure breakdown, activity with the recycled catalyst drops by about 25% in the reduction of both cinnamaldehyde and carvone.

5.3.2 Increase equilibrium carveol yield

In view of the remarkably short reaction time to reach the equilibrium point in the *R*-carvone reduction, this specific reaction is further investigated to increase the yield. As mentioned before, Meerwein–Ponndorf–Verley (MPV) reduction is an equilibrium reaction with the reverse reaction called Oppenauer oxidation. The Meerwein–Ponndorf–Verley–Oppenauer (MPVO) redox equilibrium is determined by the oxidation potentials of both carbonyl–alcohol pairs. Aside from using isopropyl alcohol as the solvent, two other strategies can be used to shift the equilibrium towards the desired products: (1) distilling off acetone and (2) the use of stronger reducing alcohols. The results of both strategies are shown in Figure 3.

5.3.2.1 Evaporation of acetone

In the first strategy, two reactions are carried out simultaneously; one reaction is stopped after 2 h and both the solvent isopropyl alcohol and the formed acetone are removed by rotary vacuum evaporation. After the addition of fresh isopropyl alcohol, carveol yield reaches 70% (Figure 3A). This is 20% higher than without intermediate removal of acetone and clearly points out the importance of the reverse reaction, which limits the maximum carveol yield. Based on these results, the reaction was performed under reflux. 20 mg of activated MOF-808-P together with IPA, internal standard, and carvone were placed in a 50 mL two-mounted flask connected to a condenser. The reaction mixture was refluxed at 80 °C and stirred at 250 rpm, while a N_2-flow was passed over the mixture to remove the formed acetone. The obtained yield after 4 h was comparable to the yield of the rotary evaporated sample (see supporting Figure S5). After 6 h, even 74% yield could be obtained; however, loss of isopropyl alcohol was also significant at that time, so the reaction could no longer proceed.

5.3.2.2 1-indanol as reducing agent

Also with the second strategy, the use of a stronger reducing alcohol,[7,24] the yield could be vastly increased to 73 % (Figure 3B) with a diastereomeric excess (d. e.) for *cis*-carveol of 90 % (see supporting information and Figure S6). This reaction was

carried out with 12 equivalents of (*S*)-1-indanol in toluene as solvent. The reaction with 12 equivalents of isopropyl alcohol in toluene is also given as comparison in Figure 3B.

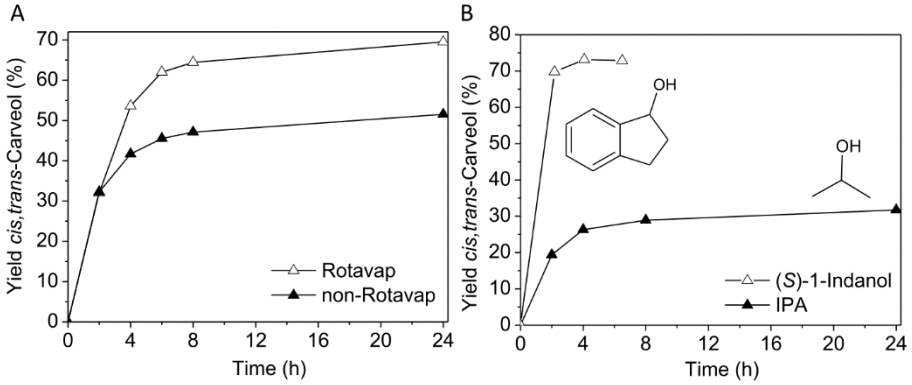

Figure 3 **A**) Evaporation of acetone and isopropyl alcohol (IPA) and addition of fresh IPA solvent (Δ) direct the equilibrium towards a *cis,trans*-carveol yield of 70 % (120 °C, Zr/Substrate/IPA = 1/13/480) **B**) MPV reduction with 12 equivalents of strongly reducing (*S*)-1-indanol drives the equilibrium towards a *cis,trans*-carveol yield of 73 %. (120 °C, Zr/substrate/reducing agent/toluene = 1/13/156/480).

5.3.3 **Substrate scope**

Given the excellent catalytic performance of MOF-808-P both with *trans*-cinnamaldehyde and *R*-carvone, a series of other α,β-unsaturated aldehydes and ketones were tested. Figure 4 shows that for the unsaturated aldehyde citral, high yields (>90%) are also obtained within a short time with high selectivity (>98%). Furthermore, Figure 4 shows that for the α,β-unsaturated ketones tested, complete conversion is not reached; instead, an equilibrium is established. This equilibrium is influenced by the redox potentials of the specific alcohol/ketone couples. We used isopropyl alcohol (IPA) as hydrogen donor and as solvent to shift the equilibrium towards the allylic alcohol product, but the oxidation potential of these compounds is too low compared to that of the acetone/IPA couple to allow complete conversion, as the reverse Oppenauer oxidation reaction takes place.[6] From the moment equilibrium is reached, selectivity starts to decrease due to the slow competing reactions that continue to progress. Selectivity in favour of the allylic alcohol is high in all reactions, only in the case of 4,4-dimethyl-2-cyclohexen-1-one, the saturated alcohol and etherification of the allylic alcohol with IPA are formed in significant amounts.

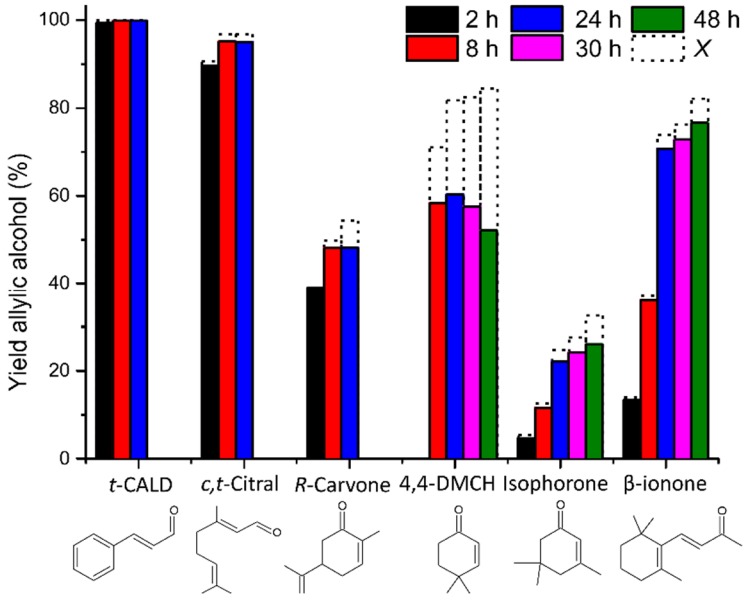

Figure 4 Meerwein–Ponndorf–Verley (MPV) reduction of α,β-unsaturated carbonyl compounds catalysed by MOF-808-P (120 °C, Zr/Substrate/IPA = 1/13/480, 250 rpm). Different colours indicate sampling at different reaction times; dotted bars represent conversion at the corresponding time (*X*).

5.4 DISCUSSION

From the broad substrate scope shown in Figure 4, it can be concluded that the cages and channels in MOF-808-P are sufficiently large to allow chemoselective transfer hydrogenation of bulky molecules like β-ionone, with a yield of 77 %. Aside from steric effects, electronic effects are also known to have an impact on the reactivity.[6,7] Electron donating substituents (such as methyl groups) increase the electron density of the carbonyl group, thereby reducing the hydrogen transfer, especially when present in the β-position of the carbonyl group. This explains the relatively low yields for isophorone. Table 1 compares the allylic alcohol yields obtained with MOF-808-P, with the highest yields reported in literature for comparable catalyst systems. Compared to Zr-zeolite Beta, that uses 1.3 mol % Zr to reach full conversion after 3 h, MOF-808-P obtained full cinnamaldehyde conversion within 2 h by using 7.7 mol % Zr (entry 1). For citral excellent allylic alcohol yield is also obtained within 4 h, in contrast to the Zr-PhyA reported MPV catalyst that required 6 h to obtain 88 % yield with a higher Zr mol% (150 %) (entry 2). The reported yield for carvone and isophorone is higher than the one obtained with MOF-808-P in our reaction system (entries 3 and 5); however, the reactant used in these studies (1-indanol) is more strongly reducing than the isopropyl alcohol used in this work. As mentioned above,

the obtained carveol yield with 1-indanol and MOF-808-P surpasses the best reported values (Table 1, entry 3). For comparison, a homogeneous Zr-catalyst—Zr(IV) acetyl acetonate ($Zr(acac)_4$; obtained from ABCR, AB122355)—was also tested under the same reaction conditions as MOF-808-P in isopropyl alcohol with the same Zr-to-substrate ratio. After 2 h at 120 °C, very little conversion was measured; after 24 h, however, 62 % of the initial cinnamaldehyde was converted with 96% selectivity in favour of cinnamyl alcohol. This obtained cinnamyl alcohol yield with the homogeneous Zr-catalysts is still 1.6 times lower than for MOF-808-P, while reaction time was 12 times longer. The same activity trend is observed in the MPV reduction of carvone; after 24 h at 120 °C, conversion reaches only 7 % with $Zr(acac)_4$. These experiments indicate heterogenization of Zr in the form of a porous catalytically-active material is not only beneficial for its recyclability, but also for its activity.

Table 1 Comparison of MOF-808-P obtained allylic alcohol yields with literature.

Entry	Substrate		*t* (h)	*Y* [1] (%)	*S* [1] (%)	Literature [2]		
						Conditions	Catalyst	Ref.
1	*trans*-cinnamaldehyde	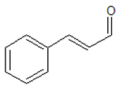	2	99	99	96% 3 h, IPA	Zr-zeolite β 1.3 mol % Zr	[19]
2	*cis*,*trans*-citral	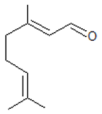	4	95	98	88% 6 h, IPA	Zr-PhyA 150 mol % Zr	[15]
3	*R*-carvone	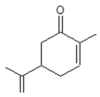	8	48	97	62% 5 h, 1-indanol	Zr-MCM-41 5 mol % Zr	[7]
4	4,4-dimethyl-2-cyclohexen-1-one	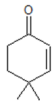	24	60	85	-	-	-
5	isophorone	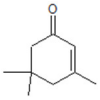	48	24	75	40% 24 h, 1-indanol	Hf-MCM-41 5 mol % Hf	[24]
6	β-ionone	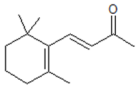	48	77	89	77% 9 h, IPA	B-MCM-41 4 mol % B	[23]

[1] Yield and selectivity are given for allylic alcohol (120 °C, Zr/Substrate/IPA = 1/13/480, 250 rpm, 20 mg catalyst); [2] Allylic alcohol yield, time, reducing agent, catalyst, and metal mol % for the given references

5.5 CONCLUSION

The Zr-based MOF-808-P was successfully used as a Meerwein–Ponndorf–Verley reduction catalyst for various α,β-unsaturated aldehydes and ketones. For typical substrates such as *trans*-cinnamaldehyde and *cis,trans*-citral, yields of respectively 99 % and 95 % were obtained within a short reaction time. Because of the increased number and strength of Lewis acid sites on coordinatively unsaturated Zr-atoms, the *cis,trans*-carveol yield increased 20-fold compared to reactions using another Zr-based MOF, UiO-66. For more challenging substrates, the equilibrium and reverse reduction of acetone prevented complete conversion. Two strategies were successfully used to shift the equilibrium towards the desired allylic alcohol products: evaporation of formed acetone and the use of the more strongly reducing 1-indanol increased the *cis,trans*-carveol yield from 50 % to more than 70 %.

5.6 REFERENCES

(1) Sheldon, R. A.; van Bekkum, H. *Fine Chemicals through Heterogeneous Catalysis*; WILEY-VCH: Weinheim, Germany, 2001; Chapter 8.
(2) Chuah, G. K.; Jaenicke, S.; Zhu, Y. Z.; Liu, S. H. *Curr. Org. Chem.* **2006**, *10*, 1639–1654.
(3) Liu, S. H.; Jaenicke, S.; Chuah, G. K. *J. Catal.* **2002**, *206* (2), 321–330.
(4) Gladiali, S.; Alberico, E. *Chem. Soc. Rev.* **2006**, *35* (3), 226–236.
(5) Boronat, M.; Corma, A.; Renz, M. *J. Phys. Chem. B* **2006**, *110*, 21168–21174.
(6) Noyori, R.; Hashiguchi, S. *Acc. Chem. Res.* **1997**, *30* (2), 97–102.
(7) De bruyn, M.; De Vos, D. E.; Jacobs, P. A. *Adv. Synth. Catal.* **2002**, *344* (10), 1120–1125.
(8) Wilds, A. L. *Org. React.* **1944**, *2*, 178–223.
(9) McNerney, B.; Whittlesey, B.; Cordes, D. B.; Krempner, C. *Chem. - A Eur. J.* **2014**, *20* (46), 14959–14964.
(10) Nandi, P.; Solovyov, A.; Okrut, A.; Katz, A. *ACS Catal.* **2014**, *4*, 2492–2495.
(11) Nandi, P.; Matvieiev, Y. I.; Boyko, V. I.; Durkin, K. a.; Kalchenko, V. I.; Katz, A. *J. Catal.* **2011**, *284* (1), 42–49.
(12) Zhu, Y.; Liu, S.; Jaenicke, S.; Chuah, G. *Catal. Today* **2004**, *97* (4), 249–255.
(13) Ramanathan, A.; Castro Villalobos, M. C.; Kwakernaak, C.; Telalovic, S.; Hanefeld, U. *Chem. - A Eur. J.* **2008**, *14* (3), 961–972.
(14) Vermoortele, F.; Bueken, B.; Le Bars, G.; Van de Voorde, B.; Vandichel, M.; Houthoofd, K.; Vimont, A.; Daturi, M.; Waroquier, M.; Van Speybroeck, V.; Kirschhock, C.; De Vos, D. E. *J. Am. Chem. Soc.* **2013**, *135*, 11465–11468.
(15) Song, J.; Zhou, B.; Zhou, H.; Wu, L.; Meng, Q.; Liu, Z.; Han, B. *Angew. Chemie (International Ed.* **2015**, *54*, 9399–9403.
(16) Ivanov, V. A.; Bachelier, J.; Audry, F.; Lavalley, J. C. *J. Mol. Catal.* **1994**, *91* (94), 45–59.
(17) Battilocchio, C.; Hawkins, J. M.; Ley, S. V. *Org. Lett.* **2013**, *15*, 2278–2281.
(18) Zhu, Y.; Jaenicke, S.; Chuah, G. K. *J. Catal.* **2003**, *218* (2), 396–404.
(19) Zhu, Y.; Chuah, G.; Jaenicke, S. *J. Catal.* **2006**, *241* (1), 25–33.
(20) Iglesias, J.; Melero, J. A.; Morales, G.; Moreno, J.; Segura, Y.; Paniagua, M.; Cambra, A.; Hernández, B. *Catalysts* **2015**, *5* (4), 1911–1927.
(21) Wang, J.; Okumura, K.; Jaenicke, S.; Chuah, G.-K. *Appl. Catal. A Gen.* **2015**, *493*, 112–120.
(22) Yuan, Y.; Yao, S.; Wang, M.; Lou, S.; Yan, N. *Curr. Org. Chem.* **2013**, *17*, 400–413.
(23) Uysal, B.; Oksal, B. S. *Appl. Catal. A Gen.* **2012**, *435-436*, 204–216.
(24) De bruyn, M.; Limbourg, M.; Denayer, J.; Baron, G. V.; Parvulescu, V.; Grobet, P. J.; De Vos, D. E.; Jacobs, P. A. *Appl. Catal. A Gen.* **2003**, *254* (2), 189–201.
(25) Gascon, J.; Corma, A.; Kapteijn, F.; Llabre, F. X. *ACS Catal.* **2014**, *4*, 361–378.
(26) Dhakshinamoorthy, A.; Opanasenko, M.; Čejka, J.; Garcia, H. *Catal. Sci. Technol.* **2013**, *3* (10), 2509.
(27) Dhakshinamoorthy, A.; Asiri, A. M.; Garcia, H. *Chem. Commun.* **2014**, *50*, 12800–12814.
(28) Plessers, E.; De Vos, D. E.; Roeffaers, M. B. J. *J. Catal.* **2016**, *340*, 136–143.
(29) Cirujano, F. G.; Corma, a.; Llabrés i Xamena, F. X. *Chem. Eng. Sci.* **2015**, *124*, 52–60.
(30) Valenzano, L.; Civalleri, B.; Chavan, S.; Bordiga, S.; Nilsen, M. H.; Jakobsen, S.; Lillerud, K. P.; Lamberti, C. *Chem. Mater.* **2011**, *23*, 1700–1718.
(31) Furukawa, H.; Gándara, F.; Zhang, Y.; Jiang, J.; Queen, W. L.; Hudson, M. R.; Yaghi, O. M. *J. Am. Chem. Soc.* **2014**, *136*, 4369–4381.
(32) Jiang, J.; Gándara, F.; Zhang, Y.; Na, K.; Yaghi, O. M. *J. Am. Chem. Soc.* **2014**, *136*, 12844–12847.
(33) Creyghton, E. J.; Ganeshie, S. D.; Downing, R. S.; van Bekkum, H. *J. Mol. Catal. A Chem.* **1997**, *115*, 457–472.

CHAPTER 6

CONCLUSION & PERSPECTIVES

CHAPTER 6

6.1 CONCLUSION AND PERSPECTIVES

Allylic alcohols and functionalized anilines are industrially important flavouring and fragrance compounds and valuable intermediates for pharmaceuticals, polymers and other fine chemicals. Industrially, they are mostly synthesized via chemoselective catalytic hydrogenation of unsaturated aldehydes and nitro-compounds. This hydrogenation can be catalysed by supported metal nanoparticles. The size, shape and distribution of the nanoparticles together with the accessibility and the support determine the outcome of the catalytic process and hence the reaction products. High selectivity towards the unsaturated alcohol and amine products is governed by the coordination of the substrates to the catalytic site, activating the carbonyl or nitro-group for reduction, leaving the C=C double bound untouched. However, besides the substrates, also hydrogen needs to adsorb on the nanoparticles before reduction can take place. Silver has a completely filled d-shell, preventing the dissociative adsorption of hydrogen and furthermore the hydrogen binding energy of silver is very low, suggesting silver is not a good hydrogenation catalyst. However, when small silver nanoparticles are formed, the electron density shifts from the 4d to the 5s orbital, making H_2 dissociation possible on silver.[1] Furthermore, coordinatively unsaturated (CUS) silver sites were found to be crucial for the H_2 dissociation and since smaller particles possess relatively more of these CUS sites, decreasing nanoparticle size was reported to be beneficial for the activity in the nitrostyrene hydrogenation.[2] To prevent aggregation of these small silver nanoparticles, they are typically supported on mesoporous alumina and silica supports.

In this work, metal organic frameworks (MOFs) were explored as alternative support for silver nanoparticles. Size restriction via pore confinement and stabilisation in the metal-organic framework was aimed. A wide range of different MOFs were tested with metal clusters ranging from Fe over Ti to Zr and using different linker sizes and functionalities. The widely used Zr-terephthalate based UiO-66 proved to be the most successful in silver nanoparticle generation, stabilisation and chemoselective hydrogenation. Silver nanoparticles were successfully supported on UiO-66 via infiltration and reduction in EtOH. This catalyst reached full cinnamaldehyde conversion with comparable selectivities to those reported in literature for other supported silver catalysts. Furthermore, this catalyst was recyclable and hence stable at the high temperature (140 °C) and pressure (50 bar of H_2) conditions

typically used in such hydrogenation reactions. Although a new nanoparticle silver catalyst was developed, further exploration of this catalyst was not pursued because the conversion was lower than the best catalysts reported in literature.

Clear-structure activity relationships could not be established because of practical difficulties such as the limited characterisation of the precise nanoparticle size and dispersion inside the MOF-granules. UV/Visible diffuse reflectance spectroscopic (DRS) characterisation of the UiO-66 supported silver nanoparticles indicates their size is smaller than 10 nm, however more precise determination with this technique is not possible at these small size ranges. Size determination based on line-broadening in X-ray diffraction also faces a lower size limit in the few nanoparticle range. Furthermore, determining the nanoparticle size on the XRD-setup in our lab was not possible because of the low detector sensitivity and the limited specification of the intrinsic line-broadening due to the X-ray source of the machine itself. As mentioned in the introduction, chemisorption is another widely applied technique to determine the silver nanoparticle size if the chemisorption stoichiometry is known, however the use of H_2 was not possible in our lab. The size obtained with chemisorption techniques also yields an approximate average value, particularly in the case of silver in which subsurface oxygen chemisorption and bulk oxidation may occur at higher oxygen coverages. Transmission electron microscopy (TEM) of metal clusters in MOFs is very difficult, because of the easy destruction of the MOF structure by the TEM electron beam. This local structural breakdown and the resulting metal aggregation happen so quickly (within a few seconds to one minute) that it is difficult if not impossible to get information on the original clusters.

Surprisingly, the pure UiO-66 support without silver reached an even higher cinnamyl alcohol yield in the solvent isopropyl alcohol (IPA) even in the absence of H_2. The Lewis acid zirconium sites of the MOF catalysed the transfer hydrogenation of cinnamaldehyde with IPA. Based on the high activity and selectivity, the substrate scope was further extended to other carbonyl compounds. Because of the lower reaction temperature and no need for hydrogen pressures, reaction could be performed in simple glass vials in contrast to reactors, this also tremendously facilitates further catalytic implementation.

One of the most interesting features of metal-organic frameworks is the large variability in building blocks that can be used to obtain the desired material properties. For catalysis purposes molecular diffusion can be increased by employing larger linker molecules, resulting in larger pores. Another strategy to alter the cluster connectivity is by the use of tridentate linkers; in the case of the $Zr_6O_4OH_4$ cluster found in UiO-66 the use of a benzenetricarboxylate (BTC) instead of benzenedicarboxylate (BDC) linker increases the pore diameter from 7-8 Å to 18 Å and decreased the coordination from 12 to 6 linkers and 6 formate ligands. After

synthesis optimization of this MOF, called MOF-808-P, only 5 formate ligands are coordinated to the zirconium cluster increasing the number and strength of Lewis acid sites.[3,4] The further improved activity of MOF-808-P over UiO-66 in the MPV reduction of all the substrates tested, indicates that larger pores clearly decrease diffusion limitations and more importantly, the increased Lewis acidity leads to 20-fold increased catalytic activity. Even with less easy to reduce carbonyl compounds, transfer hydrogenation activity was found to be possible at high selectivities. The major drawback of these MOFs as MPV reduction catalysts however, is their recyclability. Visual coloration of both UiO-66 and MOF-808-P materials from white to light yellow after reaction and washing might indicate the presence of some remaining reaction or side-products that poison the catalytic sites. Another explanation of the lack of recyclability can be the structure breakdown and the loss of linker molecules during reaction and washing. This linker loss might make the Zr-sites more accessible and more prone for poisoning and might also lead to leaching of zirconium. Before MOFs can thus be actually used as MPV catalysts, recyclability must be improved. New MOF-structures are reported frequently, but their stability under catalytic reaction conditions and regeneration of the catalytic active sites upon recycling must be more thoroughly studied before they can become real alternatives to conventional solid catalysts.

Besides developing new chemoselective reduction catalysts, this work also focussed on the rational improvement of supported silver catalysts preparation. In heterogeneous catalysis research, bulk catalytic hydrogenation testing is typically combined with nanoscale size characterisation and bulk crystal structure and loading determination. During synthesis of the commonly used silver nanoparticle on silica catalyst however, a severe colour heterogeneity at the support granule scale was revealed via optical transmission microscopy. A novel correlative imaging approach was developed to relate optical appearance of the silver on silica granules to silver loading and silver nanoparticle size on the support granule outer surface. Furthermore, the optical appearance was correlated with catalytic performance via single particle catalytic measurements in bulk reaction conditions. These single particle measurements revealed an optimal silver loading and confirmed that the interparticle heterogeneity has a large impact on the catalytic performance. Sorting of the granules with the optimal optical appearance increased the bulk catalytic performance, confirming the validity of the single particle measurements and the importance of not ignoring this heterogeneity. The impact of heterogeneity on catalytic performance is potentially even more pronounced when focussed on selectivity instead of activity. In contrast to the silver catalysed hydrogenation of 4-nitrostyrene that yielded almost exclusively 4-vinylaniline, hydrogenation of cinnamaldehyde with this silver on silica reference catalyst formed both C=O and

C=C hydrogenation products with a 75:25 ratio. Due to the lower activity and thus longer reaction time and more extreme reaction conditions, single particle catalysis experiments to reveal the impact of heterogeneity on selectivity need further optimisation.

From detailed examination of the origin of the heterogeneity in silver loading between individual silica granules, the static drying step was found to have the largest contribution. Optimisation of the drying procedure to fluidized bed drying resulted in an almost homogeneous catalyst batch. The large fraction of transparent granules in this catalyst batch indicates that almost all silver nanoparticles are pore confined 6 nm sized nanoparticles. Interestingly, this adaptation to the drying step of the incipient wetness impregnation procedure can be easily implemented at the laboratory scale, is scalable and does not require the use of expensive solvents, metal precursors or experimental conditions such as vacuum or freeze drying. However, determination of single particle silver loading and size and distribution of the silver nanoparticles, both at the outer surface and inside the granules is still necessary as follow up work. This will require additional characterisation techniques like energy- dispersive X-ray spectroscopy (EDX), scanning electron microscopy (SEM) and transmission electron microscopy (TEM) combined with 3D-reconstruction or sectioning.

Furthermore, it should be noted that the observed heterogeneity is not limited to the Ag/SiO_2 catalyst under study in this work. Pt-loading heterogeneities were reported in zeolite Y particles[5] and Pt-impregnation on silica yielded a similar colour heterogeneity at the granule scale. Bulk experiments of the Pt/SiO_2 catalysed 4-nitrostyrene reduction resulted in the saturated ethylnitrobenzene as major hydrogenation product in contrast to 4-vinylaniline with Ag/SiO_2. These experiments highlight the importance of the used element for the resulting chemoselectivity and the intrinsic selectivity of silver to obtain 4-vinylaniline, which is not straightforward with Pt. The higher activity of Pt on the contrary, is beneficial for the single particle experiments since it allows reaction at room temperature and low pressure, thereby tremendously facilitating single particle and fluorescent microscopic investigation. Preliminary single particle experiments to probe if activity and selectivity of these silica supported Pt-catalysts are related to their colour, hence Pt loading and/or size, did not result in a clear trend yet, but I believe further experiments will reveal a trend soon.

Although optical appearance and silver loading are correlated based on SEM-EDX measurements, EDX remains a surface technique that only probes the outer shell of the support granule up to a few micrometres below the surface. In case of an egg-shell type distribution of the nanoparticles in the support, this means an overestimation of the silver loading inside the particle, and the opposite for egg-yolk

catalysts. A solution to this problem that could be provided by dissolving the single particle catalysts after performing experiments, is the detection of Ag-ions via a colorimetric method using a probe molecule after complete dissolution of the silver nanoparticles. *p*-Dimethylaminobenzylidene Rhodanine (DMABR) is a probe molecule of which the colour changes due to Ag^{+}-complexation,[6] described in 1935 to quantitatively determine small amounts of silver. When $AgNO_3$ is added to a DMABR-solution in the expected nanomole range of a single Ag/SiO_2 particle, a clear decrease in absorption at 370 nm and increase in absorption at 480 nm is visible (Figure 1A-B). Preliminary experiments indicate this colorimetric method can be used to determine Ag-loading of individual particles after dissolving the metallic silver nanoparticles in concentrated nitric acid (Figure 1C).

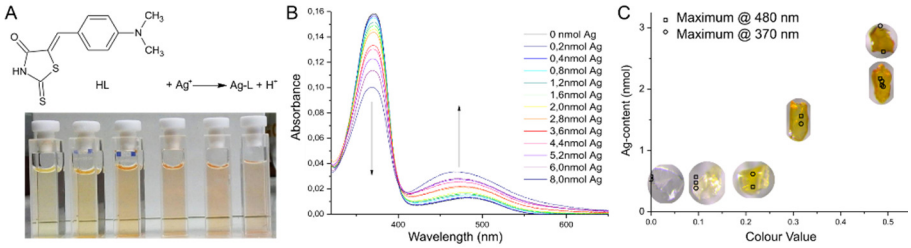

Figure 1 A,B) Colour change as a result of DMABR-Ag complexation, **C)** Single particle Al-loading determination.

The performed single particle catalytic experiments were very useful to determine the optimal optical appearance of the supported silver catalysts, these single time point, ex situ, experiments however provided no information about the evolution of the catalytic activity and selectivity or on the exact location of the reaction. Such measurements rely on fluorescent probes that during chemoselective hydrogenation undergo a change in coloration. In situ fluorescence microscopy is a powerful tool to answer these questions. Push-pull organic fluorophores consist of electron-donating and electron-withdrawing groups that are electronically connected via an extended π-conjugated system. Reduction or oxidation results in an electronic change of the system, which in turn may lead to a change in the light absorption and emission. These probes, used to study dehydrogenase and reductase enzymes, might thus be good candidates to study catalytic reduction reactions. Via carbonyl-reduction of the non-fluorescent molecule coumberone, a fluorescent alcohol product coumberol is formed,[7–9] similarly reduction of the nitro-group in nitro-DCDHF results in a fluorescent amine-product as analogue reactions for the chemoselective reduction of carbonyl and nitro-compounds (Figure 2).[10] By spatially resolved recording of these product signals, the formation in time and place can be followed for every specific catalyst granule. The location of the fluorescent product formation yields information about the role of the large silver particles on the outer

surface in the coloured granules and about the distribution of catalytic activity inside the granules. Furthermore, fluorescent microscopy would also give time resolved information on the evolution of catalytic activity to calculate the rate. Although these probe molecules were already successfully synthesized and transformed to their fluorescent products by Ag/SiO_2 hydrogenation on a bulk scale, single molecule fluorescent experiments were not successful yet. Further investigation on this topic will definitely be indispensable in understanding the impact of catalyst heterogeneity on the catalytic performance. Crucial in the success of such experiments will be related to the influence that the metal has on the fluorescence of the formed product. Metal nanoparticle catalysed oxidation and reduction by Chen and co-workers have proven that reliable observation of catalytic conversion on metals is possible.[11]

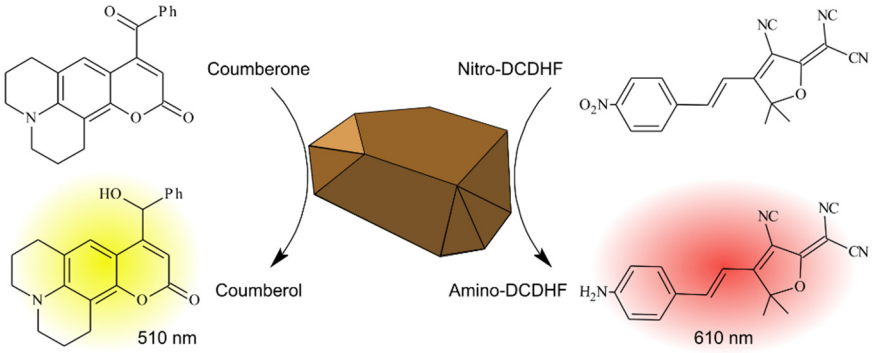

Figure 2 Conversion of non-fluorescent molecules to fluorescent products, emission maximum is indicated.

If fluorescence based observation of (individual) events near metal surfaces proves to be too challenging, Raman microscopy offers an alternative. Raman micro-spectroscopy is based on the inelastic scattering of light. Energy exchange between the scattered photon and the sample results in an energy/frequency shift. Adsorption of probe molecules at catalytic sites changes the Raman spectrum, enabling characterization of the catalyst and even localisation of the catalytic sites. Furthermore, since every molecule has its own characteristic spectrum that serves as a fingerprint, the catalytic conversion of organic molecules can be followed in space and time. Although single molecule detection is not possible, still sufficiently spatial and temporal resolved information can be observed regarding location and rate of the catalytic process at the support granule level. In contrast to fluorescence microscopy, Raman based measurements do not rely on specific probe molecules that mimic the catalytic reaction. Care should be taken when imaging silver nanoparticle catalysts with Raman, because they might influence the Raman biasing the Raman signal e. g. by enhancing the weak Raman scattering signal via surface

enhanced Raman scattering (SERS).[12] Also metal nanoparticle luminescence together with the weak Raman signals form a major limitation of Raman microscopy, however two elegant non-linear optical microscopy techniques are available that can potentially to circumvent these limitations: coherent anti-Stokes Raman scattering (CARS) and stimulated Raman scattering (SRS).[13] These two innovative techniques are accessible and home-built in our lab, so can be used to study catalyst heterogeneities and their impact on the catalytic performance. Also in spontaneous Raman scattering the use of UV yields enhanced Raman signals often avoiding the detrimental influence of metal and substrate luminescence.

As major synthesis route for allylic alcohols and functionalized anilines chemoselective reductions are an important research area. More and more heterogeneous instead of homogeneous MPV catalysts are being reported with high activity and selectivity, favouring the implementation in industrial synthesis. Implementation using alcohols from renewable sources or waste streams to reduce the substrates instead of using hydrogen, makes such a route even more attractive. Alternatively, research into chemoselective reduction via high pressure hydrogen reduction focusses on the development of improved supported metal catalysts by controlling nanoparticle size, distribution and intrinsic metal properties. The work presented in this PhD as well as recent reports on various catalysts have demonstrated particle to particle variations in material properties and the impact thereof on the catalytic process. Catalysis research in general will benefit if bulk and microscopic characterisation and catalyst testing in future will be executed keeping this into consideration.

6.2 REFERENCES

(1) Sa, J.; Srebowata, A. *Hydrogenation with Low-Cost Transition Metals*; CRC Press: Boca Raton, 2016.
(2) Shimizu, K.; Miyamoto, Y.; Satsuma, A. *J. Catal.* **2010**, *270* (1), 86–94.
(3) Furukawa, H.; Gándara, F.; Zhang, Y.; Jiang, J.; Queen, W. L.; Hudson, M. R.; Yaghi, O. M. *J. Am. Chem. Soc.* **2014**, *136*, 4369–4381.
(4) Jiang, J.; Gándara, F.; Zhang, Y.; Na, K.; Yaghi, O. M. *J. Am. Chem. Soc.* **2014**, *136*, 12844–12847.
(5) Zečević, J.; van der Eerden, A. M. J.; Friedrich, H.; de Jongh, P. E.; de Jong, K. P. *ACS Nano* **2013**, *7* (4), 3698–3705.
(6) Sandell, E. B.; Onishi, H. Wiley-Interscience: New York 1978, p 1085.
(7) Yee, D. J.; Balsanek, V.; Sames, D. *J. Am. Chem. Soc.* **2004**, *126* (8), 2282–2283.
(8) Halim, M.; Yee, D. J.; Sames, D. *J. Am. Chem. Soc.* **2008**, *130* (4), 14123–14128.
(9) Yee, D. J.; Balsanek, V.; Bauman, D. R.; Penning, T. M.; Sames, D. *Proc. Natl. Acad. Sci. U. S. A.* **2006**, *103* (36), 13304–13309.
(10) Lee, M.; Willimas, J.; Twieg, R.; Rao, J.; Moerner, W. E. *Chem. Sci.* **2013**, *4*, 220–225.
(11) Chen, P.; Zhou, X.; Shen, H.; Andoy, N. M.; Choudhary, E.; Han, K.-S.; Liu, G.; Meng, W. *Chem. Soc. Rev.* **2010**, *39* (12), 4560–4570.
(12) Laurier, K. G. M.; Poets, M.; Vermoortele, F.; De Cremer, G.; Martens, J. a; Ujl-i, H.; De Vos, D. E.; Hofkens, J.; Roeffaers, M. B. J. *Chem. Commun.* **2012**, *48* (10), 1559–1561.
(13) Zoubir, A. *Raman Imaging Techniques and Applications*; Springer: Berlin-Heidelberg, 2012.

APPENDICES

SUPPORTING INFORMATION TO CHAPTER 2

Determination of Red Colour Index

Step by step procedure used to calculate red colour index, steps 3-5 are displayed in Figure S1:

1) Colour images of several catalyst granules (20-40) at once were obtained via the eyepieces of an Olympus upright microscope using an adapter from Micro-Tech-Lab (Austria) to connect a Canon EOS5D colour camera.
2) Colour images are processed in ImageJ
3) Manual selection of particles was done via 'polygon selection'
4) Via the histogram of this selected area/particle, the mean 8-bit value in the red channel was determined. Theoretically values range from 0 for intense red particles to 255 for completely transparent particles.
5) Additionally, the mean 8-bit value of the surrounding background was measured. This value is obviously equal to or larger than the values obtained for the different particles, except for the very bright transparent ones.
6) The mean red channel value of the selected particle (see step 4) was divided by the mean value of the background (see step 5)
7) The obtained ratio (values between 0 and 1) is subtracted from 1. Hence we get an increasing index for increasing 'redness'

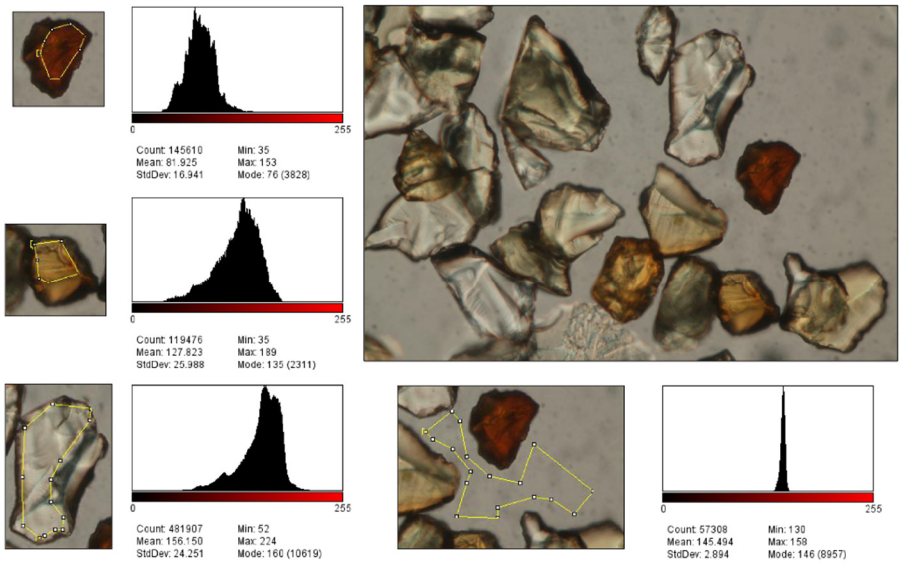

Figure S1. Illustration of steps 3-5 in the used procedure to calculate red colour index.

Nitrogen Physisorption

Nitrogen adsorption and desorption isotherms at 77 K were measured using a Micromeritics 3Flex 3500 physisorption instrument. The sample was degassed before measurement at 423 K for 6 h under vacuum (10^{-2} mbar). The pore size distribution was calculated using the BJH method (Harkins and Jura thickness curve and Faas correction, 3Flex 3.00 software).

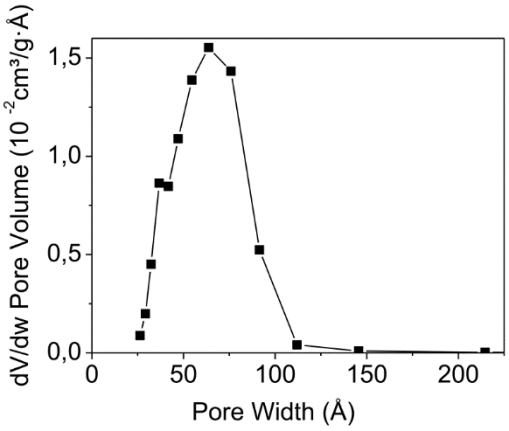

Figure S2. Pore size distribution of the used silica gel with an average pore width of 60 Å.

Physicochemical properties of Silica Gel (60752 Fluka, Sigma-Aldrich) from nitrogen physisorption measurements:
BET Surface Area = 408.6 m^2/g
BJH Desorption cumulative pore volume = 0.789 cm^3/g
BJH Desorption average pore width = 60 Å

High Resolution Scanning Electron Microscopy (HR-SEM)

On average 6 nm pore confined AgNPs are detected after crushing the sample (A), micrographs B-D were obtained without any modification of the sample in order to relate nanoparticle size on the granule's surface to its colour. On transparent granules with a red colour index in the range of 0-0.5 (e. g. Figure S3B) none or only a few 20-30 nm sized nanoparticles were present, markedly more of these 30-50 nm sized particles were detected on yellow granules with a red colour index in the range of 0.12-20 (Figure S3C,D). Schematic representation of Ag nanoparticle size distribution for three optically different granules is depicted in Figure S3E.

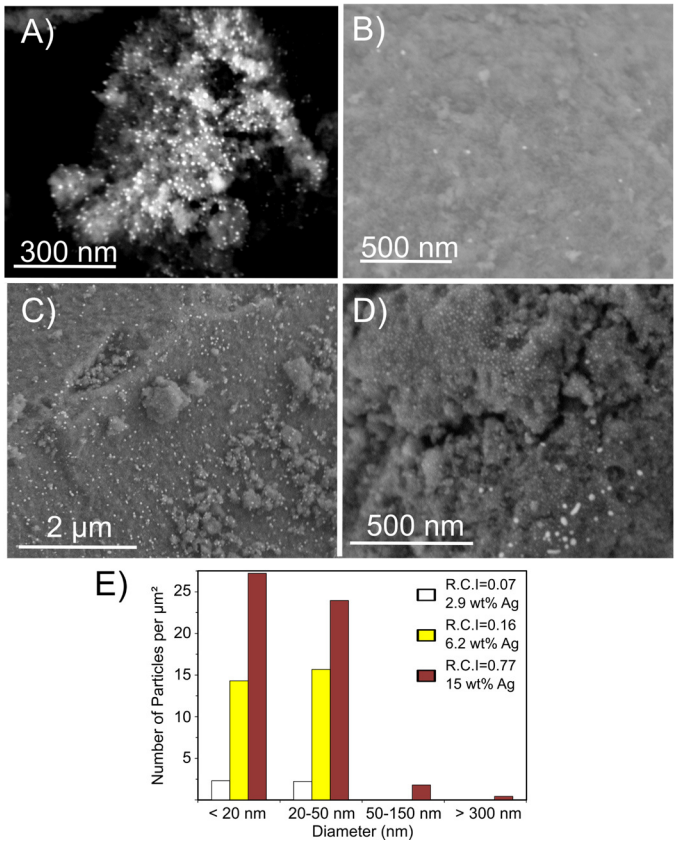

Figure S3. HR-SEM micrographs of **A)** self-synthesized and **B-D)** commercially obtained Ag/SiO_2 (white dots are Ag nanoparticles), **E)** Ag NP size distribution of the outer surface of three granules with a Red Colour Index (R.C.I.) of 0.07, 0.16 and 0.77 corresponding to respectively 2.9 wt%, 6.2 wt% and 15 wt% total silver loading per granule.

Focused ion beam (FIB) milling combined with SEM-EDX

Cross-section FIB slicing and milling combined with SEM and EDX were performed using an Scios Dual Beam system (FEI, The Netherlands). Before FIB cutting, a 2 µm protective Pt layer was applied to the crystal surface through ion-beam-assisted deposition (30 kV, 1 nA) to minimize the curtaining effect. Ga^+ ion beams of 30 kV/15 nA and 1 nA were used for trench milling and sample slicing respectively; slice thickness was 3 nm. Conventional SEM (1 kV, 13-25 pA, WD = 2.2 mm) was used to observe crystal morphology after FIB milling and slicing, combined with EDX analysis. Image acquisition was performed using the lower (T1) in-lens BSE detector and using NG Microscope User Interface software (FEI); further image analysis and processing were performed with AutoSlice And View software (FEI).

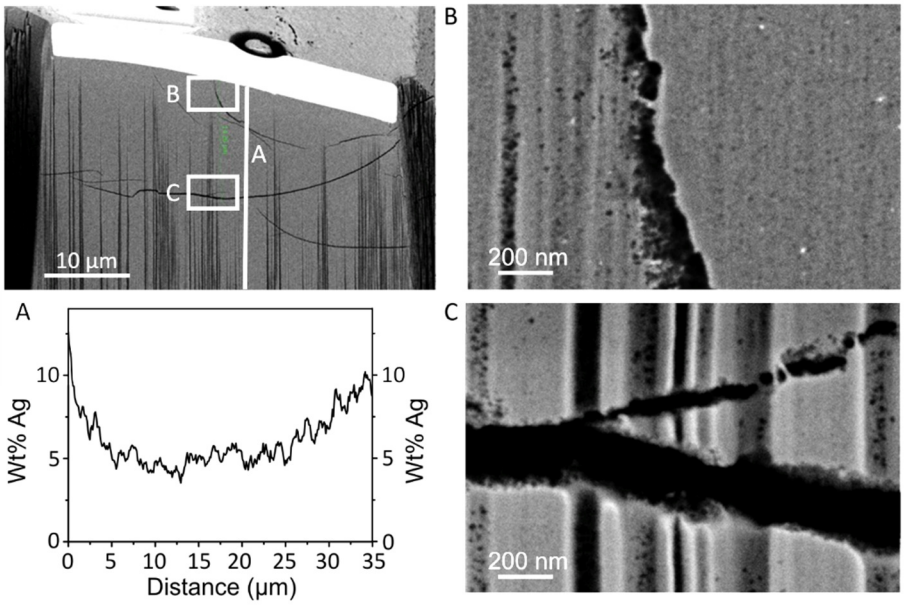

Figure S4. A) Weight percentage silver versus distance of a commercial Ag/SiO_2 particle, EDX analysis after FIB milling and slicing, location of the line scan is indicated on the overview picture; **B)** SEM micrograph of a sliced granule 1 µm below the surface, silver nanoparticles are visible (white dots); **C**) SEM micrograph of a sliced granule 14 µm below the surface, no silver nanoparticles visible.

Catalytic performance testing at the single support particle level

To test cross contamination of the 21 reaction wells via distillation of product or reagent from one well into another, solutions filled with 4-NSt (0.1 M), 4-VAn (0.1 M) and internal standard (tetradecane, 0.18M) in EtOH were placed in a reactor next to a pure EtOH solution, after 1h under 20 bar H_2 heated to 100 °C, no 4-NSt or 4-VAn was detected and only minute amounts of internal standard (< 2 μM).

Prior to the catalytic reaction, single support particles are carefully placed one by one in the different wells via a stereomicroscope (Leica M165FC). After this, the multiwell can be filled with the reaction solution using a micropipette and placed in the reactor. Since thermal hydrogenation of 4-nitrostyrene results in the formation of the unwanted 4-ethylnitrobenzene and little 4-vinylaniline, in each run several wells are not filled with a catalyst particle to account for this blank conversion and some wells are only filled with solvent to assure that no cross contamination has occurred. To lower solvent evaporation as much as possible the high boiling *N,N*-dimethylacetamide (DMA) was used as a solvent and hexadecane as internal standard for quantitative GC-analysis. Optimization of reaction conditions led to the use of 18 μL of a 33 mM 4-NSt solution in each microwell, performing hydrogenation under 20 bar H_2 heated to 110 °C for 2.5 h in a Parr reactor filled with 3 mL DMA. Analysis of the samples was carried out via gas chromatography after rinsing the wells two times with pure DMA.

The first optimization of the single particle catalytic hydrogenation was the use of high boiling DMA as solvent, since in experiments with EtOH as solvent, the microwells were emptied completely during reaction at 110 °C. Cross contamination of internal standard could be reduced significantly by replacing tetradecane with hexadecane. Figure S5 compares the initial volume and volume of DMA added to the reactor with the final volume that is found in the wells after reaction. When no additional DMA is added (entries 1-2), the solvent in the wells is evaporated completely and after cooling down condensed into the reactor; no catalytic activity is detected in these experiments. When the reactor is filled with DMA prior to the reaction, after reaction the wells still contain reaction solution and catalytic activity is detected (entries 3-7). However, when the wells are filled with 20 μL (entry 4), the surface of the multiwell is covered with liquid, indicating spill-over of one well into another because the used volume is too close to the maximum working volume of the wells (25 μL). When the volume in the wells was increased to 18 μL, and by adding 3 mL of DMA to the bottom of the reactor, no cross contamination was observed and sufficiently high 4-vinylaniline yields were obtained to perform single particle catalytic experiments.

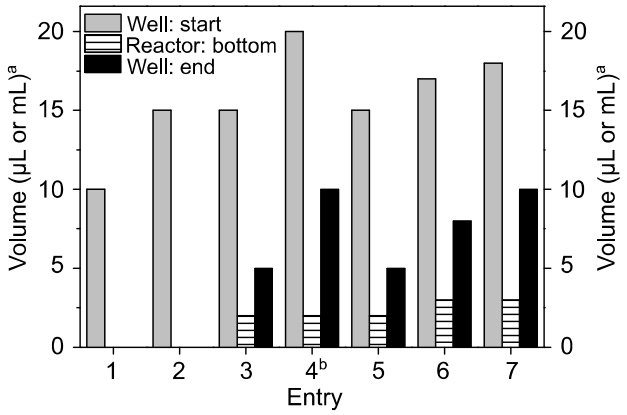

Figure S5. Optimization of the single particle catalytic experiments by varying volume in the well and addition of DMA to the reactor bottom prior to reaction. When additional DMA is used (entries 3-7), after reaction the wells still contain solution and catalytic activity is detected (except in entry 3: blank reaction). [a] Volume added to well: µL; reactor: mL [b] surface of the multiwell covered with liquid.

Figure S6 depicts the results for 47 individual silver supported silica particles, in Figure S6C 4-VAn yield is corrected for support granule size and normalized to the silver content. Calculation was done as follows: every reaction well contained one support granule of which the red colour index was determined according to the earlier described method. By including the size of the particle in combination with the silver loading determined by linking the red colour index to EDX and ICP data, the observed catalytic conversion in a specific well could be normalized on basis of the silver content of that specific supported silver catalyst granule. The red colour index–EDX relation was extensively studied and is shown in the main article in Figure 2. FIB-SEM however revealed that EDX data recorded solely from the first few micrometres below the outer surface resulted in an overestimation of Ag-loading as a consequence of a silver loading gradient. Therefore, ICP-AES measurements were performed. In order to allow correct determination of the catalyst sample's weight, a sufficient amount of sample was required. That is why we sorted the sample in different batches based on their optical colour (see Supporting Figure S8). These data allow to correct the silver content determined from EDX measurements to give a more accurate value.

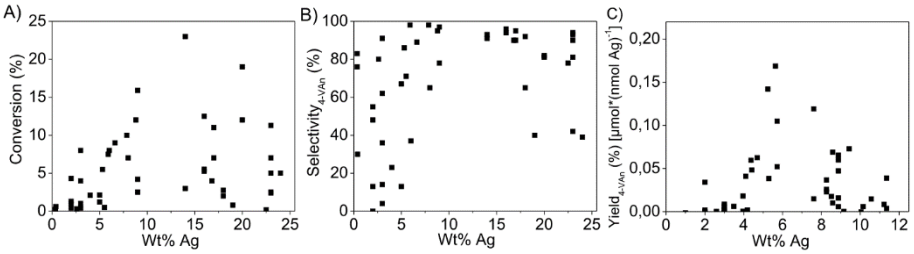

Figure S6. Single Particle experiment results (2.5 h, 20 bar H_2, 110 °C). A) Blank-corrected absolute conversion and **B)** 4-Vinylaniline (4-VAn) selectivity versus Ag-loading, based on SEM-EDX relation, **C)** Normalized 4-VAn yield versus silver loading for 47 individual silver supported silica granules, estimation of silver loading based on red colour index, SEM-EDX and ICP-AES measurements.

In addition some important notes on the validity of the test method: (1) there was no detectable amount of reagent or product in the wells filled only with solvent, nor in the reactor and (2) 4-vinylaniline yield in the blank reactions was consistent in the different between the different wells: 0,26±0,03 % (run 1); 0,18±0,07 % (run 2); 0,21±0,02 % (run 3); 0,23±0,04 % (run 4).

Specifications of microwell slide (Hamamatsu A10657-01):

Material	Slide glass	Soda-lime glass
	Cover glass	Borosilicate glass
Number of wells		21 (3*7)
Working volume		25 µL
Dimensions		38 mm x 25 mm x 3.4 mm
Well diameter		4 mm (top), 3 mm (bottom)
Well depth		3.1 mm

Calculation of Estimated Theoretical Normalized Yield

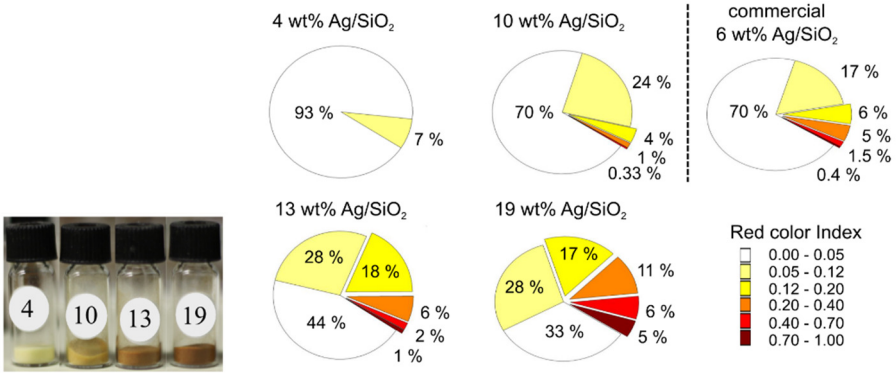

Figure S7. Optical microscopy study on catalyst powders. Interparticle heterogeneity (n = 250-600) illustrated with pie diagram, colors represent red colour index of individual Ag/SiO_2 granules.

The calculation of the estimated theoretical normalized yield for the commercial 6 wt% Ag/SiO_2 catalyst is given as an example:

1) Based on a granules' red colour index, it is classified in a specific red colour index subunit (Table S1, column A)

2) Every subunit corresponds to an average Ag loading (Table S1, column B)

3) Every subunit also corresponds to an average normalized 4-Vinylaniline (4-VAn) yield, obtained from the single particle catalysis experiments (Table S1, column C)

4) Optical microscopic analysis of 250-600 granules in every sample results in a pie diagram that illustrates the interparticle heterogeneity within this sample and the abundance of every subunit (Table S1, column D)

5) Since the 4-VAn yield is normalized to nmol Ag, the mole percentage of every subunit is calculated based on columns B & D (Table S1, column E)

6) The mole percentage of each subunit is multiplied with the corresponding normalized yield, adding up these products gives us the estimated theoretical yield for every catalyst batch:
Commercial 6.0 wt% Ag/SiO_2: (0.55*0.018) + (0.20*0.056) + (0.08*0.16) + (0.11*0.061) + (0.05*0.02) + 0.015*0.007) = 0.042 µmol*(nmol Ag)$^{-1}$

Table S1: Calculation of Estimated Theoretical Normalized Yield for the commercial 6 wt% Ag/SiO_2 catalyst.

A	B[1]	C[2]	D	E
Red Colour Index	**Wt% Ag**	**$Yield_{4\text{-}VAn}$ [µmol*(nmol Ag)$^{-1}$]**	**Pie Diagram**	**Mol% Ag**
0.00 – 0.05	3.5	0.018	70	55
0.05 – 0.12	5	0.056	17	20
0.12 – 0.20	6	0.160	6	8
0.20 – 0.40	9	0.061	5	11
0.40 – 0.70	12	0.020	2	5
0.70 – 1.00	15	0.007	0	1.5

[1]Based on red colour index, SEM-EDX and ICP-AES [2]Based on single particle experiments, 4-VAn = 4-vinylaniline.

The yellow, orange and red colours originate both from the amount of 6nm Ag NPs as well as from the large NPs at the outer surface. Hence, a yellow catalyst granule taken from an on average 13 wt% Ag containing powder has a higher silver loading than a similar coloured particle in the 6 wt% commercial sample. To calculate the 4-VAn yield normalized to the silver content per granule in the different samples, we thus included this and adjusted column B of Table S1 for every sample relative to its bulk Ag loading (as determined via ICP-AES).

Bulk catalytic performance testing of powdered catalyst.

Table S2: Bulk hydrogenation of 4-nitrostyrene with different catalyst samples (2 h, 110 °C, 20 bar H_2, 0.35 mole% Ag, 70 mM 4-nitrostyrene in DMA, 500 rpm).

Sample	Wt.% Ag[1]	X (%)	$S_{4\text{-}VAn}$ (%)	$Yield_{4\text{-}VAn}$ [µmol*(nmol Ag)$^{-1}$]	Est. Yield[3]
1	3.58 ± 0.07	15	93	0.040 ± 0.003	0.022
2	9.53 ± 0.37	29	93	0.077 ± 0.044	0.039
3	13.36 ± 0.04	39	85	0.094 ± 0.001	0.064
4	18.97 ± 0.15	25	91	0.066 ± 0.017	0.053
5[2]	6.00 ± 0.40	25	93	0.068	0.042

[1]Determined via ICP-AES [2]Commercial sample [3]Estimated Theoretical Yield based on optical screening. 4-VAn = 4-vinylaniline

Sorting

Calcined commercial silver nitrate on silica gel was manually sorted using an eyelash micromanipulator in three different fractions (Figure S8B-D) on a stereomicroscope (Leica M165FC). A Mettler Toledo AT20 balance was used to determine the weight of the catalyst transferred into the reaction vial (unsorted sample, reaction carried out in duplicate). The reaction vials were placed in a 100 mL Parr reactor and bulk catalytic experiments were performed in parallel (Table S3).

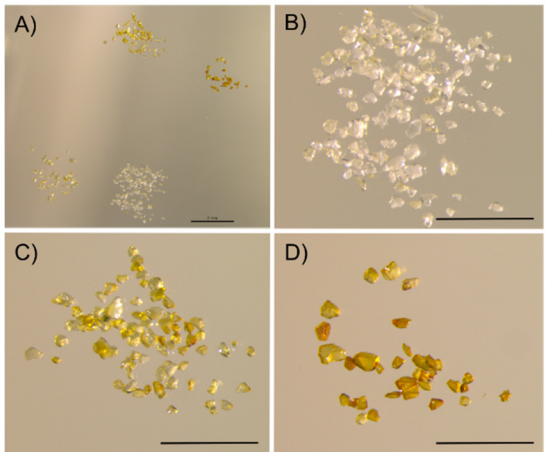

Figure S8. Sorting of commercial $AgNO_3$ sample into 3 fractions. A) Scale bar 2mm, **B-D)** Scale bar 1mm. Images were obtained via a Leica M165FC stereomicroscope equipped with a Leica DFC 450C camera.

Table S3: Bulk hydrogenation of 4-nitrostyrene with unsorted and sorted catalyst (2 h, 110°C, 20 bar H_2, 0.35 mol% Ag, 70 mM 4-nitrostyrene in DMA, hexadecane as IS for GC).

Catalyst	Wt. %[1]	M (mg)	X (%)	$S_{4\text{-VAn}}$[2] (%)	S_{ENB}[3] (%)	Normalized $Y_{4\text{-VAn}}$ [µmol*(nmol Ag)$^{-1}$]
Unsorted	6.00 ± 0.40	0,085 ± 0.004	22	95	3	0.06
B	3.52 ± 0.50	0,119 ± 0.002	10	94	4	0.04
C	5.33 ± 0.70	0,087 ± 0.004	36	95	2	0.20
D	8.71 ± 1.00	0,033 ± 0.002	19	93	3	0.13

[1]Determined via ICP-AES; [2]4-VAn = 4-vinylaniline; [3]ENB=ethylnitrobenzene.

Pt/SiO_2

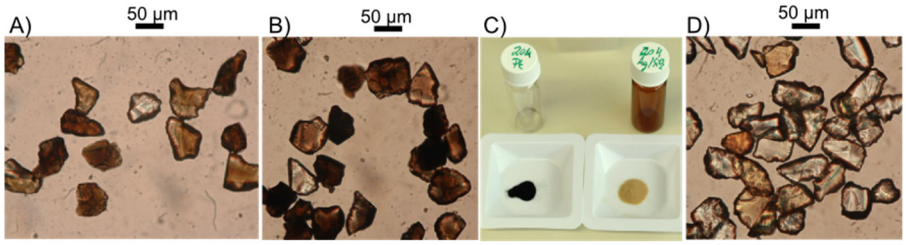

Figure S9. Pt/SiO_2 synthesis similar to Ag/SiO_2, optical microscopy reveals colour heterogeneity not visible on macroscopic scale. Images were obtained via the eyepieces using an adapter from Micro-Tech-Lab (Austria) to connect a Canon EOS5D colour camera to a Olympus BX51 Upright microscope with a standard mercury lamp, equipped with infinity corrected air objectives 4x (0.16 numerical aperture (N.A.)) and 20x (0.40 N.A.).

Synthesis conditions:
(a) aqueous $Pt(NH_3)_4(NO_3)_2$ (31µmol) solution equals pore volume of 120 mg dried silica gel, drop wise added under stirring, 2 h equilibrated at 60 °C, overnight dried in oven at 120 °C, calcined under O_2 flow (0.5 °C/min 350 °C, 2 h).
(b)&(d) aqueous $Pt(NH_3)_4(NO_3)_2$ (49 µmol) and $AgNO_3$ (50 µmol) solution equals pore volume of 70 mg dried silica gel, drop wise added under stirring, ½ h equilibrated at R.T., overnight dried in oven at 120 °C, calcined under static air (1 °C/min 500 °C, 2 h).

SUPPORTING INFORMATION TO CHAPTER 3

Synthesis

Ag/SiO_2 was synthesized via standard incipient wetness impregnation . To 950 mg of dried silica gel (Aldrich 60752) an aqueous solution of $AgNO_3$ (78 mg $AgNO_3$, 750 µL dist. water) was added under vigorous stirring. After equilibration at RT (0.5 h), the silver impregnated silica was dried in static air at 100 °C (16 h) and calcined in static air (1-5 °C/min 500 °C, 2 h).

Modifications to the synthesis procedure:
- NaOH pre-treatment: 0.1 M NaOH aqueous solution (5 mL/g silica), 2 h stirred, supernatant removed via centrifugation (1000 rpm), washed with dist. H_2O (7 times, 1000 rpm), dried (80 °C) and calcined
- wet impregnation: 1.5 mL dist. H_2O added to silica gel before impregnation, eq. 1 h at RT
- vacuum drying: RT, 16 h, 10 mbar
- freeze drying: frozen at -20 °C (4 h) and liquid N_2 cooled (1 h); freeze drying 4 h 0.3 mbar
- fluidized bed drying: 200 mg impregnated powder is transferred to a tubular quartz reactor (Ø 1 cm), 2 quartz wool plugs were used to create a homogeneous flow through the bed and to prevent the powder being blown out, a controlled flow of 30 mL/min 80 % N_2 20 % O_2 was used, oven was heated to 100 °C (10 °C/min) for 8 h
- fluidized bed calcination: 200 mg dry powder, tubular quartz reactor, 30 mL/min 80% N_2 20% O_2, 1 °C/min 500 °C, 2 h

Table S1. Physical properties of the used silica supports.

Silica	Pore diameter (nm)	Pore volume (cm^3/g)	Surface Area (m^2/g)	Purity[2]
Silica gel	6[1]	0.79[1]	409[1]	0.1 wt% Ca
Aldrich 60752				
Self-synthesized	4[1]	0.73[1]	580[1]	
TEOS, HCl				
CARiACT Q-10	10[2]	1.00[2]	300[2]	99.7 wt% SiO_2
Fuji Silysia				0.02 wt% Na_2O

[1] determined via N_2-physisorption [2] Provided by supplier

Optical Microscopy

Images were obtained via the eyepieces using an adapter from Micro-Tech-Lab (Austria) to connect a Canon EOS5D colour camera to an Olympus BX51 Upright microscope with a standard mercury lamp, equipped with infinity corrected air objectives 4x (0.16 N.A.) and 20x (0.40 N.A.). Overview images of the powder bed were obtained with a Leica (M165FC) stereomicroscope.

Colour Index Determination

Colour indexing is described in detail in ref. 64. Images were adjusted to obtain optimal contrast and brightness. The mean 8-bit value in the blue channel was used to increase the sensitivity towards transparent, light yellow and yellow coloured granules.

Nitrogen Physisorption

Nitrogen adsorption and desorption isotherms were measured using a Micromeritics 3Flex 3500 physisorption instrument at 77 K. The sample was degassed before measurement at 423 K for 6 h under vacuum (10^{-2} mbar). The pore size distribution was calculated using the BJH method (Harkins and Jura thickness curve and Faas correction, 3Flex 3.00 software).

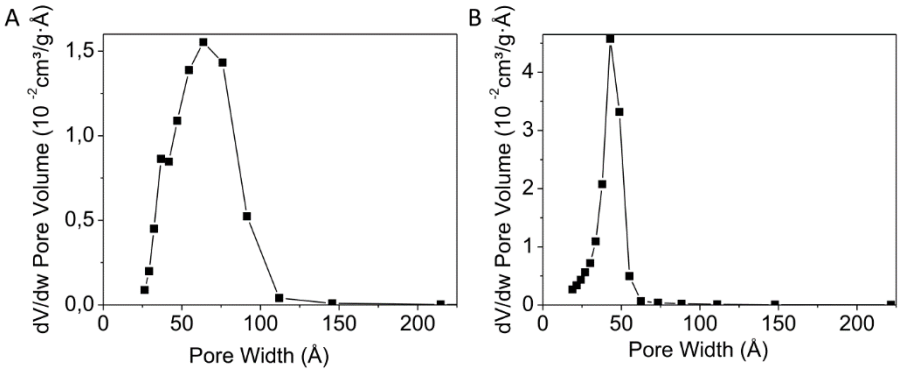

Figure S1. N_2-physisorption cumulative desorption volume for silica **A)** obtained from Aldrich, and **B)** self-synthesized.

Supporting Notes:

1. Heterogeneity at the support granule level before impregnation: Rhodamine 6G

Heterogeneous distribution of surface charges on individual granules was probed both via ion exchanging a cationic dye Rhodamine 6G (R6G). In a neutral solution the negative surface charge density of silica is approximately -0.02 C/m².[65] Based on this value, silica gel powder was contacted with 3 solutions of different concentrations R6G: $[R6G^+ Cl^-]/[O^-]$ [M]/[M] is respectively 1; 0.5 and 0.05 (Figure S2A). After equilibration at room temperature overnight (16 h), the supernatant of solution 1 still contained 38 % of the initial [R6G] (Figure S2B), which indicates the surface charge density of our material is lower than reported in literature and the deposition of dye during drying on the outer surface of the silica gel hinders the probing of surface charges. The most diluted solution on the other hand, is depleted before all surface charges are complexed (Figure S2A-B), so no conclusion regarding a heterogeneous surface charge density can be drawn. The supernatant of the intermediate solution however, only contains 5 µM R6G dye or less than 1 % of the initial concentration (Figure S2A-B).

With standard transmission microscopy, absorbance of Rhodamine 6G in all silica granules is too high to see possible heterogeneous concentration distributions. Also when these dyes are excited with 488 nm laser light (Figure S2B-C, dark blue line), absorption is too high and thus transmission very low. When 405 nm laser light is used on the contrary, there is very little absorption (Figure S2B-C, light blue line) and transmission is high enough to see possible different Rhodamine concentrations and thus surface charge densities. Since transmission and absorbance are also determined by the thickness of the individual granules, this thickness is determined by a z-scan of the fluorescent signal upon 488 nm excitation (Figure S2D). From the transmission image at 405 nm laser light excitation, absorbance can be determined since $A = {}^{10}\log(I/I_0)$. Intensities for the granule area and background surrounding the granule are normalized between 0 and 1 based on the minimum and maximum intensity of the whole image. The obtained absorbance is divided by the extinction coefficient of R6G at 405 nm and the thickness obtained from the z-scan, resulting in a concentration value (Figure S2E). Based on the resulting concentration differences among the silica granules, it can be concluded that there is a 5-fold interparticle heterogeneity in surface charge density.

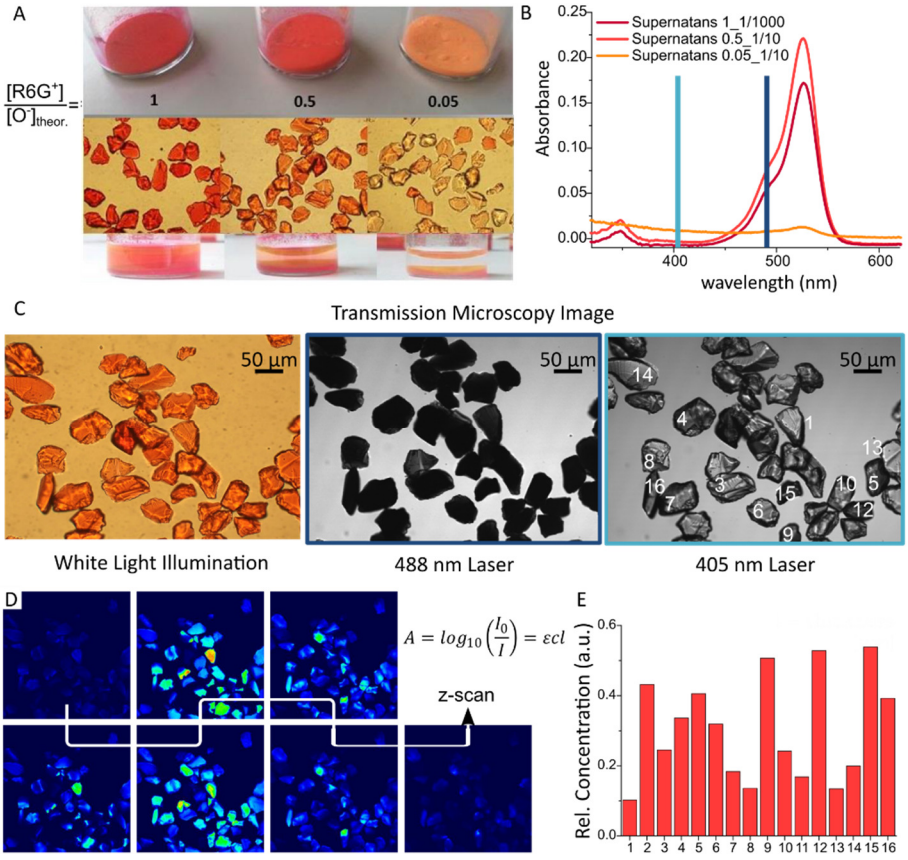

Figure S2. Probing of surface charge density heterogeneity with Rhodamine 6G dye. **A)** silica gel powder contacted with 3 solutions of different R6G concentration; **B)** UV-Vis absorbance of R6G in supernatant solutions (pink and orange lines) after equilibration at room temperature overnight (16 h), blue lines indicate excitation wavelength for fluorescence microscopy study in C; **C)** fluorescence microscopy: R6G excitation with 488 nm laser light (dark blue line,) and 405 nm laser light (light blue line) (FluoView FV-1000 instrument, Olympus Japan; emission mirror 550-635 nm); **D)** individual granule thickness determination by a z-scan of the fluorescent signal upon 488 nm excitation; **E)** relative single particle R6G concentrations based on thickness, absorbance and extinction coefficient of R6G at 405 nm.

2. Heterogeneity induced during impregnation

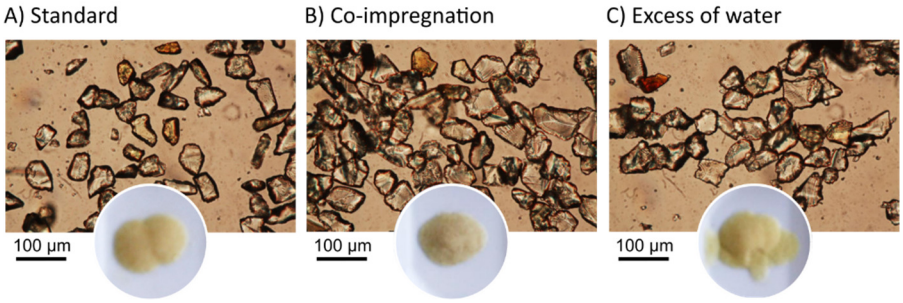

Figure S3. A) silver nanoparticles supported on silica, synthesized via standard incipient wetness impregnation (950 mg silica, 78 mg $AgNO_3$, 750 µL dist. water; drying in vacuum oven at RT 16h, calcination static air, 500 °C 2 h). Impregnation varied: **B)** co-impregnation with NH_4NO_3 (10 eq.) **C)** impregnation solution: 4 mL H_2O.

3. Heterogeneity induced during calcination

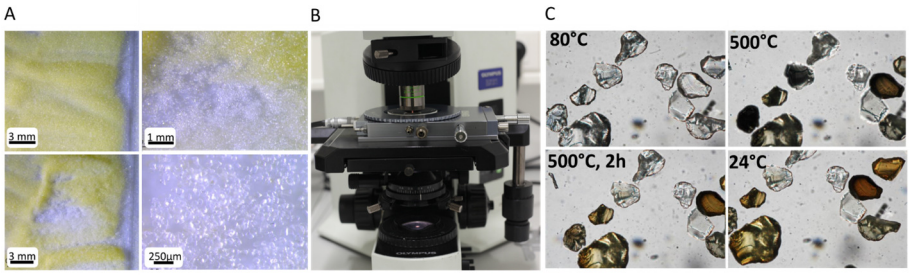

Figure S4. A) Heterogeneities as a consequence of position in the calcination bed are noticed. **B-C)** In situ observation of calcination via a Linkam THMS600 heating stage and an Olympus BX51 upright microscope.

References

(1) Plessers, E.; Stassen, I.; Sree, S. P.; Janssen, K. P. F.; Yuan, H.; Martens, J.; Hofkens, J.; De Vos, D.; Roeffaers, M. B. J. *ACS Catal.* **2015**, *5*, 6690–6695.

(2) Kosmulski, M. *Chemical Porperties of Material Surfaces*; Marcel Dekker, Inc: New York Basel, 2001.

SUPPORTING INFORMATION TO CHAPTER 4

1. Synthesis and Characterization

All chemicals and solvents used in the syntheses were of reagent grade and used without further purification.

MOF Synthesis

All materials were made in a closed Schott DURAN® pressure plus bottle with a volume of 1 L under static conditions. UiO-66 and UiO-66-NO_2 were synthesized in the presence of a modulator, starting from an equimolar solution of $ZrCl_4$ (3.5 g, 15 mmol) and terephthalic acid (2.5 g, 15 mmol) or 2-nitroterephthalic acid (3.2 g, 15 mmol), dissolved in DMF (155 mL, 2 mol), 1.5 mL of a 36 wt% solution of HCl (17 mmol) and 20 equivalents (23 mL of CF_3COOH) were also added to the mixture. UiO-66-NH_2 was synthesized without the presence of a modulator, also starting from an equimolar mixture of $ZrCl_4$ (0.48 g, 2.1 mmol) and 2-amoniterephthalic acid (0.372 g, 2.1 mmol) dissolved in DMF (120 mL), 0.15 mL H_2O was added.

All synthesis mixtures were placed in a preheated oven at 120 °C for 21 h (modulated) or 24 h (non-modulated). The powders were collected via centrifugation (10 minutes, 11 000 rpm) and thoroughly washed with DMF (3 times) and methanol (3 times).

Supported Ag nanoparticle synthesis

Before Ag infiltration, the MOFs are activated at 150°C for 16 hours. $AgNO_3$ (512 mg $AgNO_3$, 3 mmol) is dissolved in 6 mL of a H_2O:EtOH 1:5 solution, a pure ethanol solution is not possible as a consequence of the low solubility of $AgNO_3$ in ethanol. This aqueous-ethanolic $AgNO_3$ solution is added to a vial containing 200 mg MOF, the vial is sealed with a crimp cap and flushed with nitrogen to remove all O_2. Interaction of Ag^+ ions with light is prevented by a protective layer of aluminium foil around the vial. The MOF-$AgNO_3$ mixture is sonicated for 2 minutes and stirred continuously for 16 hours at 500 rpm. The sample is thoroughly washed (+/- 5 times) with ethanol to remove remaining $AgNO_3$ and unbound Ag particles formed in solution, centrifugation (8 minutes, 3000 rpm); removal of the supernatant and addition of fresh EtOH are performed under an inert atmosphere. A NaCl-solution can be added to the supernatant solution to check whether there is still some $AgNO_3$ present. After washing the sample is dried in a vacuum oven at room temperature for 16 hours.

Powder X-ray Diffraction

Powder X-ray diffractograms were routinely collected on a STOE STADI COMBI P diffractometer in High-Throughput mode, equipped with an image plate detector using Cu Kα radiation (λ = 1.54056 Å). Diffractograms of the materials are shown in Figure S1.

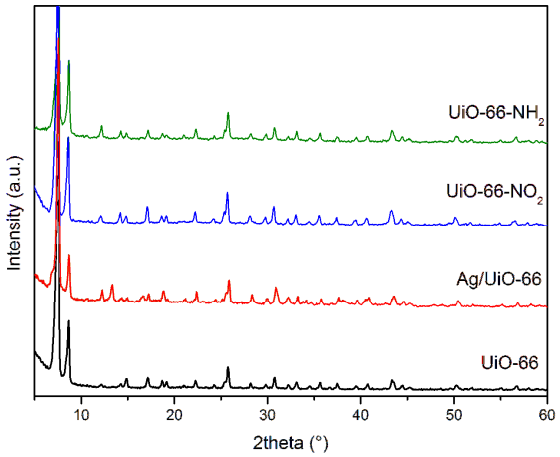

Figure S1. Powder X-ray diffractograms of UiO-66-X and 13 wt% Ag-loaded UiO-66.

Scanning Electron Microscopy

Scanning Electron Microscopy (SEM) images were obtained using a JEOL SEM (JSM-6010LV).

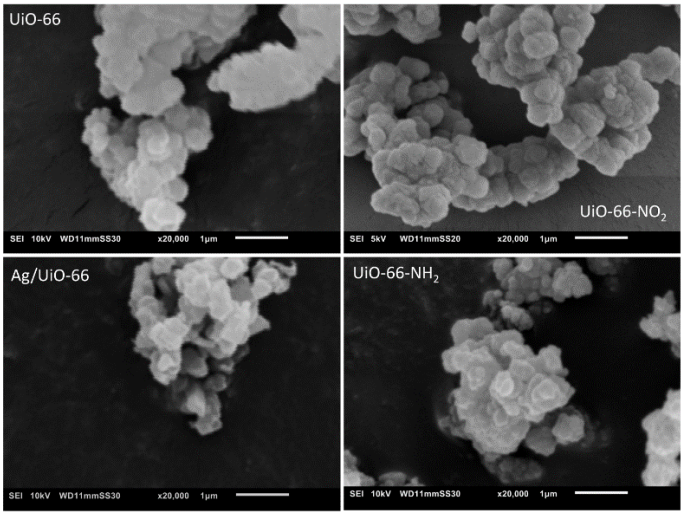

Figure S2. SEM images of UiO-66-x and Ag/UiO-66 (scale bar = 1 µm).

Nitrogen Physisorption

Nitrogen adsorption and desorption isotherms at 77 K were measured using a Micromeritics 3Flex 3500 physisorption instrument. The sample was degassed before measurement at 423 K for 6 h under vacuum (10^{-2} mbar). The pore size distribution was calculated using the BJH method (Harkins and Jura thickness curve and Faas correction, 3Flex 3.00 software).

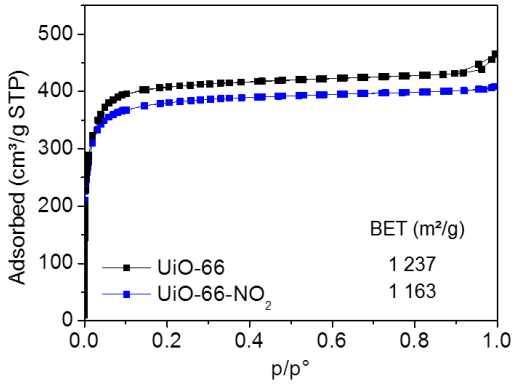

Figure S3. Nitrogen adsorption and desorption isotherms and BET surface area.

Fourier Transform Infrared Spectroscopy (FTIR)

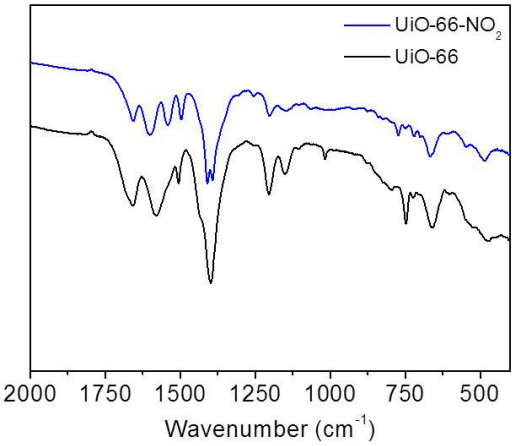

Figure S4. FTIR spectra of modulated UiO-66 and UiO-66-NO_2 metal-organic frameworks.

2. Catalytic Experiments

High H_2 Pressure Hydrogenation

For the high pressure hydrogenation reaction, 25 mg of catalyst (UiO-66, Ag-loaded and pure, crystal size 0.4 µm aggregated into 1-10 µm sized clusters, pore diameter 1.1 nm and 0.8 nm), 1.15 mmol (145 µL) of cinnamaldehyde, 0.95 mmol tetradecane (245 µL, internal standard) and 3.3 mL of *N,N*-dimethylacetamide (DMA, solvent) were introduced into a 15 mL autoclave. After flushing with N_2, the autoclave was pressurized with H_2 to 20-50 bar of H_2 and stirred with a magnetic stirring bar at 500 rpm. The hydrogenation reaction was performed at 140 ℃ for 6 h, unless stated otherwise. For analysis of the liquid products, the catalyst was removed by centrifugation and analysis of the reaction products was carried out using a gas chromatograph (Shimadzu 2010 GC) equipped with a CP-Sil 8 column and FID detector. Tetradecane was added as internal standard for quantitative GC analysis. Identification of the compounds was carried out using GC-MS.

MPV reduction

Before reaction, each catalyst was dried at 200 °C to remove residual solvent molecules; catalytic reactions were carried out in 10 ml glass crimp cap vials loaded with 20-30 mg catalyst (Zr/substrate ratio was kept constant by varying the amount of catalyst; UiO-66-x: crystal size ± 0.4 µm aggregated into 1-10 µm sized clusters, BET surface area 1237 m²/g UiO-66 and 1163 m²/g UiO-66-NO2) and a magnetic stirring bar. A solution of the substrate (1.15 mmol) in 3.3 mL isopropyl alcohol (IPA) was added; tetradecane was added as internal standard. For each catalyst, a substrate to Zr ratio of 7.8 was used as to compare the activity of each catalyst. After introduction of the reaction mixture, the vials were placed in an aluminium heating block (at 120 °C) and stirred. Reaction samples were filtered through a 0.2 µm PTFE filter (Thermo scientific), and analysed with gas chromatography (Shimadzu 2010 GC, CP-Sil 8, FID detector). Reaction products were identified using GC–MS (Agilent, HP-1, MS). Reactions were performed in duplicate, and the results shown are averaged.

3. Recycle test

For the recycling test, the used catalyst was isolated from the reaction mixture by centrifugation (3000 rpm, 10 minutes) and thoroughly washed with DMA or isopropyl alcohol until the supernatant was purely solvent, as confirmed by GC. The recovered catalyst was reactivated overnight at room temperature in a vacuum oven (10 mbar, Ag-loaded UiO-66) or at 150 °C (UiO-66) and reused under the same reaction conditions.

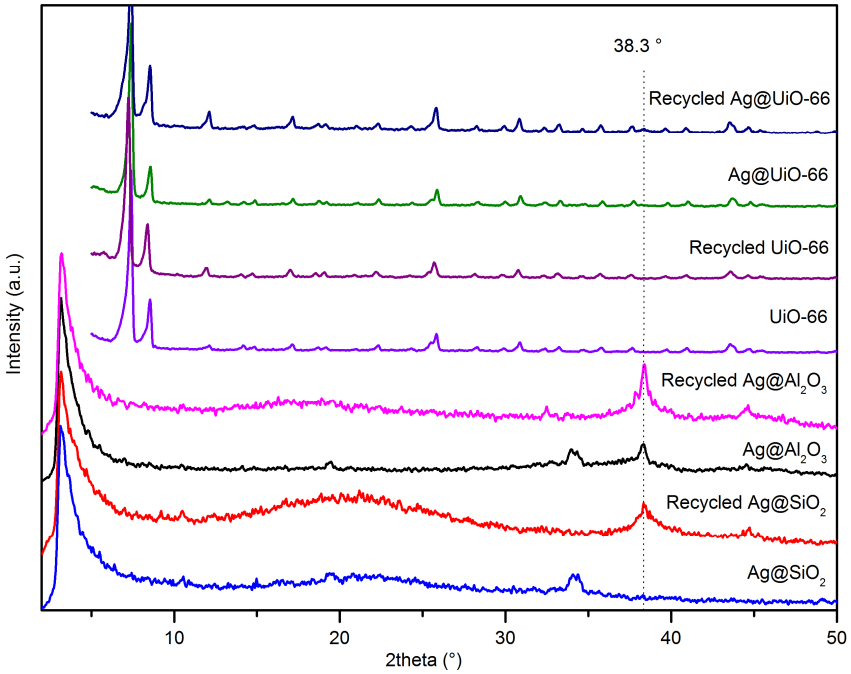

Figure S5. Powder X-ray diffractograms of UiO-66 and Ag-loaded - UiO-66, - SiO_2 and - Al_2O_3 before and after catalytic reaction. Although the activity of UiO-66 decreases upon recycling, crystallinity is retained after 3 recycle steps, however the very small blunt diffraction at 6° might be associated with a primitive cubic defect.[56]

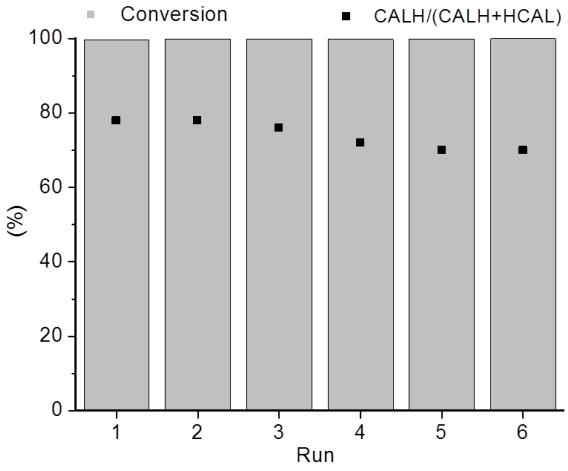

Figure S6. Conversion of cinnamaldehyde and selectivity to cinnamyl alchol (CALH) compared to hydrocinnamaldehyde (HCAL) after 5 times recycling of the Ag/UiO-66 catalyst (140 °C, 50 bar of H_2, 500 rpm, 6 h).

Thermogravimetric Analysis

UiO-66 and recycled UiO-66 (after 3 recycling steps) was analysed by Thermogravimetric Analysis (TGA) under a stream of N_2-gas using a Universal V4.5A TA Instrument running from room temperature to 800 °C with a scan rate of 3.5 °C/min.

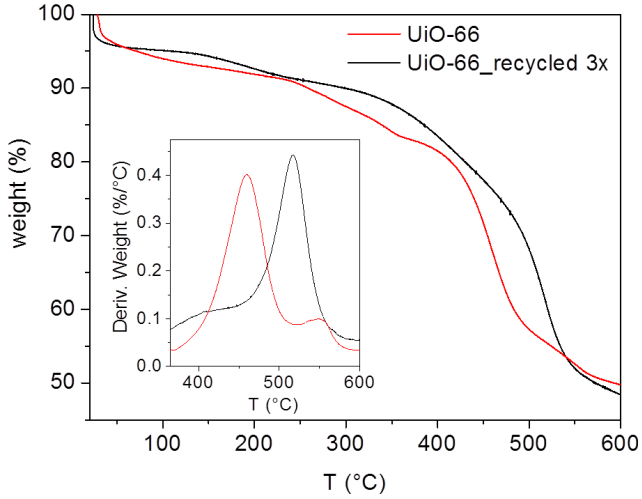

Figure S7. Thermogravimetric Analysis (TGA) of UiO-66 and UiO-66 after 3 recycling steps.

SUPPORTING INFORMATION TO CHAPTER 5

1. Characterization

Powder X-ray Diffraction

Powder X-ray diffractograms were routinely collected on a STOE STADI COMBI P diffractometer in High-Throughput mode, equipped with an image plate detector using CuKα radiation (λ = 1.54056 Å). Diffractograms of the materials are shown in Figure S1.

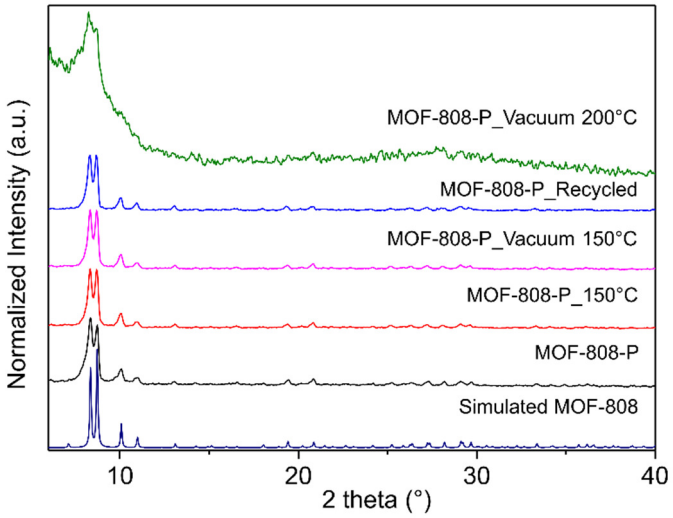

Figure S1. Powder X-ray diffractograms of MOF-808-P: simulated MOF-808 pattern, as synthesized MOF-808-P, activated at 150 °C and 200 °C for 16 h and recycled after reaction.

Scanning Electron Microscopy

Scanning Electron Microscopy (SEM) images were obtained using a JEOL SEM (JSM-6010LV).

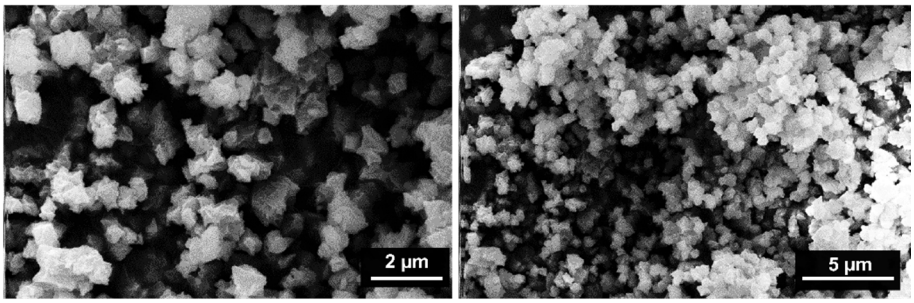

Figure S2. SEM micrograph of MOF-808-P.

Thermogravimetric Analysis

MOF-808-P was analysed by Thermogravimetric Analysis (TGA) under a stream of N_2-gas using a Universal V4.5A TA Instrument running from room temperature to 650 °C with a scan rate of 5 °C/min.

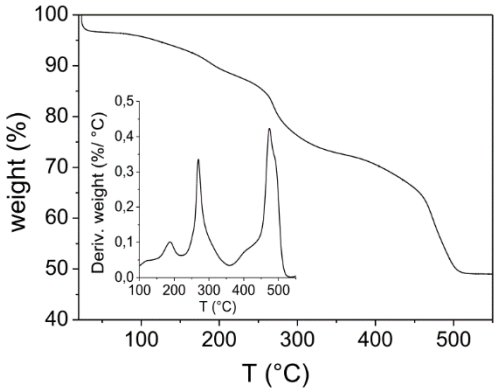

Figure S3. Thermogravimetric Analysis.

CD_3CN Chemisorption

Sorption with deuterated acetonitrile (CD3CN) (Figure S4) indicated a larger ratio of chemisorbed molecules on Lewis acid sites to physisorbed molecules (vibration frequency at respectively 2297 cm^{-1} and 2265 cm^{-1}) for MOF-808-P compared to UiO-66 after activation at 150 °C. A large fraction of the CD_3CN molecules on the Lewis acid sites of MOF-808-P stay chemisorbed upon desorption under vacuum with increasing temperature to 150 °C, indicating a high acid strength.

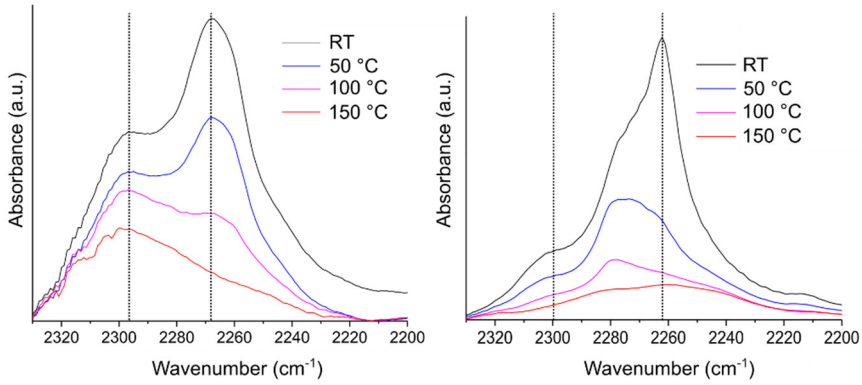

Figure S4. Normalized FTIR spectra of CD_3CN chemisorption on MOF-808-P (left) and UiO-66 (right) at 10 mbar (RT) and desorption under vacuum at increasing temperature.

Elemental Analysis

Inductively Coupled Plasma (ICP) – Atomic Emission Spectra (AES) were recorded on a Varian 720-ES. Sample breakdown was performed in 0.5 ml aqua regia (1:3 HNO_3:HCl) and 3 mL HF (40%) for 1 h at 100 °C. The HF-solution was neutralized with excess H_3BO_3 99.99% and the spectral signal was compared to Zirconium Standard (TraceCERT, 1000 mg/L Zr in HNO_3: HF Sigma-Aldrich Cat. N° 73574).

Table S1 Theoretical molecular formula and Zr-percentage compared to ICP-AES analysis of self-synthesized MOF-808-P activated at 150 °C (16 h).

Entry	Material	Molecular Formula	Wt% Zr
1	MOF-808 [31]	$[Zr_6O_4(OH)_4](HCOO)_6[C_6H_3(COO)_3]_2$	40.15
2	MOF-808-P.2H_2O [32]	$[Zr_6O_5(OH)_3](HCOO)_5[C_6H_3(COO)_3]_2(H_2O)_2$	40.43
3	MOF-808-P.2DMF [32]	$[Zr_6O_5(OH)_3](HCOO)_5[C_6H_3(COO)_3]_2(DMF)_2$	37.76
4	MOF-808-P_150C		39.40±0.7

2. Catalytic Experiments

Recycle test

For the recycling test, the catalyst was collected via centrifugation (3000 rpm, 10 minutes) after reaction and thoroughly washed with EtOH and IPA for 4 times (3000 rpm, 15 minutes). The recovered catalyst was reactivated first at 60 °C and overnight at 150 °C. Reaction solution was adjusted to account for the catalyst loss (10-20 %). In the first recycle run cinnamyl alcohol and carvone yield decrease with 25 %.

Reflux

For the reaction under reflux, 20 mg of activated MOF-808-P, 3.3 mL IPA, 145 µL tetradecane and 180 µL *R*-carvone were placed in a 50 mL two-mounted flask connected to a condenser. The reaction mixture was refluxed at 80 °C and stirred at 250 rpm, while a N_2-flow was passed over the mixture to remove the formed acetone.

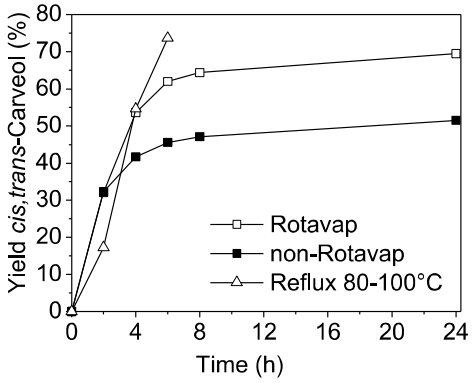

Figure S5. Evaporation of acetone and isopropyl alcohol and addition of fresh IPA solvent (□) indicate that the equilibrium of the MPV reduction of *R*-carvone with MOF-808-P can be shifted towards *cis,trans*-carveol. By performing the reaction under reflux at 80 to 100 °C yield could be increased to 74 %.

1-Indanol as reducing agent

MPV reduction reactions were carried out with 5 or 12 equivalents of IPA and 1-indanol in toluene.

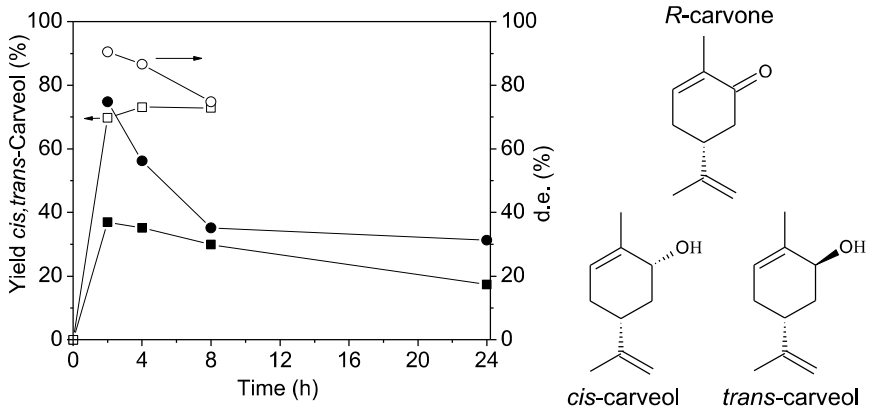

Figure S6. MPV reduction of *R*-carvone with MOF-808-P with 5 (filled) or 12 (open) equivalents of (S)-1-Indanol. When yield of *cis,trans*-carveol (■,□) reaches equilibrium (73 %), epimerization occurs and the diastereomeric excess (d.e., ●,○) decreases.

LIST OF PUBLICATIONS

Plessers, E., Stassen, I., Pulinthanathu Sree, S., Janssen, K., Yuan, H., Martens, J., Hofkens, J., De Vos, D., Roeffaers, M. (**2015**). Resolving Interparticle Heterogeneities in Composition and Hydrogenation Performance between Individual Supported Silver on Silica Catalysts. ***ACS Catalysis**, 5* (11), 6690-6695.

Plessers, E., De Vos, D., Roeffaers, M. (**2016**). Chemoselective reduction of alpha,beta-unsaturated carbonyl compounds with UiO-66 materials. ***Journal of Catalysis**, 340*, 136-143.

Plessers, E., Fu, G., Tan Yong Xiang, C., De Vos, D., Roeffaers, M. (**2016**). Zr-Based MOF-808 as Meerwein–Ponndorf–Verley Reduction Catalyst for Challenging Carbonyl Compounds. ***Catalysts**, 6*, 104-104.

E. Plessers, J. E. van den Reijen, P. E. de Jongh, K. P. de Jong, M. B. J. Roeffaers. Optical Microscopy Reveals the Origin of Heterogeneity at the Support Granule Scale of Silver on Silica Catalysts. *Submitted.*

NOTES